ABSTRACT

MADER, GREGORY CHARLES. Modeling Cerebral Autoregulation During Orthostatic Stress in the Presence of Aging and Hypertension. (Under the direction of Mette Olufsen.)

Cerebral autoregulation refers to the brain's control mechanisms responsible for maintaining cerebral blood flow at an appropriate, approximately constant, level despite changes in arterial blood pressure. Metabolic, myogenic, shear-dependent, and neurogenic influences work collectively to ensure adequate flow and necessary distribution of nutrients to cerebral tissue. Cerebral autoregulation is typically studied from two perspectives. First, static autoregulation defines the steady-state relationship between blood pressure and blood flow, typically illustrated by the autoregulatory plateau curve. The second perspective is dynamic cerebral autoregulation, which describes the transient response of blood flow velocity to changes in arterial pressure. This study combines the two modeling methodologies deriving a simple pulsatile nonlinear model that uses measured pressure values as an input to quantitatively predict cerebral blood flow dynamics during postural change. The model is motivated by the analysis of time-varying dynamics observed in the filtered and pulsatile measurements of flow and pressure, indicating a nonlinear response. The present study addresses data analysis, model development, and shows how structural and practical parameter identifiability methods can be used to demonstrate that the model displays correct qualitative and quantitative behavior. Finally parameter estimation is used to show that the model can accurately predict middle cerebral blood flow velocity measurements recorded during postural change. Current methods do not detect a difference in the performance of cerebral autoregulation due to aging or hypertension, despite the many cerebrovascular changes that occur in each of those states. In this study, we show that by accounting for pulsatility and nonlinearity, it is possible to devise a measure that can distinguish between

three patient groups: healthy young, healthy elderly, and hypertensive elderly. Results are obtained by analyzing model dynamics and estimating patient specific model parameters for each subject. In addition, nonlinear mixed effects analysis was used to test if all subjects belong to the same population with equal population parameter values, or if the population parameters vary among the three subgroups. Future work could entail using a detailed theoretical autoregulation model as a tool for generating various static curves within the model framework, eventually arriving at a clinically useful physiologically-based index for cerebral autoregulation.

Modeling Cerebral Autoregulation During Orthostatic Stress
in the Presence of Aging and Hypertension

by
Gregory Charles Mader

A dissertation submitted to the Graduate Faculty of
North Carolina State University
in partial fulfillment of the
requirements for the Degree of
Doctor of Philosophy

Biomathematics

Raleigh, North Carolina

2016

APPROVED BY:

_____   _____
Adam Mahdi   Hien Tran

_____   _____
Pierre Gremaud   Mette Olufsen
                                                        Chair of Advisory Committee

DEDICATION

To my parents, for all of your sacrifices, love, and support. I couldn't imagine having two better role models. To my sister, for daring to be different and for putting up with her older brother. You continue to amaze me, and I am so proud of you. To the rest of my family, for being my biggest fans. To my soon-to-be wife Emily, for all the adventures we have taken and for all that you have done to inspire me to be the best I can be. I wouldn't want to go through life with anyone else. To all of my friends, for never understanding the life of a mathlete yet still filling my life with joy and laughter. To all of my teachers and advisors at Immaculata Catholic School, Cardinal Gibbons High School, Elon University, and North Carolina State University, especially Dr. John Sprague, Mrs. Joan Troy, Dr. Karen Yokley, Dr. Todd Lee, Dr. Jeff Clark, Dr. Adam Mahdi, and Dr. Mette Olufsen. To all of the coaches that have made the commitment to make me a better leader and teammate, especially Tim Healy, Darren Powell, and Leo Fitzsimmons. Lastly, to my dog Ellie, for her continued love and distraction.

BIOGRAPHY

Greg Mader was born in Durham, North Carolina on May 18, 1989. He went to Immaculata Catholic School for prekindergarten through eighth grade, where he received the Regal Eagle Award. His kindergarten diploma is still framed and on display at home. Greg then attended Cardinal Gibbons High School, where he first recognized his aptitude and appreciation for mathematics. He served as a captain of the school's men's soccer team en route to their state championship. For undergraduate studies, he attended Elon University and was a four-year letterman in soccer. He obtained a Bachelor of Science in Mathematics and was inducted into Phi Beta Kappa, Phi Kappa Phi, Pi Mu Epsilon honor societies. He received the AL Hook Scholar-Athlete Award, indicating the highest male athlete grade point average. He served on the Student-Athlete Advisory Council, which acts as a liaison between athletics, academics, and administration. After matriculating in 2011, he was awarded the distinct honor of serving as a youth trustee on the Elon University Board of Trustees. He chose to attend North Carolina State University for graduate studies in applied mathematics, eventually pursuing a doctorate in the biomathematics program.

ACKNOWLEDGEMENTS

TABLE OF CONTENTS

LIST OF TABLES

LIST OF FIGURES

CHAPTER

1

CEREBRAL AUTOREGULATION

1.1 Cerebral Circulation

Even though the human brain constitutes about two percent of total body weight, the brain receives 15 percent of the resting cardiac output [Hal16]. Blood flow to the brain is imperative for bodily function, and as a result, it is a highly vascularized organ. If the flow of blood to the brain is completely stopped, unconsciousness will occur within five to ten seconds. The blood flow of the human brain is supplied by four major arteries: two

internal carotid arteries and two vertebral arteries. Each carotid artery contributes roughly 40% to the total cerebral perfusion. The two vertebral arteries merge to form the basilar artery, which contributes approximately 20% to the total cerebral perfusion and intersects with the two internal carotid arteries at the base of the brain to form the Circle of Willis (CoW) [Hal11]. A complete CoW allows for the flow of blood to be maintained even if an artery is blocked. However, only half of the human population has a complete CoW [KH98]. Blood is distributed from the CoW via the anterior cerebral arteries, middle cerebral arteries (MCA), and the posterior cerebral arteries. The MCA supplies the cortical regions connected with auditory, motor, somatosensory, and speech activities. Since the MCA is one of the larger cerebral arteries and extends laterally from the Circle of Willis to the temporal bone, it is the most accessible cerebral vessel for transcranial Doppler (TCD) ultrasound.
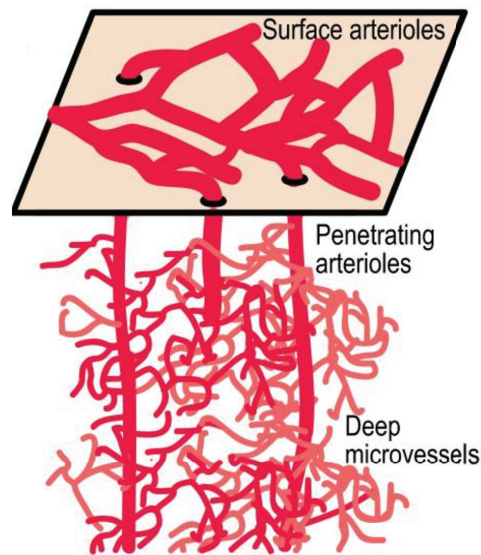
Figure 1.1 Penetrating Arterioles. Branching from the pial arterioles, a majority of cerebral autoregulation occurs in the penetrating arterioles. Adapted and reproduced with permission from [Nis07]. Copyright (2007) National Academy of Sciences.

The arteries extending from the Circle of Willis travel along the surface of the brain and eventually give rise to pial arteries, which branch out into smaller vessels called penetrating arteries and arterioles, shown in Figure 1.1. Pial arteries and arterioles comprise the sections of the cerebrovascular bed directly under the control of regulatory mechanisms. Thus, a vast majority of cerebral blood flow regulation occurs in these arterioles. These penetrating vessels branch into intracerebral arterioles and capillaries, where nutrients and gases are exchanged between the blood and tissues. The velocity of blood flow significantly decreases as arteries branch to arterioles, but the flow is the slowest in the capillaries due to the increased cross-sectional area. Similar to other parts of the body, the highest number of capillaries exist where the metabolic needs are greatest. However, brain capillaries are much less leaky than the capillaries in other areas of the body. The main reason for this feature is that the cerebral capillaries have glial feet along all sides of the vessel. These feet, which are projections from glial cells, provide protection against over-stretching of the walls in the presence of high blood pressure. The regulation of cerebral blood flow is achieved through the interaction between neurovascular coupling (global) and cerebral autoregulation (local). Astrocytes are specialized cells that couple the neuronal activity with the local regulatory mechanisms [Att10].

The structure of arterial blood vessels varies throughout the vascular bed. When compared to the arterioles and capillaries, the arteries are much larger and thicker. Arterioles range from 9 to 40 μm in diameter; where as, capillaries are the smallest vessels with a diameter of approximately 7 μm. Arteries also have the most elastic walls, ensuring that they can withstand the rapid flow of blood [Cam99]. Arterioles have many layers of smooth muscle outside of the endothelium, which allows them to efficiently and rapidly regulate

diameter. Capillaries are responsible for the exchange of nutrients and gases between the blood and the tissue, and thus consist of only a small layer of endothelial cells.

1.2   Cerebral Blood Flow

Fluid flow through a vessel can be quantified by combining Ohm's Law and mathematical principles of pipe flow. The flow of blood through a vessel, denoted Q, is driven by a pressure gradient (Δp) and counteracted with a resistance (R), yielding the equation

$$Q = \frac{\Delta p}{R}.$$

(1.1)

The resistance of flow in a vessel is due to the friction between the particles in the fluid (viscosity μ) and the friction between the blood and the vessel wall. Changes in the radius of a vessel can have an immense effect on how much blood is able to flow through it. Resistance in a vessel can be written as

$$R = \frac{8\mu L}{\pi r^4},$$

(1.2)

where the radius and length of the vessel are given by r and L, respectively. By plugging in the expression for R into the previous equation, the law of Poiseuille flow can be obtained:

$$\Delta p = \frac{8\mu L Q}{\pi r^4}.$$

(1.3)

Cerebral blood flow (CBF) and cerebral blood flow velocity (CBFV) can sometimes be confused as interchangeable, but they are not. For blood traveling through a vessel, the

blood flow velocity is the distance traveled per unit of time, often expressed as cm/sec. Conversely, the blood flow represents a volume moving per unit of time, typically having units of cm^3/min. Flow and velocity (V) within a vessel are related by the equation $Q = VA_c$ where A_c denotes the cross-sectional area of the vessel, given by the equation $A_c = \pi r^2$. In other words, at constant vessel radius (r), changes in flow (CBF) are proportionate to changes in velocity (CBFV). When considering cerebral circulation, oftentimes it is important to use the mean velocity because blood flowing in a vessel has a parabolic profile under laminar flow conditions (Hagen-Poiseuille Flow).

1.3   Cerebral Autoregulation

Cerebral autoregulation is a collection of local mechanisms that aim to maintain constant cerebral blood flow and oxygen supply amidst changes in arterial blood pressure. The maintenance of flow is accomplished by changing cerebrovascular resistance through vasoconstriction or vasodilation of arterioles and small arteries, induced by a change in vascular smooth muscle cell (VSMC) tone. There are four mechanisms that contribute to local regulation within the brain: the myogenic, metabolic, shear-dependent, and neurogenic responses. Each of these mechanisms are triggered by different stimuli that cause diameter changes in cerebral arterial vessels.

1.3.1   Myogenic Response

The cerebral myogenic response, during which decreased intraluminal pressure causes vasodilation, is key to maintaining constant cerebral blood flow (CBF) in response to varia-

tions in systemic pressure and to providing a critical shield to protect brain capillaries and blood-brain barrier. After detecting a change in pressure, mechanosensors in the smooth muscle cells of the arterial wall trigger various physiological responses. Eventual constriction or dilation of vascular smooth muscle is achieved to ensure that flow remains at its baseline value. Figure 1.3 shows a slightly more detailed version of the myogenic response.
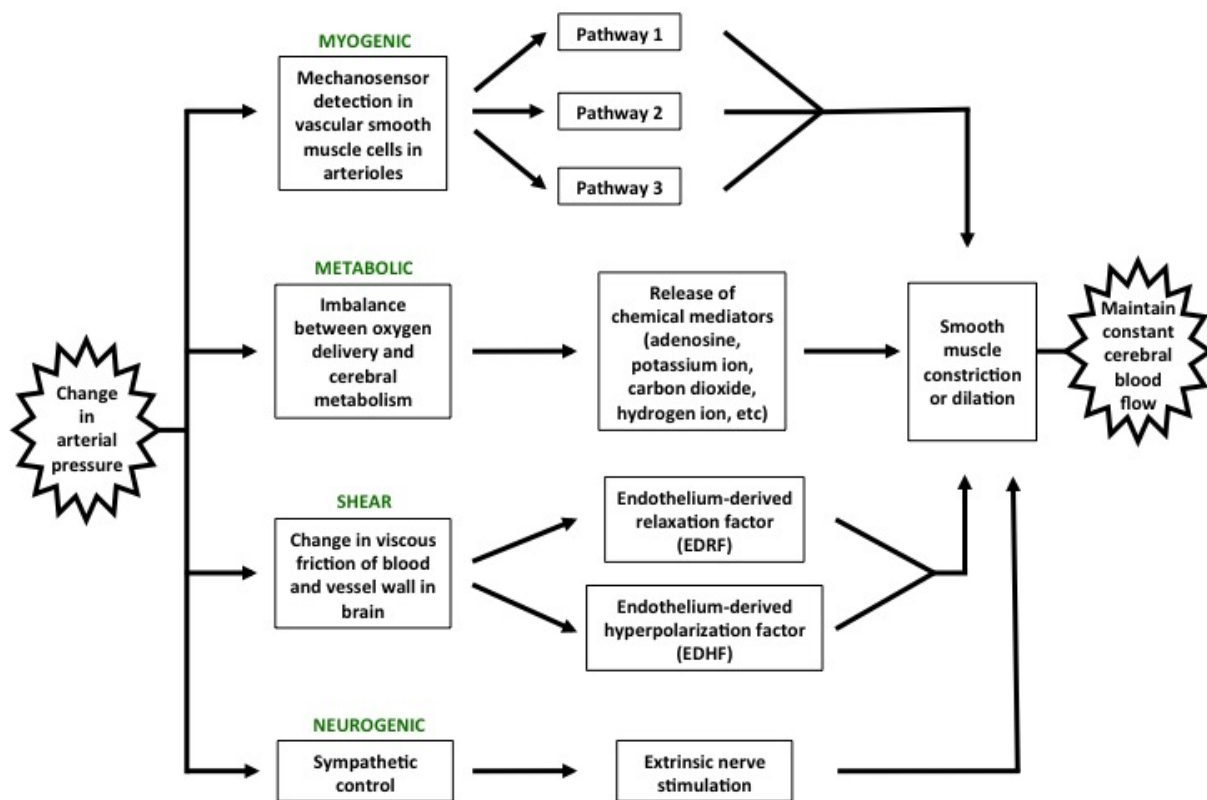
Figure 1.2 Cerebral Autoregulation Response. Following an abrupt change in arterial blood pressure, the myogenic, metabolic, shear-dependent, and neurogenic responses are activated and work collectively to cause a vasoconstriction or vasodilation in the cerebral vessels. This flowchart represents a general summary the local autoregulatory responses within the brain.

Once the change is detected by mechanosensors, there are three possible pathways for the myogenic response to occur, ultimately resulting in vasodilation (assuming a decrease in blood pressure). One signaling pathway is characterized by calcium ion induced contraction via myosin light chain kinase-catalyzed phosphorylation of myosin light chain

Myogenic Response

Myogenic Pathway 1	Myogenic Pathway 2	Myogenic Pathway 3
Membrane potential depolarization	Activation of ROCK and protein kinase C pathways	Activation of Rho-associated protein kinase (ROCK) pathway
Activation of nonselective ion channels	Actin polymerization	Phosphorylation of myosin phosphatase target subunit 1 (MYPT1)
Opening of voltage-gated calcium channels	Enhanced membrane connections	Inhibition of myosin light chain (L_{20}) phosphatase
Calcium ion decreases electrochemical gradient and binds to calmodulin	Force transmission	Phosphorylation of L_{20}
Activation and phosphorylation of myosin light chain kinase	Arterial vasoconstriction	
Cross-bridge cycling		

Figure 1.3 Myogenic Response. Triggered by a change in arteriolar pressure, mechanosensors along the arterial wall initiate three possible pathways for myogenic regulation, ultimately achieving vasoconstriction or vasodilation. This general description of the myogenic response shows what happens during increased pressure, eventually resulting in constriction of cerebral arterioles.

LC_{20} in response to membrane depolarization. A second pathway includes the calcium ion sensitization of contraction elicited by Rho-associated kinase (ROCK)-mediated phosphorylation of myosin phosphotase target subunit 1(MYPT1) and inhibition of myosin light chain phosphotase. The third possible pathway is the calcium ion sensitization of contraction elicited by dynamic regulation of actin cytoskeleton mediated by protein kinase C and ROCK. It is important to note that these pathways describe the induced vasoconstriction due to an increase intraluminal CBP (as opposed to vasodilation) [WC13]. The myogenic response is characterized by a time constant of 2.5-10 seconds [Pet11; Spr12]. Because of the large mass of smooth muscle found within cerebral arteries, it is believed that this response may be more developed in the brain than elsewhere in the body.

1.3.2 Metabolic Response

The metabolic response is comprised of all the chemical transformations that occur within the red blood cells flowing through the lumen of arterioles. The chemical transformations convert and use energy for the regulation of blood flow. The diameters of blood vessels are controlled by balancing the cerebral metabolic demand blood supply to the brain (see Figure 1.2). Numerous studies have discussed the existence and importance of several chemicals that couple blood flow and metabolism, including hydrogen ions, potassium ions, lactate, carbon dioxide, and oxygen. An increase in the concentrations of potassium ions or hydrogen ions causes vasodilation. Lactate concentrations significantly elevate during a reduction in arterial blood pressure, and lactic acid, which is the end product of glycolysis, decreases pH. The effect of pH on blood flow appears to be a global effect linked with chemoreceptors and thus is not considered an important facet of cerebral autoregulation.

However, local changes in pH can modulate the vasomotor responses to other agents that affect vessel caliber, such as norepinephrine. Cerebral arteries dilate in response to increases in the partial pressure of arterial carbon dioxide (Pa_{CO_2}), and carbon dioxide reactivity is a major player in dCA. It is believed that Pa_{CO_2}, pH and adenosine serve as coupling factors, but the mechanisms involved cannot be fully explained [Aoi09; ZM97]. Adenosine has also been proposed as a regulator of CBF and a modulator of synaptic transmission. Adenosine is a purine nucleoside, potent vasodilator of cerebral pial vessels, and an important metabolic factor in cerebral autoregulation. Cerebral adenosine concentrations are rapidly increased within seconds of a change in cerebral perfusion pressure as well as with a reduction of arterial blood pressure (hypotension) [Win85].

1.3.3 Shear-Stress Response

Shear-stress regulation is initiated by the endothelium producing nitric oxide in response to an increased shear stress on the vessel wall and is caused by viscous friction of blood and the vessel wall. The nitric oxide release is controlled by mechanoreceptors in the endothelium. Nitric oxide is a potent vasodilator, which is released into the lumen and causes an increase is vessel diameter and therefore an increased cerebral blood flow [Pet11]. A change in transmural pressure elicits an altered state of the myosin and actin filaments, which can be characterized by two biophysical pathways: the nitric oxide/endothelium-derived relaxing factor (EDRF) and the endothelium-derived hyperpolarization factor (EDHF). Both of these pathways are shown in Figure 1.4. Nitric oxide is a diffusible second messenger and EDHF is triggered only when the other pathway is inhibited. A flowchart depicting the role of endothelins is given in Figure 1.5. When binded to, ET_A and ET_B receptors can

act as vasoconstrictors and vasodilators, respectively. However, the long-lasting effects of endothelins imply that they are poorly suited for minute-to-minute CBF regulation [Pet11]. Cerebral arteries dilate in response to a decreased hydrodynamic shear stress. The shear response is important to long-term cerebrovascular tone and vascular remodeling and is
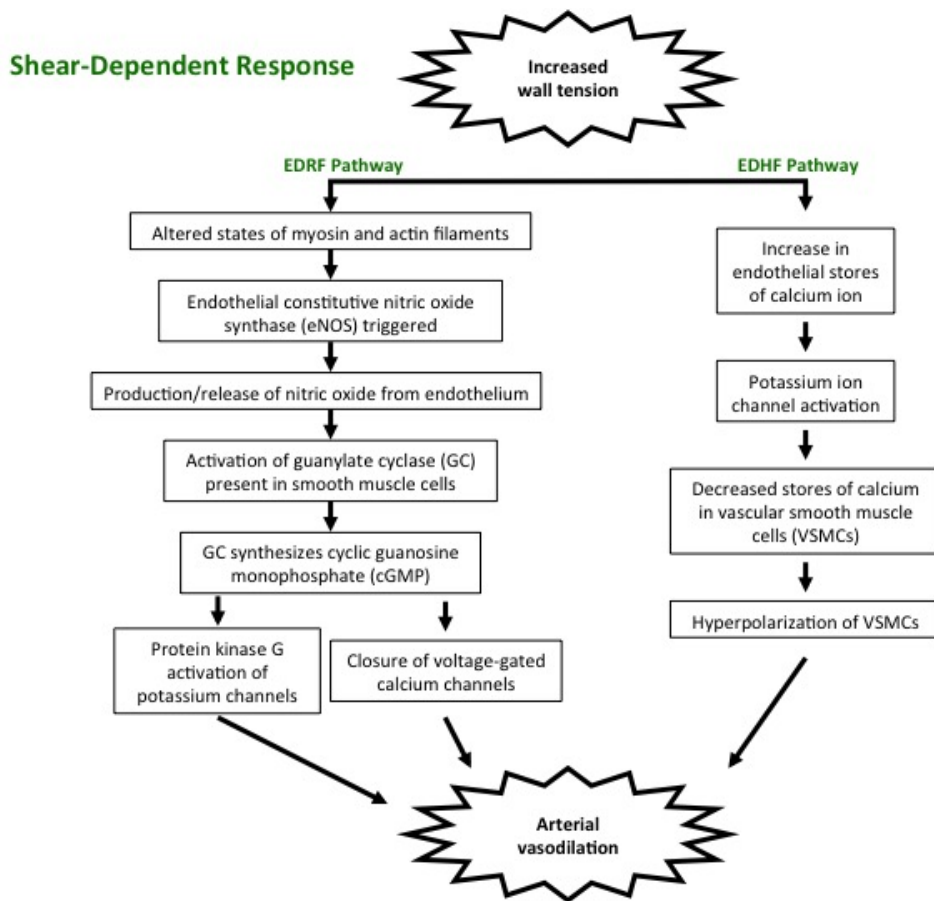
Figure 1.4 Shear-Stress Response. In response to a decreased blood pressure, vasodilation of the cerebral arterioles can be accomplished through the release of nitric oxide, a potent vasodilator, via the endothelium-derived relaxation factor (EDRF) pathway. If EDRF pathway is inhibited, vasodilation can occur via the endothelium-derived hyperpolarization factor (EDRF). In this pathway, changes in stores of calcium ions cause a subsequent hyperpolarization of vascular smooth muscle cells (VSMCs).
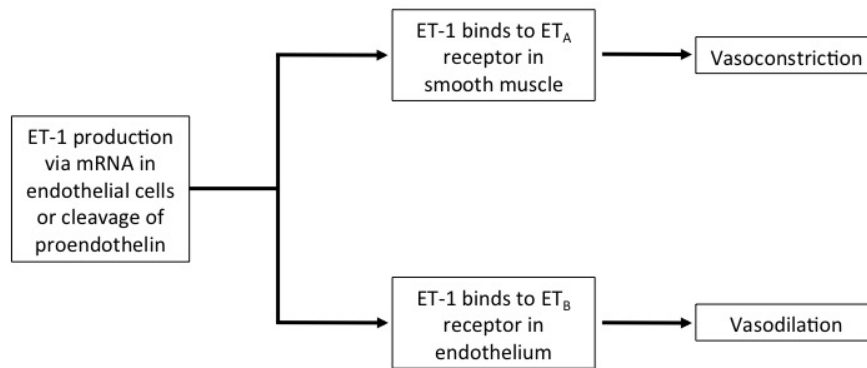
Figure 1.5 Shear-Stress Response. A change in flow through an artery is sensed by endothelial cells, which can release endothelins. These endothelins can bind to ET_A or ET_B receptors to cause vasoconstriction or vasodilation, respectively.

often coupled with the myogenic response.

1.3.4 Neurogenic Response

The fourth mechanism of cerebral autoregulation is the neurogenic response (see Figure 1.2). This response is described by the interactions between the intracranial nerves and cerebral vessels. By increasing the activity of the nerves within and surrounding the brain by stimulation, CBF is influenced by the response of the neurons. Unfortunately, not much is known about the physiology and exact relationship between the intracranial nerves and vessels. Little work has been done relating the vascular response to the stim-

ulation of the nervous system in the brain because measuring the local neural behavior is extremely difficult. The intracranial nervous system can be divided into two categories based on the location of the nerves, the intrinsic and extrinsic nerves. The intrinsic nerves are found on the interior of the brain and throughout the brain substance, which innervate the cerebral vessels. The nerves surrounding the brain that feed into the pial vessels are known as extrinsic nerves. The stimulation of these nerves influences CBF during CA.

The intrinsic nerves differ in their effect on cerebral blood flow based on their location within in the brain matter. When stimulated, the neurons within these parts of the brain can affect CBF. When the ganglia within the medulla, midbrain, forebrain, and cerebellum are stimulated, the increase in neuronal activity causes an increase in CBF. However, an increase in activity within the points leads to a decrease in CBF [EK02; Hal11]. The extrinsic nerves have been shown to have a direct influence on CBF. The extrinsic system can be divided among three pathways: the parasympathetic, sympathetic, and sensory pathways. An increase in parasympathetic activity, the rest-and-digest response, causes an increase in CBF. When the sympathetic neurons are stimulated, they cause a decrease in CBF. When there is an increase in sensory activity, the nerves respond by increasing blood flow. Some studies have shown these direct correlations, but the evidence is not completely conclusive about the relationship between the neurovascular response involved with CA [EK02].

There is evidence suggesting that the sympathetic nervous innervation plays a permissive role in CA responses. Sympathetic nerve stimulation extends the upper limit of autoregulation; where as, acute sympathectomy or inhibition of the effects of neuropeptide Y shift the lower limit of autoregulation toward a lower blood pressure. The precise roles of the autonomic nervous system on CA are still contended, but recent studies indicate a role

for the autonomic system in CA and the need to study its effects more closely. In particular, neural innervation of the human brain provides a mean by which cerebral vessel caliber can be altered without changes in perfusion pressure, local metabolic needs, or arterial blood gases [Goa04].

1.3.5   Cerebral Autoregulation and Aging

The human cardiovascular system experiences many age-related changes, including decreases in systemic artery compliance [Fle86] and increases in systolic ABP [Kan78]. Rat studies have shown that cerebral arterioles have reduced distensibility and undergo atrophy during aging [Haj90]. Additionally, aging leads to widening of cerebral arterial vessels [Kre99] and is responsible for a decrease in both cerebral blood flow velocity (CBFV) and cerebral blood volume [Car00]. Gender differences in the elderly have been studied [Dee10], concluding that elderly women have better vascular function than elderly men and that women autoregulate better than men. Almost all elderly humans have a blockage of some small cerebral arteries. Approximately ten percent of elderly people eventually have enough blockage to cause a stroke [Hal16]. Since the most common type of stroke is blockage of the middle cerebral artery, TCD measurements from the MCA are typically used for CA assessment. Vessels are not only stiffer in aging, but also are bigger. It remains unclear whether or not autoregulation is preserved in aging.

1.3.6   Cerebral Autoregulation and Disease

Autoregulation is an essential protective mechanism of the brain and plays an important role in numerous physiological and pathological phenomena. Reductions in CA have

been reported in various disease states, including hypertension [Eam03], severe head injury [Czo96], ischemic stroke [Eam02], carotid artery disease [Rei08], obstructive sleep apnea [Urb08], and Parkinson's disease [Vok07]. In subjects with impaired CA, the brain becomes excessively sensitive to fluctuations in blood pressure and complete autoregulation failure has been associated with higher rates of morbidity and mortality [Hu08]. Additionally, having an incomplete Circle of Willis may present more issues for individuals with cerebrovascular disease.

Hypertension is a major risk factor for cerebrovascular diseases [Fuj95]. It causes enlargement and remodeling of the cells in the vessel wall, which reduces the maximum dilatation of cerebral arterioles. Increased vascular resistance in hypertension decreases CBF in elderly hypertensives to the level observed in healthy young subjects [Str73]. This increased resistance is a result of structural changes in the smaller resistance vessel, characterized by narrowed arterioles with thickened walls [CY72]. These thickened arterioles remain greatly constricted all the time to prevent transmission of the high pressure to the capillaries [Hal16]. The presence of hypertension reduces the cerebrovascular response to changes in the arterial partial pressure of CO_2 [Mae94].

1.4   Static CA vs. Dynamic CA

In general, cerebral autoregulation can be separated into two distinct components: static and dynamic. Static cerebral autoregulation (sCA) represents the steady-state relationship between mean ABP and mean CBF, typically illustrated by the Lassen curve [Las59]. The curve, shown in Figure 1.6, contains a plateau between 60 mmHg and 150 mmHg. The plateau throughout this region indicates a constant CBF for changes in ABP, although the
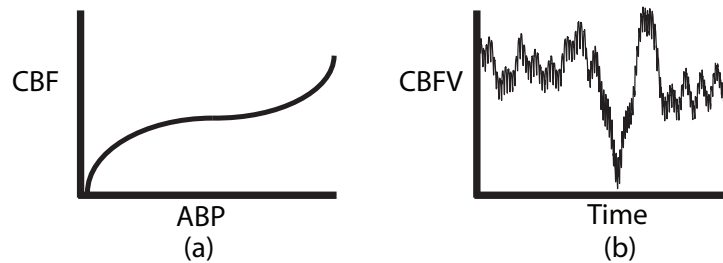
Figure 1.6 Cerebral Autoregulation. (a) The classical and theoretical steady-state relationship between cerebral blood flow and arterial blood pressure. Typically referred to as the Lassen Curve [Las59], the static relationship between ABP and CBFV has a plateau region between 50 and 150 mmHg. When the blood pressure is within this region, autoregulation remains intact. Outside this region, CBF changes linearly with pressure [HP14]. (b) The transient response of CBFV to a perturbation in ABP is studied through the concept of dynamic cerebral autoregulation. Following a change in ABP, the autoregulatory mechanisms are triggered to return the CBFV back to its baseline value.

curve does not necessarily have a slope of zero over the interval [Ros95; Urs95]. Evaluation of sCA is conducted by quantifying the difference in cerebral blood flow before and after the autoregulatory response to an alteration in blood pressure. If CBF remained approximately constant, then CA is intact. Conversely, if the CBF changes significantly, then CA is said to be impaired [Tie95].

A majority of the early studies on CA were performed on a static basis. Recent advances in measurement instruments, e.g. transcranial Doppler ultrasonography (TCD), have allowed for continuous monitoring of ABP and CBFV. The increased use of these measurements has led to the distinction between sCA and dynamic cerebral autoregulation (dCA). Following an ABP perturbation under normal conditions, CBF returns to its original value with a time constant of a few seconds. The transient process of how cerebral blood flow

is regulated following fluctuations in arterial blood pressure is referred to as dCA. Reproducibility and variability remain in the forefront of current studies in the assessment of dCA. Reproducibility describes the variability between repeated measurements within a subject; where as, variability refers to differences between subjects within a group of subjects [Elt14]. Improvements in this area are essential before its diagnostic value can be fully appreciated and confidently assessed [Pan09]. When studying hemodynamic regulation, experimental arterial blood pressure and cerebral blood flow velocity data can be collected through many different techniques.

1.4.1 Measuring ABP and CBFV

When assessing cerebral autoregulation, it is imperative to obtain both ABP and CBFV measurements. ABP data can be obtained invasively by the insertion of an arterial line, where a needle is placed in an artery and connected to a pressure transducer. While this method provides the most accurate pressure readings, there is a high risk associated with these measurements and therefore they are typically only performed on intensive care patients. The most common non-invasive technique for continuous measurement of ABP is the Finapres, shown in Figure 1.7. This device is based on the vascular loading technique, where a pressure is applied to a peripheral artery to maintain arterial blood volume constant by matching this applied pressure to the arterial blood pressure. The resulting ABP provides a continuous measurement with high temporal resolution. Since the Finapres device is used on the finger, experimentalists assume that the peripheral ABP is the same in both the brain and the finger. Peterson et al. [Pet14] found that both non-invasive and invasive methods produce similar cerebral autoregulation metrics.

Collection of CBFV data can be obtained through a number of techniques, with the most common procedure being transcranial Doppler (TCD) ultrasonography [Pan98]. The TCD technique utilizes the Doppler shift to estimate the velocity of red blood cells in blood vessels [Aas82], typically in the middle cerebral artery. TCD allows for continuous non-invasive measurements of CBFV with enough time resolution to analyze the dynamic variability in the signal. TCD is used to record CBFV as a surrogate of CBF, and the conversion from velocity (CBFV) to flow (CBF) assumes that the cross-sectional area remains constant along the vessel, an issue that is eloquently described in [Gil03]. The strength and accuracy of the CBFV signal is dependent on insonation angle, see Figure 1.7.

1.4.2   Assessing Autoregulation

When studying cerebral autoregulation, there are two types of experimental data used. Some studies analyze CBFV response to induced changes in ABP; where as, other studies assess the relationship between naturally occurring variability in the ABP and CBFV signals. Changes in ABP can be obtained by several maneuvers, including sit-to-stand, head up tilt, lower body negative pressure, Valsalva maneuver, and thigh cuff [Pan01]. Although these experiments generate a rapid change in ABP, some human subjects cannot tolerate the procedures. Since there is not a gold standard approach, many authors use the protocol of their choice. Often the protocol chosen depends on the CA assessment method used [Cla16]. The sit-to-stand technique has become a widely-used procedure for inducing orthostatic stress because it simulates an activity that humans encounter in their everyday life. Van Beek et al. [Bee10] concluded that the sit-to-stand test gives an increase in coherence due to increased power spectral density in both ABP and CBF. When compared to the thigh cuff
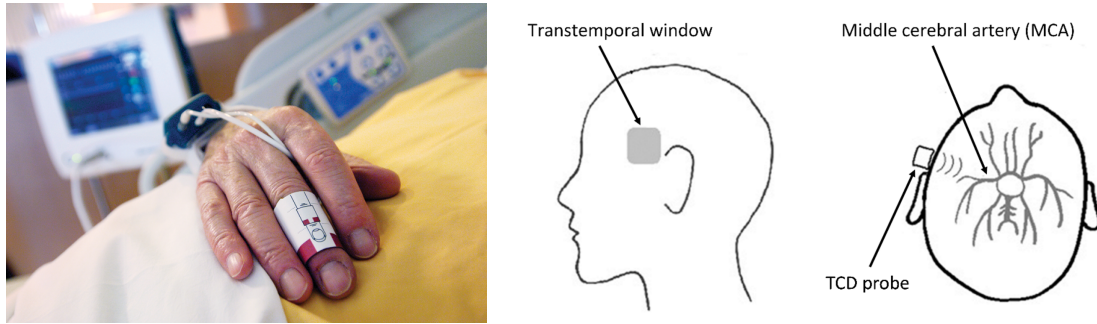
Figure 1.7 Measuring ABP and CBFV. Autoregulation is typically studied by analyzing ABP and CBFV signals. *Left:* ABP is commonly measured using the Finapres device. Reprinted with permission from [Mar12]. *Right:* Noninvasive measurements of CBFV in the middle cerebral artery can be obtained using transcranial Doppler (TCD) ultrasonography. Adapted and reproduced with permission from [Lu14].

procedure, Sorond et al. [Sor09] showed that there is greater tolerance for the sit-to-stand test and smaller within-subject variability in autoregulation measures. In clinical settings, naturally occurring ABP and CBFV time series are typically studied because it is more pleasant for the patient [Pay16]. For example, it is uncommon to induce pressure changes in intensive care patients that have suffered from stroke or traumatic head injury.

1.5   Open Questions

The underlying mechanisms that cause impairments in autoregulatory function are not fully understood. Furthermore, the links and distinctions between local autoregulation and global blood flow regulation (e.g. neurological, baroreflex, neurovascular coupling) are still widely debated. The effects of gender on the effectiveness of cerebral autoregulation are currently being studied. Understanding gender differences, if there are any, could be a great

contribution to the field, especially when considering hormonal changes in women due to pregnancy. Another open question relates to the concepts of sCA versus dCA. These topics are very different in definition. When it comes to experimental protocol, it is important to understand which one is being measured (if not both). Additionally, the shifting of the theoretical CA curve in the presence of various disease states is not completely known. Lastly, the need for a gold standard approach to assessing CA is of utmost importance [Cla16]. There continues to be variation in the clinical implementation of assessment techniques for autoregulation. The lack of a standardization within field proves difficult for comparing studies and arriving at consistent conclusions.

1.6 Outline

This study contributes to the field of cerebral autoregulation by combining modeling with data analysis techniques. The main objective is to take on the open questions associated with distinguishing between groups and investigating the role of pulsatility. We start by reviewing current contributions to modeling cerebral autoregulation (in Chapter 2) and techniques used to analyze the model developed here (in Chapter 3).

Chapters 4 and 5 (published and submitted papers) present a simple, nonlinear ordinary differential equation model that is capable of predicting cerebral blood flow velocity as a function of arterial blood pressure on a patient-specific basis. Initial qualitative testing (Chapter 4) is included to show that our model captures the physiological assumptions and definitions of cerebral autoregulation. Structural identifiability, practical identifiability, sensitivity analysis, parameter estimation (Chapters 4 and 5), and nonlinear mixed effects techniques (Chapter 5) are developed and used for model validation. Model results are

focused on showing how our model contributes to the discussion of differentiating dynamic autoregulatory responses in healthy young, healthy elderly, and hypertensive elderly human subjects (Chapter 5). Specifically, we show that by including the nonlinearity of cerebral autoregulation and some pulsatility from the input blood pressure, the model is able to quantify differences in autoregulatory response due to aging and hypertension.

Possibilities for model extension are discussed (Chapter 6), with the intentions of incorporating physiological principles and addressing the theoretical shifts of the autoregulation curve. Finally, a discussion is included in Chapter 7, addressing the advantages and disadvantages of the simple model analyzed here. Given its simplicity, the model has potential to be incorporated in the prediction of an autoregulatory index, allowing for more nuanced analysis in clinical settings. Since the model requires an input stimulus incorporating a significant change in pressure, more work is needed to assess if it has potential to assess cerebral autoregulation in patients with traumatic head injury, one of the most important clinical applications. Finally, we discuss (based on results in Chapter 6) how more physiological mechanisms can be accounted for, in particular associated with potential shifts observed in the static cerebral autoregulatory curve.

CHAPTER

2

CEREBRAL AUTOREGULATION

MODELING

As discussed in Chapter 1, cerebral autoregulation (CA) is typically studied using two perspectives: static and dynamic. Static CA refers to the net effect a change in ABP has on CBF, represented by the static Lassen curve [Las59]. Dynamic CA refers to the time-varying response to a perturbation in ABP. Numerous authors have tried to explain either static or dynamic aspects of CA [Urs88a; Gil90; Tie95; UL97; Czo97; UL98; Zha98; Urs00; Olu00;

LA02; Liu03; Ban05; Pay06; Spr12], resulting in two different modeling methodologies: physiologically-based compartment models and black box methods. Physiologically-based models and statistical black-box approaches are often focused on obtaining different objectives.

2.1 Lumped Compartmental Models

A common theme in lumped compartmental models is that they are inherently based on the physiological mechanisms effecting the system. Some model parameters can be known a priori through literature reviews and previous studies. Estimated parameter values from physiological models can often be extrapolated to real-world application. These approaches range from simple models relating pressure and flow to complex models with detailed descriptions of the CA pathways. The models are primarily developed to predict qualitative features rather than to fit clinical data. Numerous physiologically-based approaches exist, and many of them hinge on the techniques and concepts used by Ursino and his colleagues [Urs88a; UL97; UL98; Urs00].

2.1.1 Ursino & Colleagues

In 1988, Mauro Ursino first attempted to model whole brain circulation [Urs88a]. He used an electrical equivalent circuit model of cerebral circulation and incorporated autoregulation by assuming that arterial conductance is adjusted in response to changes in driving pressure through a low-pass filter with gain and time constant. The model showed good agreement with experimental simulations [Urs88b]. This formulation is the fundamental basis for all

subsequent models of autoregulation proposed by Ursino and colleagues.
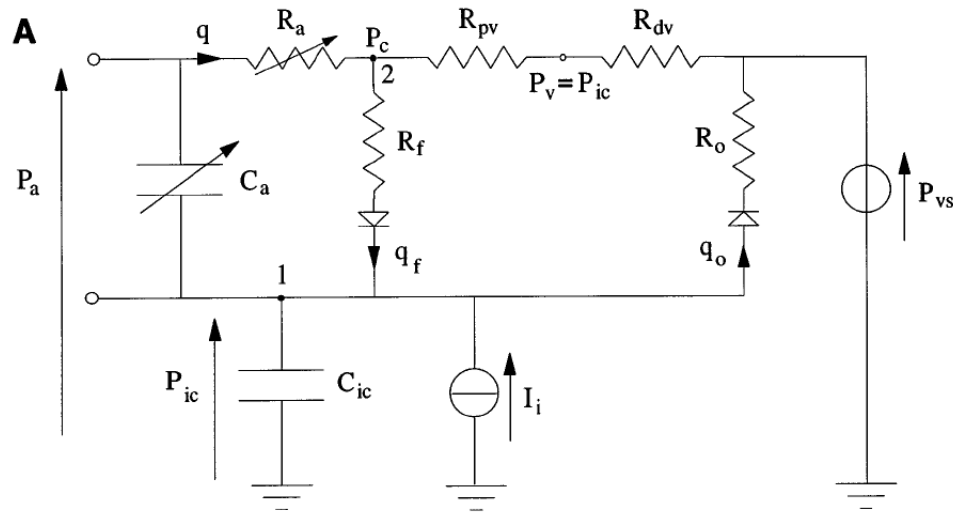
Figure 2.1 Ursino-Lodi Model (1997). Electrical analog of intracranial dynamics according to the 1997 Ursino and Lodi model. Cerebral blood flow (q) enters the brain at a pressure approximately equal to the systemic arterial pressure (P_a), and then passes through the arterial-arteriolar and venous cerebrovascular beds. Flow regulation is incorporated through the arterial compliance capacity (C_a). Adapted and reproduced with permission from [UL97].

In 1997, Mauro Ursino and Carlo Lodi developed a mathematical model of the interaction between intracranial pressure (ICP) and cerebral hemodynamics. An electrical analog of the intracranial dynamics of cerebral circulation associated with this model is shown in Figure 2.1. The goal of the model was to present a drastically simplified model of ICP dynamics useful for the study of patients with severe brain disease [UL97]. They believed that certain physical phenomena could be described in a very simple way without deterioration in model performance. Two main simplifications were made. No distinction was made between proximal and distal segments of the arterial-arteriolar cerebrovascular

bed, meaning that only one arterial-arteriolar segment, extending from large intracranial arteries down to cerebral capillaries, was included. Also, they assumed that the pressure at the terminal points of the large cerebral veins was equal to ICP. This assumption is based on the idea that the cerebrovascular beds behave as Starling resistors. In other words, CBF only depends on the difference between arterial pressure and ICP and is independent of the downstream venous sinus pressure.

The four CA mechanisms are lumped together into one term, describing the static CA curve. The model was compared against steady-state clinical data. Ursino and Lodi were able to predict patterns of pulsatile ICP changes and show how ICP responds to vasodilation and vasoconstriction stimuli. Although they were able to obtain these clinical results, they were forced to compromise between accuracy in the reproduction of the physiological reality and simplicity. Overall, this model is simple, physiologically reliable, and usable in neurosurgery intensive care units.

Since it is the foundation for a lot of models by other authors, let's derive the 1997 model by Ursino and Lodi. Throughout the development of the model, please reference Figure 2.1. Recall that blood flow velocity can be expressed as a function of flow (q) and cross-sectional area (A_c), given by $v = \frac{q}{A_c}$. This stems from the relationship with electrical currents. Flow, pressure, and compliance can be related to their electrical equivlances of current, voltage, and capacitance, respectively. This parallel with electrical currents allows the use of Ohm's law to describe the flow q:

$$q = \frac{p_a - p_c}{R_a} = \frac{\text{arterial blood pressure} - \text{capillary blood pressure}}{\text{arterial flow resistance}}.$$

The difference between ABP and capillary blood pressure can be denoted Δp and

represents the pressure difference across a vessel. The pressure gradient can be defined as

$$\Delta p = \frac{8\mu L q}{\pi r^4} = \frac{8(\text{fluid viscosity})(\text{vessel length})(\text{flow})}{\pi(\text{inner radius})^4}.$$

Assuming the volume of a single vessel (V_a) can be written as $L\pi r^2$, then a new expression for the pressure change can be obtained.

$$\Delta p = \left(\frac{L\pi r^2}{L\pi r^2}\right)\frac{8\mu L q}{\pi r^4} = \frac{8\mu\pi L^3 q}{\pi^2 L^2 r^4} = \frac{8\mu\pi L^3 q}{(\pi L r^2)^2} = \frac{k_R q}{V_a^2},$$

where k_R is a constant parameter. Also, since $\Delta p = R_a q$, arterial resistance (R_a) can be defined:

$$R_a q = \frac{k_r q}{V_a^2} \rightarrow R_a = \frac{k_R}{V_a^2}.$$

By applying a volume balance equation for the capillaries, the volume of blood flowing into the capillaries should be the approximate volume flowing out of the capillaries, assuming that the volume of blood plasma absorbed by tissues is negligible:

$$q = \frac{p_a - p_c}{R_a} = \frac{p_c - p_v}{R_{pv}}.$$

By assuming that the venous pressure in the cerebral capillaries is equal to the intracranial pressure ($p_v = p_{ic}$), an expression for capillary pressure can be obtained:

$$p_c = \frac{p_a R_{pv} + p_{ic} R_a}{R_{pv} + R_a}.$$

Now assume that the pressure-volume relationship of the cerebral arteries to be $V_a =$

$C_a(p_a - p_{ic})$. In other words, stressed arterial volume is approximately equal to compliance. Relating to the intracranial pressure-volume relation: $p_{ic} = p_{ic0}e^{k_E V_{ic}}$, where V_{ic} is the stressed intracranial volume, p_{ic0} is the reference pressure at which $V_{ic} = 0$, and k_E is the intracranial elastance. The total intracranial volume (V_{ic}) is composed of cerebrospinal fluid volume (V_{CSF}), intracranial tissue volume (V_{tiss}), arterial blood volume (V_a), and venous blood volume (V_v). V_{tiss} and V_v are constant with time. Thus,

$$V_{ic}(t) = V_{CSF}(t) + V_{tiss} + V_a(t) + V_v.$$

Using these equations, cerebral hemodynamics can be described with a single nonlinear ODE for intracranial pressure (p_{ic}), given by

$$\frac{dp_{ic}}{dt} = \frac{k_E p_{ic}}{1 + C_a k_E p_{ic}}\left[C_a \frac{dp_a}{dt} + \frac{dC_a}{dt}(p_a - p_{ic}) + \frac{p_c - p_{ic}}{R_f} - \frac{p_{ic} - p_{vs}}{R_0} \right]$$

One assumption of note is that the rate of change in the CSF volume is equal to the difference between CSF formation and outflow. Constant model parameters are the elastance coefficient (k_E), cerebrospinal fluid formation resistance (R_f), cerebrospinal fluid outflow resistance (R_0), and dural sinus pressure p_{vs}. Model input consists of arterial blood pressure (p_a) and the rate of change of arterial pressure ($\frac{dp_a}{dt}$).

Ursino and Lodi envisioned that CBF is maintained by the regulation of vascular tone, which is achieved by the control of arterial compliance (C_a), given by the equation

$$\frac{dC_a}{dt} = \frac{1}{\tau}[-C_a + \sigma(x)].$$

Here, τ represents a relaxation constant and σ denotes the autoregulatory control function, given by

$$\sigma(Gx) = \frac{(C_{an} + \frac{\Delta C_a}{2}) + (C_{an} - \frac{\Delta C_a}{2})e^{\frac{Gx}{k_\sigma}}}{1 + e^{\frac{Gx}{k_\sigma}}}.$$

The saturation limits are described using ΔC_a, k_σ denotes the central slope of the static autoregulation curve, and G represents the maximum autoregulatory gain. The model output is cerebral blood flow velocity, and is a function of the computed radius of the middle cerebral artery [UL97].
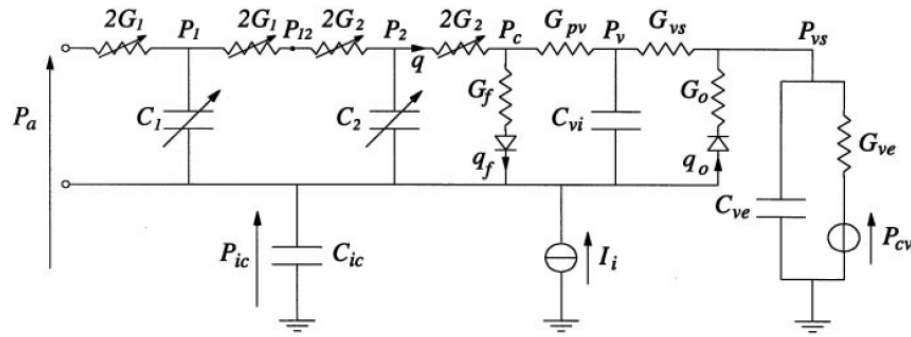
Figure 2.2 Ursino-Lodi Model (1998). Electrical analog of intracranial dynamics according to the 1998 Ursino and Lodi model. This is an extension of the previous approach by Ursino and Lodi including CO_2 reactivity in the pial arterial circulation. The model was used to analyze the nonlinear interaction of CO_2 reactivity with autoregulation. Reprinted with permission from [UL98].

One year after their initial paper, Ursino and Lodi further developed their model to show the interaction among autoregulation, CO_2 reactivity, and intracranial pressure [UL98]. To do this, they decided to separate the microcirculation and macrocirculation. They considered the cerebrovascular bed to consist of four compartments (see Figure 2.2), each

responding independently to changes in pressure. The aim of this study was to significantly improve and extend the previous model to include the CO_2 reactivity of cerebral vessels, its nonlinear interaction with ICP and CA, and the description of the Transcranial Doppler velocity signal. They hoped by developing this new model, that they would be able to show that cerebral autoregulation and chemical metabolic regulation can be summarized into a single theoretical setting. They also wanted to improve the interpretation of clinical maneuvers concerning cerebrovascular control and ICP dynamics.

Model results showed the importance of the role of CO_2 reactivity, and that one must consider the different sizes of arterial vessels in the brain when modeling the CBF regulation system. Although they did not consider the effects of the neurogenic response on CA, they were able to specifically accomplish four main goals with the 1998 model. When holding ICP constant, they were able to analyze CA, CO_2 reactivity, and the interactions between CA and CO_2 reactivity. Lastly, they were able to analyze the effect of acute changes in CO_2 on ICP [UL98]. The plots of cerebral blood flow as a function of both arterial blood pressure and partial pressure of carbon dioxide are validated against animal experimental data [Mac79; Har79].

The original model from 1988 was used to model ICP dynamics in patients with acute brain injury [Urs95]. Results from that study revealed that intracranial pressure is governed by blood flow changes, cerebrospinal fluid dynamics, and changes in blood volume. The two arterial compartment model [UL97] was simplified back into one arterial compartment with feedback based on flow and arterial CO_2 [Urs00].

2.1.2 Similar models

The work of Ursino and his colleagues forms the basis for models created by other authors. Olufsen et al. [Olu02] developed a lumped, three-element windkessel model for cerebral blood flow regulation consisting of two resistors and a capacitor. The aim of the Olufsen model was to better understand the cardiovascular response to hypotension, and found that the initial increase in cerebrovascular resistance is responsible for the widening of the blood flow pulse in young subjects. The model output, generated using time-varying parameters, was validated using pulsatile CBFV data from the sit-stand manoeuvre [Lip00]. Czosnyka et al. [Czo97] developed a model for bedside testing of cerebrovascular autoregulation which was very similar to the model by Ursino and Lodi. The model by Banaji et al. [Ban05] is used extensively. It uses the model form the 2000 study by Ursino et al. [Urs00], but replaces the two feedback equations with a detailed model of the biochemical pathways.
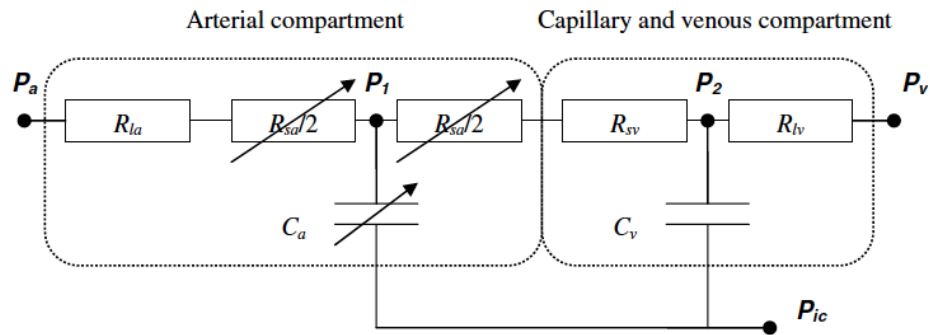
Figure 2.3 Payne Model Schematic. This approach uses a lumped model to predict the response of cerebral vasculature to changes in neural stimulation, arterial blood pressure, and arterial CO_2 concentration. Cerebral blood flow is controlled in an additive manner through these three feedback mechanisms. Reprinted with permission from [Pay06].

In 2006, Payne [Pay06] proposed a simple lumped model that included neural activity, partial CO_2 arterial pressure, and blood flow influence on compliance (see model schematic in Figure 2.3. These influences were represented in the model by state equations and were assumed to affect the compliance of the arterioles. The Payne model [Pay06] is very similar to the in vivo prediction model [Urs00], but includes the contribution from neural activation and is thus able to draw upon validation data from three physiological challenges. The model can be thought of as two parts, the first contributing to the hemodynamics of the blood vessel and the second pertaining to the autoregulatory mechanisms. Model analysis shows a large correlation between brain autoregulation and neural activation processes. The model exhibited the classic autoregulation curve and other qualitative characteristics of cerebral blood flow. Payne found that incorporating a sigmoidal curve was useful in getting cerebral autoregulatory characteristics because it provided limits to the extent that cerebral autoregulation could influence the hemodynamic system.
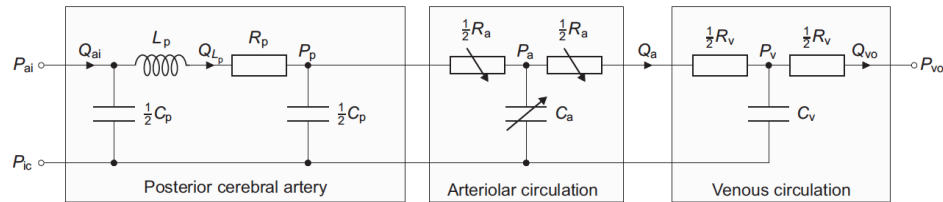
Figure 2.4 Spronck Model Schematic. This is a lumped model of the posterior cerebral artery and its distal venous and arteriolar beds. Blood flow regulation is exerted at the arteriolar level by vascular smooth muscle and all four autoregulatory mechanisms are included. Reprinted with permission from [Spr12].

In 2012, Spronck et al. [Spr12] created a lumped parameter model that demonstrates

the mechanisms involved with cerebral autoregulation and neurovascular coupling. A schematic of the model is provided in Figure 2.4. The change in CBF due to increased brain activity is known as neurovascular coupling. Because the same mechanisms are involved in both processes, this paper aims to model the mechanisms involved in order to study the dynamical effects of cerebral autoregulation and neurovascular coupling on cerebral blood flow as well as the influence of each mechanism involved. All four mechanisms of cerebral autoregulation are considered: myogenic, shear stress, metabolic, and neurogenic responses.

The model by Spronck et al. [Spr12] is of similar structure to the work of Ursino and colleagues. It is composed of three compartments: the posterior cerebral artery (PCA), the venous circulation, and the arteriolar circulation. The model is composed of a combination of Ursino and Lodi's model [UL98] and Payne's model [Pay06]. The schematic for the model is shown in Figure 2.4, which describes the interaction of the equations involved in the model. The four mechanisms of CA are modeled by their regulatory state and regulatory action. The entire model considers the simulation of nine state equations: three for the PCA, one for venous circulation, one for arteriolar circulation, four for the regulatory mechanisms, and one for the CO_2 concentration. The first-order model is qualitatively compared to actual patient data in order to determine the success of the model.

To imitate the qualitative behavior of the clinical data obtained, MATLAB simulations were run in order to optimize the parameters and the fit quality was measured by the root mean square error. Some parameters were kept constant based on previous models that determined a significant value for each. In eleven subjects, five of the feedback gains and time constants are fitted to data and the parameter values show consistency across the

subject group. Model results concluded that the myogenic response plays a larger role in regulating CBF when arterial blood pressure is fluctuated more than shear stress regulation. The model shows that the metabolic response cannot be responsible for neurovascular coupling solely. The relationship between the neurogenic and metabolic responses is important because they directly influence one another (coupled). This model has the advantage that the different feedback mechanisms are more explicitly included.

2.1.3   Other approaches

A myriad of autoregulatory studies exist, with some focusing on the detailed physiological mechanisms of cerebral autoregulation and others attempting to simply describe the complex mechanisms using a simple model. Kashif et al. [Kas12] used a model-based approach to continuously estimate intracranial pressure from CBF velocity and ABP noninvasively. A simplified model focusing on brain tissue, cerebral vasculature, and cerebrospinal fluid was considered.

The study by David et al. [Dav09] develops a non-dimensional representation of both myogenic and metabolic responses coupled with an asymmetric binary tree algorithm simulating the cerebrovasculature structure. The end results of the two mechanisms given in this paper are presented for an autoregulation algorithm of the cerebrovasculature downstream of the efferent (conveying away from a central organ or section) arteries, such as the middle cerebral artery.

The David et al. paper is believed to be the first model that includes a full arterial tree algorithm shown in an autoregulation mechanism. The authors demonstrated the arterial wall model and asymmetric binary tree model. The arterial wall model is adapted from the

Gonzalez-Ferrandez and Ermentrout (GFE) model to simulate the complete motion of the arterial wall, known as the Maxwell unit. The GFE model utilizes differential equations to simulate Ca^{2+} variations in smooth muscle via Ca^{2+} and Ca^{2+}-dependent K^+ ion channel open probabilities. The arterial wall model consists of four equations with a power exponent, for the relationship between parent and daughter vessels, and an asymmetry ratio. The overall function for the asymmetric tree model is to imitate the vascular system from a major artery, like the middle cerebral artery.

The authors were able to conclude that the myogenic response has a greater influence on CA than the metabolic response from their analyses. Since this appears to be one of the first models that utilizes the complete vascular tree, the authors state that the combination of a CA model with a fully populated arterial tree remains relatively unexplored and more work should be done with this concept [Dav09].

Works by Arciero et al. [Arc08; Car08] focus on the development of a theoretical segmental model of blood flow regulation. Although the models describe regulation in skeletal muscle, they have recently been extended to retinal autoregulation [Arc13] and can be applicable for modeling cerebral autoregulation. The possible extension of the work by Arciero et al. to cerebral autoregulation will be explored further in Chapter 6.

2.2   Black Box Methods

The general idea behind the black box approaches is to provide a non-invasive assessment of dynamic CA in the resting state. All of the techniques use spontaneous fluctuations in blood pressure and cerebral blood flow velocity. Using spontaneous mean arterial blood pressure fluctuations can be quite advantageous. Since no clinical maneuvers need to be performed,

these methods may be used in a wider range of patients, particularly those who are unstable or unable to cooperate with or tolerate the challenges required to provoke a hemodynamic response. Unlike the physiologically-based models above, black box approaches allow for continuous, non-invasive monitoring of cerebrovascular function. The two most commonly used black box methods for assessment of autoregulation are transfer function analysis (TFA) and the autoregulatory index (ARI). The TFA [Zha98] results in a phase and gain spectrum; where as, the ARI method [Tie95] describes the system response to a step-like disturbance and is graded on a scale of 0 to 9. One problem with these approaches is that spontaneous MABP fluctuations must be of sufficient amplitude in order to obtain reliable estimates of the dCA parameters [Elt14].

Regardless of the method used for CA assessment, raw experimental data are preprocessed. To obtain preprocessed data, pulsatile ABP and CBFV are low-pass filtered using zero-phase 4th-order Butterworth filter, in both the forward and reverse directions, with cutoff frequency of 20 Hz (see [Pan00]). Subsequently, the beginning and end of each cardiac cycle are marked by the onset of the systole using ABP signal. The onsets are detected using a windowed and weighted slope sum function and adaptive thresholding [Zon03]. The beat-to-beat average of ABP and CBFV are calculated for each detected cardiac cycle. A first-order polynomial is then used to interpolate the resulting time series, which is followed by downsampling at 10 Hz to produce signals with a uniform time base. Preprocessed ABP and CBFV time series are used in the modeling approaches described below.

2.2.1 Transfer Function Analysis

One tool for CA assessment is transfer function analysis (TFA), which was first conducted by Giller [Gil90] and later applied to dynamic CA by Zhang et al. [Zha98]. The TFA method aims to analyze the frequency domain relationship between oscillations in blood pressure and cerebral blood flow velocity. This approach is based on the notion that CA minimizes the effect of spontaneous pressure oscillations on the duration, magnitude, and frequency in the velocity signal. The method of transfer function analysis has been used extensively in the investigation of cardiovascular control, respiratory sinus arrhythmia, and renal autoregulation [Sau91; Sau89; HR91]. Spectral analysis, which can be performed with the fast Fourier transform (FFT), transforms time series of ABP and CBFV to the frequency domain. Define $S_{xx}(f)$ to be the autospectrum (power spectrum) of changes in the input signal (ABP) and $S_{xy}(f)$ to be the cross spectrum between the input and output (CBFV) signals [Ain08]. The cross spectrum, also called the cross-spectral, is the Fourier transform of the cross-correlation function, which is a measure used in signal processing describing the similarity of two series as a function of the lag of one relative to the other [BP10]. The transfer function between the two signals can then be calculated according to

$$H(f) = \frac{S_{xy}(f)}{S_{xx}(f)}. \tag{2.1}$$

From the transfer function, the relative power (gain) and timing (phase) can be described using the real ($H_R(f)$) and the imaginary ($H_I(f)$) parts of the complex transfer function:

$$\text{gain: } \left|H(f)\right| = \sqrt{|H_R(f)|^2 + |H_I(f)|^2}$$
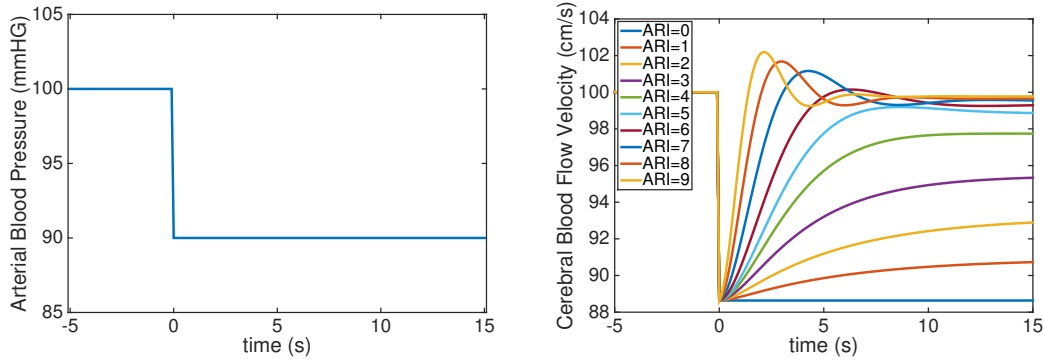
Figure 2.5 Autoregulation Index. Cerebral Blood Flow Velocity (CBFV) for various ARI values according to the arterial blood pressure step response input (left).

$$\text{phase: } \phi(f) = \arctan\left[\frac{H_I(f)}{H_R(f)}\right].$$

Calculation of the magnitude-squared coherence gives an estimate of the reliability of the relationship between the two signals:

$$\text{coherence: MSC}(f) = \frac{|S_{xy}(f)|^2}{S_{xx}(f)S_{yy}(f)},$$

where $S_{yy}(f)$ is the autospectrum of changes in CBFV. The coherence, which represents the linear association between the fluctuations in blood pressure and cerebral blood flow, is sometimes used as a measure of CA function. Impairment of CA is indicated by a coherence of close to one.

2.2.2 Autoregulatory Index

The autoregulatory index (ARI) method uses preprocessed ABP data (dP) as an input to the Tiecks' model [Tie95] to predict cerebral blood flow velocity. Even though this method is

ARI	T	D	K
0	2.00	0	0
1	2.00	1.60	0.20
2	2.00	1.50	0.40
3	2.00	1.15	0.60
4	2.00	0.9	0.8
5	1.90	0.75	0.90
6	1.60	0.65	0.94
7	1.20	0.55	0.96
8	0.87	0.52	0.97
9	0.65	0.50	0.98

Table 2.1 Autoregulatory Index. Corresponding values of T, D and K parameters for each ARI value.

known for its uncertainty and lack of reproducibility, it has been the focus of many recent studies [Cla16; Mah16]. Similar to several of the methods described above, this approach uses beat-to-beat average BP as an input to predict CBFV. The input is typically normalized according to the expression

$$dP = \frac{P - \bar{P}}{\bar{P} - P_{cr}},$$ (2.2)

where $P_{cr} = 12\,\text{mmHg}$ is the critical closing pressure [Tie95].

There are both continuous and discrete formulations of the Tiecks method. Regardless of the version used, for a prescribed input pressure stimulus, combinations of ten different values of (T, D, K) are used to generate ten models corresponding to various grades of autoregulation ranging from 0 (absence of autoregulation) to 9 (strongest/fastest autoregulation), see Figure 2.5 and Table 2.1. The associated ARI value is determined by finding the minimal difference between the predicted ($\hat{V}$) and measured CBFV (V).

We will only consider the continuous formulation of the Tiecks model [Tie95]. This

formulation estimates the CBFV using a second-order linear differential equation system with input pressure dP and state variables x_1 and x_2.

$$\frac{d x_1}{d t} = \frac{1}{T}(-x_2 + dP) \tag{2.3}$$

$$\frac{d x_2}{d t} = \frac{1}{T}(x_1 - 2D x_2), \tag{2.4}$$

where T and D are the time constant and damping factor parameters, respectively. The predicted flow velocity $(\hat{V})$ is calculated using the equation

$$\hat{V} = \overline{V}(1 + dP - K x_2), \tag{2.5}$$

where $\overline{V}$ is the mean velocity and K is a parameter reflecting autoregulatory gain. To solve a system, appropriate initial conditions must be determined. Assuming that at rest, the system is at steady state. Initial conditions can be determined from setting Equations (2.3)-(2.4) equal to zero.

$$\frac{1}{T}(-x_2 + dP) = 0$$

$$\frac{1}{T}(x_1 - 2D x_2) = 0.$$

The first ODE is zero when x_2 is equal to the input pressure dP. The second ODE is zero when $x_1 = 2D x_2$. Thus, to efficiently start the data-driven ARI method, initial conditions of $x_2(0) = dP(0)$ and $x_1(0) = 2D dP(0)$ should be used.

2.2.3 Other Approaches

Aside from TFA and ARI, other statistical black-box approaches exist. Autoregressive exogenous (ARX) and autoregressive-moving average (ARMA) are extensions of the previously discussed methods [LA02; Liu03]. The pulsatility index (PI) can be used to reflect cerebrovascular resistance [Gos71]. This index is defined as the difference between systolic and diastolic extremes of CBF velocity divided by the mean CBF velocity. Another tool that is used is the rate of recovery (RoR), which is defined as the normalized changes in the cerebrovascular resistance index per second during a decrease in blood pressure [Aas89]. This method has not yet been tested in an elderly population. Although most of the black box methods can be used to analyze clinical data, they are rather limited in explaining physiological mechanisms underlying CA.

2.3 Conclusion

While modeling autoregulation varies between phenomenological methods and conceptual approaches, it is evident that research within the field of cerebral hemodynamics is ever-growing. The brain is of high importance, since it influences and controls many of the other systems within the human body. The model developed in Chapter 4 is an extension of the Tiecks model [Tie95] to account for important features of cerebral autoregulation. We aim to create a simple model (few parameters) capable of estimating cerebral blood flow velocity given any pressure stimulus. Before discussing the model and the motivation behind its development, let's discuss a few methods that can be used for model validation and analysis.

CHAPTER

3

MATHEMATICAL METHODS

In Chapter 2, numerous methodologies for modeling cerebral autoregulation were described. Despite the vast differences between the structures of the models, many of the same mathematical tools can be used for model validation and analysis. This chapter will introduce the analysis tools used to examine the model developed and presented in Chapters 4 and 5, including identifiability analysis, sensitivity analysis, subset selection, and parameter estimation. Throughout this chapter we use the previously developed ARI model [Tie95] as an example for application of the techniques.

3.1 Identifiability

Structural identifiability addresses the question of whether it is possible to uniquely infer the model parameters given perfect and noise-free data. Practical identifiability establishes if the model parameters can be determined uniquely given a specific (noisy) dataset. Thus, if possible, structural identifiability should be considered before practical identifiability as it is a necessary condition [Mia11; Mah14; MS14]. The importance of practical identifiability stems from the fact that for many models, only some data is available. Thus even if the model is structurally identifiable, it may only be possible to estimate a small subset of model parameters [OO13]. If a model is unidentifiable, the parameters can take an infinite number of values and still produce the same response. This can cause serious problems when estimating parameters. Structural identifiability can also reveal identifiable combinations of parameters, commonly referred to as correlated parameters. These combinations can cause issues during parameter estimation, but reparameterization can be used to restructure the model, creating an identifiable input-output equivalent to the original model.

Both analytical and numerical approaches can be used for identifiability analysis. Perhaps the most effective analytical method for structural identifiability testing is the differential algebra approach, which uses substitution and differentiation to eliminate all variables in the model except for the observed output [Aud01]. Equations can be reduced using Gröbner bases and characteristic sets to eliminate the unmeasured variables, eventually yielding input-output (I/O) equation(s). This equation relates the model input (e.g. pressure) with the model output (e.g. flow). Using the coefficients of the I/O equation, one can test model identifiability. Structural identifiability is determined by whether the

corresponding coefficient map is one-to-one. If the I/O equation has a unique solution, then it is one-to-one and the model is structurally identifiable in the variables. Simpler forms for identifiable combinations and identifiable reparameterizations for the model can also be obtained from the I/O equation. Structural identifiability analysis, which includes the calculation of the input-output equation for our model, is used in Chapter 4 (see Equations (4.14)-(4.15)).

Another analytical approach is the Laplace transform method, which can only be used on linear models. Consider the transfer function $H(w, \theta)$ associated with some linear model, parametrized by θ, where θ belongs to an open subset $\mathscr{D}_T \subset^m$, and consider the equation

$$H(w, \theta) = H(w, \theta^*) \qquad \text{for almost all } p, \tag{3.1}$$

where $\theta, \theta^* \in \mathscr{D}_T$. Then, the model structure is said to be globally identifiable if (3.1) has a unique solution in $\mathscr{D}_T$, locally identifiable if (3.1) has a finite number of solutions in $\mathscr{D}_T$, and unidentifiabile if (3.1) has a infinite number of solutions in $\mathscr{D}_T$. Other analytical methods for identifiability analysis include Taylor series and similarity transform.

Analytical methods sometimes have limited applicably and oftentimes can be slow. To remedy, a variety of numerical approaches exist. One numerical approach uses the Fisher Information Matrix (FIM), which is a $N_p \times N_p$ matrix representing the amount of information that the model output has about the model parameters p. The FIM can be

calculated via the matrix product $X^T X$, where X is the design matrix, given by

$$X = \begin{bmatrix} \dfrac{\partial y(t_1)}{\partial p_1} & \cdots & \dfrac{\partial y(t_1)}{\partial p_n} \\[2ex] \vdots & \ddots & \vdots \\[2ex] \dfrac{\partial y(t_m)}{\partial p_1} & \cdots & \dfrac{\partial y(t_m)}{\partial p_n} \end{bmatrix}.$$

When errors are normally distributed, the FIM is determined using $X^T W X$, where W is a weighting matrix. The rank of the FIM denotes the number of identifiable parameters and parameter combinations. The FIM can be used to find blocks of related parameters and subsequently how many parameters to fix during estimation. Structural identifiability can often be detected by variances in the covariance matrix, which hinges on theory behind the Cramer-Rao bound ($\text{FIM}^{-1} \leq \text{Cov}(p)$).

Another numerical method for identifiability analysis is profile likelihood [Rau09], which focuses on exploring one parameter at a time by fixing it to a range of values and fitting the rest of the model parameters. When analyzing the curvature of the profile likelihood, flat or nearly flat regions indicate identifiability issues. By generating simulated perfect noise-free data, structural identifiability can be tested. Other numerical methods for identifiability analysis exist, including some Bayesian approaches [Ran02].

3.1.1 Example: ARI Model

Recall the ARI model system given in Equations (2.3)-(2.5). To check the structural identifiability of the model, we compute the I/O equation. Let p denote the ARI model input (formerly dP) and $\hat{V}$ represent the model output. First, differentiate the output, Equa-

tion (2.5) and replace $d x_2 / d t$ with the expression in Equation (2.4) to get

$$\frac{d \hat{V}}{d t} = \bar{V} \frac{d p}{d t} - \frac{\bar{V} K}{T} x_1 + \frac{2 D \bar{V} K}{T} x_2.$$

Solving Equation (2.5) for x_2, substituting the result into the expression above, and rearranging yields

$$\frac{d \hat{V}}{d t} = \bar{V} \frac{d p}{d t} - \frac{\bar{V} K}{T} x_1 - \frac{2 D}{T} \hat{V} + \frac{2 D}{T} \bar{V} + \frac{2 D}{T} \bar{V} P.$$

Differentiate to get

$$\frac{d^2 \hat{V}}{d t^2} = \bar{V} \frac{d^2 p}{d t^2} - \frac{\bar{V} K}{T} \frac{d x_1}{d t} - \frac{2 D}{T} \frac{d \hat{V}}{d t} + \frac{2 D}{T} \bar{V} \frac{d p}{d t}.$$

Next, replace $d x_2 / d t$ with the expression in Equation (2.4), substitute in the expression for x_2, divide through by $\bar{V}$, and rearrange to get

$$\frac{d^2 p}{d t} + \frac{2 D}{T} \frac{d p}{d t} + \frac{1 - K}{T^2} p = \frac{d^2 \hat{V}}{d t^2} + \frac{2 D}{T} \frac{d \hat{V}}{d t} + \frac{1}{T^2} \frac{(\hat{V} - \bar{V})}{\bar{V}}.$$

Lastly, multiply through by T^2, yielding the input/output equation

$$T^2 \frac{d^2 p}{d t} + 2 D T \frac{d p}{d t} + (1 - K) p = T^2 \frac{d^2 \hat{V}}{d t^2} + 2 D T \frac{d \hat{V}}{d t} + \frac{(\hat{V} - \bar{V})}{\bar{V}}.$$

The structural identifiability is determined by whether the coefficient map

$$\phi(T, D, K) = \left[T^2, 2 D T, 1 - K \right] \tag{3.2}$$

is one-to-one. This has a unique solution and thus the ARI model is structurally identifiable.

3.2   Sensitivity Analysis

To analyze the general ability of the model to fit the data, the sensitivity and practical identifiability problem must be considered. Practical identifiability can be determined by analysis of the sensitivity matrix. To define sensitivities, assume that the model can be written as

$$\frac{dx}{dt} = f(t, x; \theta),$$

where t denotes time, x represents the state vector, and θ is the parameter vector. Also assume that the output can be computed as

$$y = g(t, v; \theta),$$

where g is an algebraic function dependent on time t, the states x, and the parameters θ. The sensitivity of the model output (y) to the model parameters can be estimated using the sensitivity matrix, given by

$$S = \frac{\partial y}{\partial \theta}.$$

Notice that the structure is equivalent to the design matrix previously defined. Each column of the sensitivity matrix, denoted S_i for $i = 1, \dots, n$ where n is the total number of model parameters is a time-varying vector that measures how sensitive the model output is to a given parameter at a time t. Sensitivities can be determined analytically as solutions to the sensitivity equations [VJ08], as well as by using finite differences [Pop09] or automatic

differentiation [Ell08].

Given that model parameters do not have the same units, sensitivities cannot easily be compared across the parameter space. To remedy this problem, relative sensitivities can be calculated by scaling the sensitivity matrix S relative to the parameter and the time-varying data. The relative sensitivity matrix is defined by

$$\tilde{S} = \frac{\partial y}{\partial \theta} \frac{\theta}{y}.$$

(3.3)

For the purpose of parameter identification, it can be useful to rank the model parameters according to their sensitivity. Insensitive parameters are typically difficult to identify. Ranked sensitivities can be obtained by imposing a two-norm on each column of the sensitivity matrix

$$\bar{S}_i = ||S_i||_2,$$

(3.4)

or along each column of the relative sensitivity matrix

$$\bar{S}_i = \left|\left|\tilde{S}_i\right|\right|_2.$$

(3.5)

These ranked sensitivities can be sorted from most to least sensitive, and are typically scaled so that the most sensitive parameter has sensitivity equal to one. For model outputs predicted numerically, parameters for which the ranked sensitivity $S_{\theta i} < \sqrt{\xi}$, where ξ is the tolerance of the ODE solver, are insensitive. In addition to being insensitive, parameters may also be correlated [Tho09; Jac85; Dau08; Mia11]. Practical identifiability and sensitivity analysis are used in Chapters 4 and 5.

3.2.1 Example: ARI Model

Sensitivity analysis provides insight into how model output changes with respect to parameter values. Consider the ARI model [Tie95]. Sensitivity equations can be formulated to see how parameters for autoregulatory gain (K), damping factor (D), and time constant (T) can effect the model output. The sensitivities with respect to the model output are

$$\frac{\partial \hat{V}}{\partial T} = -K x_{2T}$$

$$\frac{\partial \hat{V}}{\partial D} = -K x_{2D}$$

$$\frac{\partial \hat{V}}{\partial K} = -K x_{2K} - x_2,$$

where $x_{2T} = \frac{\partial x_2}{\partial T}$, $x_{2D} = \frac{\partial x_2}{\partial D}$, and $x_{2K} = \frac{\partial x_2}{\partial K}$. Absolute, relative, and ranked sensitivities can be determined numerically by solving the following dynamical system of intermediate

variables and their sensitivities,

$$\frac{d\,x_1}{d\,t} = \frac{dP - x_2}{T}$$

$$\frac{d\,x_2}{d\,t} = \frac{x_1 - 2D\,x_2}{T}$$

$$\frac{\partial\,x_{1T}}{\partial\,t} = -\frac{1}{T^2}dP + \frac{1}{T^2}x_2 - \frac{1}{T}x_{2T}$$

$$\frac{\partial\,x_{1D}}{\partial\,t} = -\frac{1}{T}x_{2D}$$

$$\frac{\partial\,x_{1K}}{\partial\,t} = -\frac{1}{T}x_{2K}$$

$$\frac{\partial\,x_{2T}}{\partial\,t} = -\frac{1}{T^2}x_1 + \frac{1}{T}x_{1T} + \frac{2D}{T^2}x_2 - \frac{2D}{T}x_{2T}$$

$$\frac{\partial\,x_{2D}}{\partial\,t} = \frac{1}{T}x_{1D} - \frac{2}{T}x_2 - \frac{2D}{T}x_{2D}$$

$$\frac{\partial\,x_{2K}}{\partial\,t} = \frac{1}{T}x_{1K} - \frac{2D}{T}x_{2K} \tag{3.6}$$

where $x_{1T} = \frac{\partial\,x_1}{\partial\,T}$, $x_{1D} = \frac{\partial\,x_1}{\partial\,D}$, $x_{1K} = \frac{\partial\,x_1}{\partial\,K}$, $x_{2T} = \frac{\partial\,x_2}{\partial\,T}$, $x_{2D} = \frac{\partial\,x_2}{\partial\,D}$, and $x_{2K} = \frac{\partial\,x_2}{\partial\,K}$. Classical sensitivites (see Figure 3.1(A)) and relative sensitivities (see Figure 3.1(B)) give insight to the time-dependent importance of the parameters. Ranked sensitivities for the ARI model are provided in Figure 3.1(C), from which the parameter representing the time constant (T) is the most sensitive parameter. All three sensitivities were calculated for the model developed in this study, described in detail in Chapters 4 and 5.

(A)   (B)   (C)
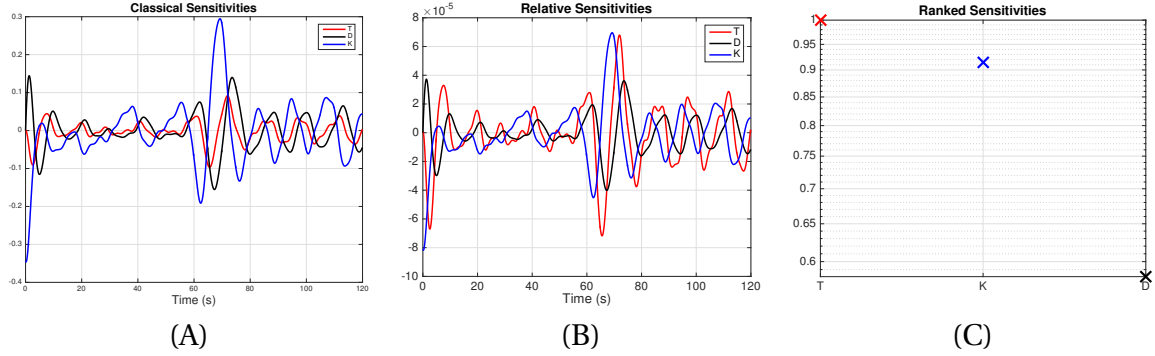
Figure 3.1 ARI Model Sensitivities. Plots of the classical (A) and ranked (B) sensitivities against time show how sensitive the ARI model output is to a given parameter at a time t. For the purpose of parameter identification, it can be useful to rank the model parameters according to their sensitivity. When looking at the ranked sensitivities (C) for the ARI model, the time constant (T) is the most sensitive and the damping factor is the least sensitive.

3.3 Subset Selection

The structured correlation analysis method can be performed to explore possible pairwise correlations among sensitive model parameters [OO13]. Using the sensitivity matrix S, the correlation matrix c can be computed from the covariance matrix $C = (S^T S)^{-1}$ (assuming it is not singular), as

$$c_{i,j} = \frac{C_{i,j}}{\sqrt{C_{i,i}\, C_{j,j}}}. \tag{3.7}$$

The covariance matrix exists assuming the matrix product $S^T S$ is not singular, i.e. $\det(S^T S) \neq 0$. The correlation matrix c is symmetric with $\left|c_{i,j}\right| \leq 1$ and all $\left|c_{i,i}\right| = 1$. A parameter pair (i, j) is pairwise correlated when $|c_{i,j}| > \epsilon$ for some threshold value ϵ. The criteria, i.e. the choice value for ϵ, can be chosen by the researcher, where a value closer to 1 indicates a stronger pairwise correlation.

Other methods for subset selection include the orthogonal method [Mia11], and using

49

singular value decomposition of the sensitivity matrix followed by QR factorization [Pop09]. Structured correlation analysis was performed on the model developed in this thesis (see Chapters 4 and 5).

3.3.1 Example: ARI Model

Structured correlation analysis was performed on the ARI model, yielding the correlation matrix

$$
\begin{array}{ccc}
T & D & K
\end{array}
$$
$$
\begin{array}{c}
T \\
D \\
K
\end{array}
\left(
\begin{array}{ccc}
1.00 & -0.64 & -0.58 \\
-0.64 & 1.00 & 0.77 \\
-0.58 & 0.77 & 1.00
\end{array}
\right)
$$

Assuming a cutoff criteria of $|\epsilon| = 0.95$, no parameters in the Tiecks model [Tie95] are pairwise correlated. Thus, parameters T, D, and K are estimable. The ϵ used here is consistent with the criteria used in Chapters 4 and 5. This is not a set value and is oftentimes a matter of choice, but parameters close to this value should be investigated more carefully.

3.4 Parameter Estimation

After addressing the identifiability of a model, estimates of identifiable model parameters can be performed. Parameter estimation is a large field with lots of different optimization methods that can be used. Additionally, parameter estimation is significantly easier to perform successfully and efficiently with good nominal parameter values.

3.4.1 Least Squares Optimization

Nonlinear least squares optimization is used to estimate parameters by minimizing the least squares cost $J = R^T R$, where R is a matrix of residuals describing the difference between the model output and the observed data evaluated at times t_i where the data are measured.

One method for least squares optimization is the Nelder-Mead simplex algorithm [NM65], which can be implemented using the *fminsearch* command in Matlab. This algorithm minimizes the cost through direct search. A simplex, which is a triangle in h dimensions, is generated using the initial guess for the h parameters. Nelder-Mead compares the values of the function at the three vertices of the triangle, then eliminates and replaces the vertex with the largest cost. This process is repeats and is eventually terminated once the cost at the vertices converges to a single value.

Another optimization tool is the Levenberg-Marquardt method [Kel99], which is easily implemented in Matlab using the *nlinfit* and *newlsq_v2* scripts. This method combines gradient descent and Gauss-Newton algorithms. The gradient descent method updates the parameters in the direction of steepest descent, and then, assuming the least squares function is locally quadratic, the Gauss-Newton method finds the minimum of the quadratic. Parameter estimation is used in Chapters 4 (see Equation (4.20)) and 5 (see Equation (5.13)) to quantify patient-specific model parameters associated with the dynamic autoregulatory response.

3.4.2 Example: ARI Model

To identify the three ARI model parameters, parameter estimation was performed using the Levenberg-Marquardt method. Figure 3.2 shows the ARI model output $\hat{V}$ plotted against the beat-to-beat CBFV data from a sample dataset [Lip00]. The fit was generated using the optimal parameter values of $T = 1.36$, $D = 0.46$, and $K = 0.43$.
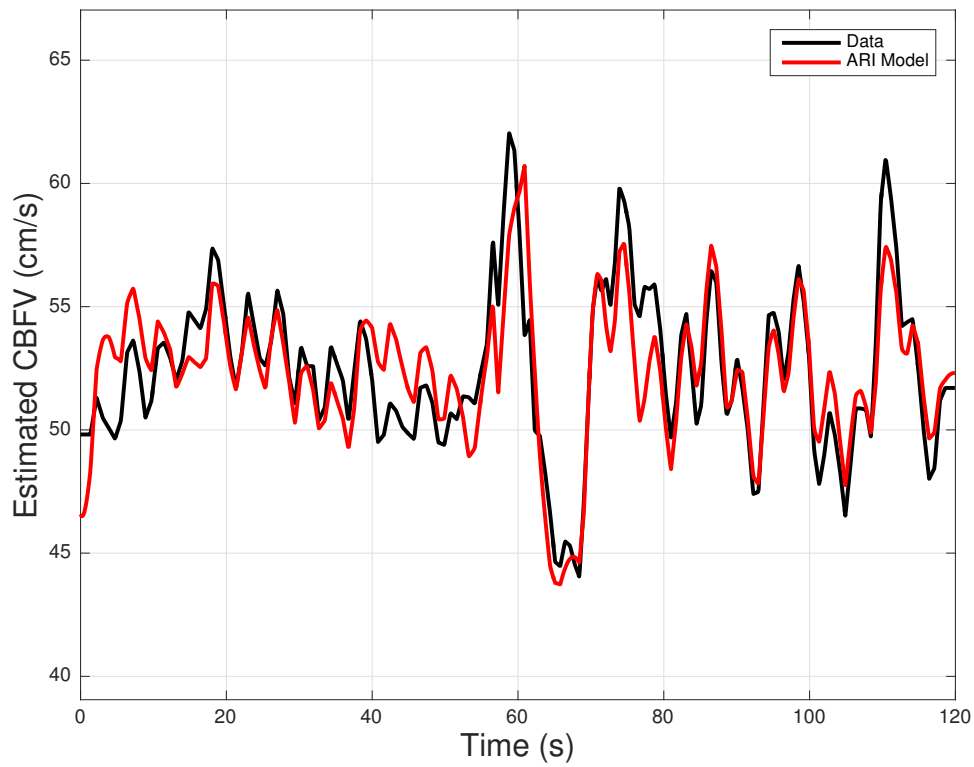
Figure 3.2 Parameter Estimation. Estimated parameter values were obtained for the ARI model using least squares optimization. Plots of the model output (red) and the averaged CBFV signal (black) from a sample dataset.

3.4.3   Nonlinear Mixed Effects Modeling

Most parameter estimation techniques are used on mathematical models to describe intra-subject variation. In order to analyze data from multiple subjects and extract valuable information about inter-subject variation, one can use nonlinear mixed effects (NLME) analysis. A mixed-effects model is one that includes both fixed effects and random effects. NLME models are constructed using a statistical framework that incorporates fixed effects for population parameters and random effects for the uncertainty associated with intra- and inter-subject variability [DG95; Bon11]. NLME analysis is a two stage process, where the first stage addresses intra-individual variability, and the second stage quantifies the inter-individual variability.

Stage 1 describes assay errors and model errors, according to $y_{i,j} = g(x_{i,j}, \phi_i) + e_{i,j}$ with $e_{i,j} \sim N(0, \sigma^2)$. For some initial condition $x(0) = x_0$, $\frac{dx}{dt} = f(t, x, u; \phi)$. Stage 2 addresses the uncertainty associated with inter-individual variability, $\phi_i = h(\theta, Z_i, \eta_i)$ using log-normal parameter distribution $\phi_i = \theta \cdot \exp(\eta_i)$, with $\eta_i \sim N(0, \Omega)$. Using the NLME method, estimates of population parameters for random effects (Ω), random effects (σ^2), and model parameters (θ) are obtained.

In the NLME analysis, the data are fitted to the same overall model as done in the least squares optimization method. However, unlike least squares, the NLME method gives insight into both intra- and inter-individual variation. The model parameters are assumed to vary randomly around their population value (the population median) with the associated variances quantifying the variability among subjects. A residual component is introduced to describe the within-subject variation. Compared to taking the average of the independently estimated individual parameter values, the NLME population estimate

gives an improved estimate of the population parameters. Additionally, if not enough data is available to estimate parameters for each subject, NLME modeling can help. The method can borrow data from other subjects in the population to get a population mean, and then parameters can be compared across populations with higher level of certainty [WZ06]. Nonlinear mixed effects modeling can be implemented in Matlab using the SimBiology GUI. Another option is the specialized software package NONMEM. It was developed by Lewis Sheiner and Stuart Beal and is commonly used in the analysis of pharmacokinetic and pharmacodynamic data [Bea11].

This section introduces the concept of NLME analysis used in Chapter 5 to analyze our model. It should be noted that NLME modeling included in Chapter 5 was performed by collaborators Timmermann and Ottesen. Due to the complex model structure, the commercial software NONMEM was used. The results using nonlinear mixed effects analysis are presented in Chapter 5.

3.5   Statistical Considerations

In later chapters, statistical analysis via location testing will be used to differentiate between subpopulations. Given data from two independent groups, location testing determines if the means of the data are equal, using the null hypothesis $H_0 : \mu_1 - \mu_2 = 0$. Using a two-sample t-test, the comparison of groups is performed by predicting p-values computed at a prescribed confidence level α. The test statistic is calculated using

$$T = \frac{\mu_1 - \mu_2}{\text{SE}},$$

where SE is the standard error, given by

$$\sqrt{\frac{s_1^2}{N_1} + \frac{s_2^2}{N_2}}.$$

Here, the s denote the sample variances and the N are the sample sizes. The two-tailed p-value is given by

$$p = P(t_{1-\alpha,\,\mathrm{DF}} < T) + P(t_{1-\alpha,\,\mathrm{DF}} > T),$$

where the degrees of freedom (DF) are determined using

$$\frac{(s_1^2/N_1 + s_2^2/N_2)^2}{\frac{(s_1^2/N_1)^2}{N_1-1} + \frac{(s_2^2/N_2)^2}{N_2-1}}.$$

To interpret, reject H_0 if $p < 0.05$.

CHAPTER

<div style="text-align:center">

4

MODELING CEREBRAL BLOOD FLOW VELOCITY DURING ORTHOSTATIC STRESS

</div>

This chapter presents, develops, and analyzes our nonlinear cerebral autoregulation model. We have chosen to include the entire text from our published paper, therefore some repetitions may appear redefining the methods used for model analysis. To make all definitions

clear, we have added comments to the text (in italics) to distinguish them from published text. The manuscript was written in collaboration with Mahdi and Olufsen, who mentored Mader in model development and analysis and contributed to proof reading the manuscript. As a first author, Mader was responsible for writing the text.

4.1 Motivation

The brain accounts for only 2% of human body mass, yet approximately one-fifth of the body's blood supply goes to the brain. Cerebral autoregulation (CA) is a term used to describe the ability of the brain to regulate cerebral blood flow (CBF) over a wide range of blood pressures. The system works by altering the local environment, keeping the flow at homeostasis under changes in arterial blood pressure (ABP). The flow of blood to the brain is modulated both by local and global mechanisms including myogenic, metabolic, shear-dependent, and neurovascular regulation. These four regulatory responses act collectively to maintain an approximately constant CBF and oxygen supply amidst ABP changes. Myogenic regulation [Pet11] operates by changing electrical properties of stretch-activated ion channels in arteriolar smooth muscle cells. Metabolic regulation [Pau90] refers to the negative feedback system operating to balance metabolic demand with oxygen delivery. This response is driven by the imbalance between cerebral metabolism (demand) and oxygen delivery through CBF (supply) and acts by means of a vasoactive substance. Shear-stress regulation [Spr12] responds to changes in wall stress imposed by changes in blood pressure and is coupled with the myogenic response. This mechanism facilitates the en-

dothelium producing nitric oxide due to the viscous friction of blood flow along the vessel wall. Lastly, the neurogenic component of autoregulation describes the interaction between intracranial nerves and cerebral vessels [HT14; Pet11]. While it has been established that these four CA mechanisms operate on different time-scales [UL98; Pay06; Lan07; Bla08] that are larger than a heart beat, the exact physiological mechanisms underlying observed dynamics are still under debate.

Generally CA is studied from two perspectives: static and dynamic. Static CA refers to the net effect a change in ABP has on CBF. It is typically illustrated by the CA curve, an s-shaped curve (see Figure 4.3) showing the range of ABP (approximately 50-150 mmHg) over which CBF is maintained [Las59]. Outside this range CBF change proportionally with changes in ABP. Dynamic CA refers to the time-varying response to an ABP perturbation. This is typically studied by analyzing adaptation following a step-increase in ABP. In clinical studies, an ABP change is typically induced by subjecting the patient to either postural or respiratory challenges such as head-up tilt, sit-to-stand, or CO_2 rebreathing [Bee08].

In this study, we assess CA using data measured during postural change from sitting to standing. Upon standing, in the upper body ABP drops due to gravitational pooling, while in the lower extremities ABP increases. This leads to a decrease in cardiac output and therefore a reduced flow to the brain. In response to this stimulus the autonomic and autoregulatory systems are activated. Baroreflex regulation restores blood pressure by regulating heart rate, cardiac contractility, and vascular tone, while CA responds via vasodilatation restoring blood flow to the brain.

Simultaneous recordings of ABP and cerebral blood flow velocity (CBFV) allow researchers to study dynamic adaptation. Figure 4.1 shows sample data from a sit-to-stand

experiment. We note that a drop in ABP leads to an immediate drop in CBFV, which is followed by a recovery, overshoot, and adaptation. This type of behavior resembles stress-strain responses observed in viscoelastic materials [Fun93], including large arteries [VJ11]. This study develops a CA model that can predict both static and dynamic responses to changes in ABP. For changes in ABP within the CA range, the model adapts to a baseline value of CBFV, while outside the CA range changes in CBFV are proportional to ABP.

Numerous authors have tried to explain both static and dynamic aspects of CA. A variety of physiologically-based models have been proposed [UL97; Urs00; Pay06; Spr12]. Ursino and Lodi used two-element [UL97] and three-element [UL98; Urs00] Windkessel models to predict dynamic autoregulatory responses to changes in cerebral perfusion pressure, arterial CO_2 pressure, and arterial compliance. Payne [Pay06] proposed a lumped parameter model that relates ABP, partial CO_2 arterial pressure, and neural stimulation to predict CBF and the change in hemoglobin. Spronck et al. [Spr12] developed a lumped parameter model that predicts static CA regulation including all four autoregulatory mechanisms. A common theme in these physiological models is that they include numerous parameters and were primarily developed to predict qualitative features rather than to fit clinical data. The physiologically-based models can be contrasted with statistical black-box approaches [Pan95; Czo96]. This group of methods includes the autoregulation index (ARI) [Tie95], autoregressive-moving average (ARMA), autoregressive exogenous (ARX) [LA02; Liu03], and transfer function analysis [Gil90; Pan96; Zha98]. Although most of these methods can be used to analyze clinical data, they are rather limited in explaining physiological mechanisms underlying CA.

This study combines the two modeling methodologies deriving a simple nonlinear

model that uses measured values of ABP as an input to quantitatively predict CBFV dynamics during postural change from sitting to standing. The model is motivated by the analysis of time-varying dynamics observed in the filtered and pulsatile measurements of ABP and CBFV. This analysis showed that CBFV responds nonlinearly to changes in ABP. We found it important to develop a model that incorporates the CA curve in order to distinguish between fluctuations in ABP. Perturbations of ABP within the CA range enable CBFV to return to baseline, whereas perturbations outside this range causes CBFV to follow changes in ABP. The objective of the present study is to derive a model motivated by physiology while still keeping it as simple as possible. The latter is important since it facilitates model-based analysis of large and patient-specific ABP/CBFV datasets by comparing the estimated parameters. This type of analysis allows parameters to play the role of autoregulatory indices, which can be compared within and between groups of subjects. In this study, the model is validated using ABP/CBFV data from a representative healthy young and healthy elderly subject, but future studies aim at obtaining model parameters using data from a larger cohort of subjects. More specifically, the present study addresses data analysis, model development, and shows how stability analysis, as well as structural and practical parameter identifiability methods can be used to demonstrate that the model displays correct qualitative and quantitative behavior. Finally parameter estimation is used to show that the model can fit CBFV measurements recorded during a postural change from sitting to standing.

4.2 Methods

4.2.1 Data

The sit-to-stand anonymized patient data analyzed in this paper were used with permission from Dr. Lipsitz, Hebrew SeniorLife, Boston, MA. The Institutional Review Board at Hebrew SeniorLife approved the study and all subjects provided written informed consent [Lip00]. Beat-to-beat arterial pressure was measured noninvasively in the middle cerebral artery (MCA) using a photoplethysmographic Finapres monitor (Ohmeda Monitoring Systems, Englewood, CO). The subject's nondominant hand was supported by a sling at the level of the right atrium to eliminate hydrostatic pressure effects. In order to minimize the effects of respiration, subjects were required to breathe at a rate of 15 breaths per minute with the assistance of tape-recorded cues. Test subjects also underwent Doppler ultrasonography by a trained technician in order to measure the changes in blood flow velocity within the MCA due to active postural changes. The 2 MHz probe of a portable Doppler system (MultiDop X4, DWL-Transcranial Doppler Systems Inc., Sterling, VA) was strapped over the temporal bone and locked in position with a Mueller-Moll probe fixation device to image the MCA. The MCA blood flow velocity was identified according to the criteria of Aaslid [Aas89] and recorded at a depth of approximately 50-65 mm. The blood flow velocity waveform, derived from a Fourier analysis of the Doppler frequency signal and continuous pressure signal, was digitized at 250 Hz and stored in the computer for later analysis.
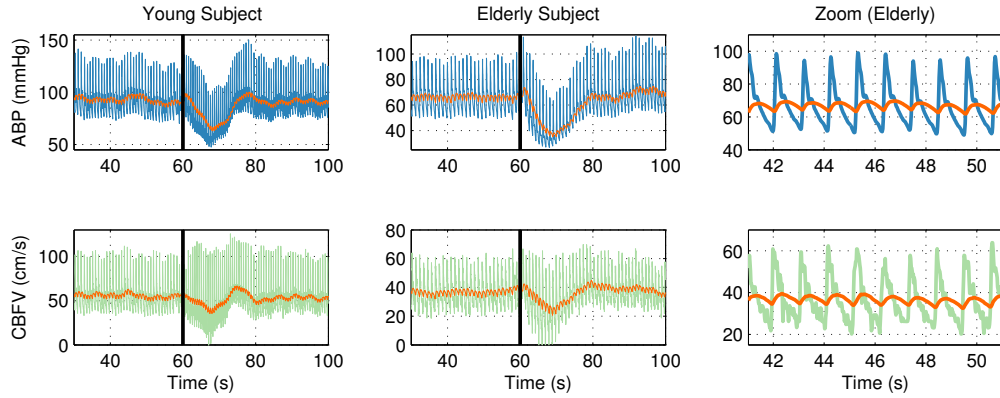
Figure 4.1 Trends in ABP/CBFV dynamics. Graphs show pulsatile and filtered ABP and CBFV data for a healthy young (left column) and a healthy elderly (middle column) subject during the sit-to-stand experiment. The black vertical lines mark the time at which the subjects stand.

4.2.2 Data Processing

To inspect the trends observed in the pulsatile ABP and CBFV data, a simple filtering procedure was applied to both signals. *We know there are several filtering approaches, reference previous papers. We do not implement the integral in Equation (4.1), but rather implement the ODE (see Equation (4.2)). Having the integral from $-\infty$ to t gives nicer form of differential equation.* The filtered signals $\bar{p}_a$ and $\bar{V}_{mca}$ are computed as weighted averages, where the present value is weighted higher than the past, according to the expression

$$\bar{x}(t) \;=\; \beta \int_{-\infty}^{t} x(s) e^{-\beta(t-s)} ds, \tag{4.1}$$

where $x \in \{p_a^d, V_{mca}^d\}$ is the pulsatile data and β (1/sec) represents the weighing parameter. Alternatively, differentiating Equation (4.1) we obtain

$$\frac{d\bar{x}}{dt} = \beta(x - \bar{x}). \qquad (4.2)$$

In this study $\beta = 1$ for both subjects. *Filtering was done by solving the differential equation in (4.2), corresponding to the integral in (4.1). This form of the integral is chosen to get a simple form for (4.2), which can be justified since $\int_{-\infty}^{0}$ is small. In this study all computations are done with $\beta = 1$. As we discuss in Chapter 5, varying beta allows us to account for more or less pulsatility in the model.* A smaller value of β, gives rise to smoother data at the cost of delaying arrival of peaks and troughs. Figure 4.1 shows the pulsatile and filtered ABP and CBFV data for a healthy young and a healthy elderly subject. A zoom (before postural change) of the data from the elderly subject is included to show inter-beat ABP and CBFV dynamics. The black vertical lines indicate when the subjects undergo postural change from sitting to standing, which causes pooling of blood in the legs. As a result, the ABP in the upper body drops, while lower body ABP (not measured) increases. In response, baroreflex, and autoregulation are activated, restoring ABP and CBFV to baseline levels. The young subject displays a larger overshoot before recovery than the elderly one; and the recovery time is longer in the elderly than in the young subject.

4.2.3   Model Formulation

The proposed model is partially based on the trends observed in the filtered ABP/CBFV (input/output) data. The drop in ABP during a postural change from sitting to standing
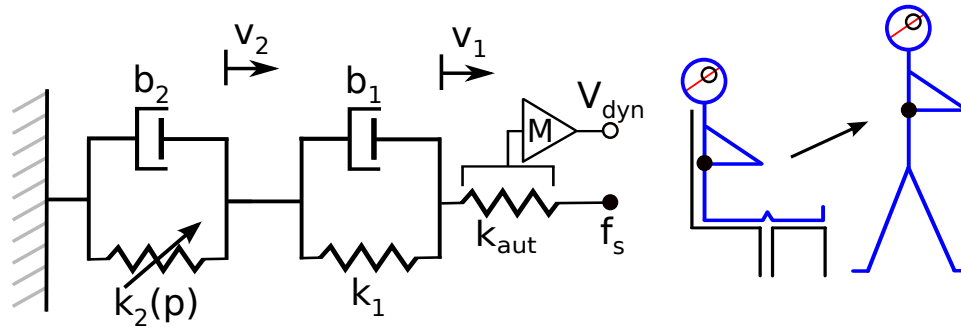
Figure 4.2 Mechanical analog used for predicting V_{dyn}**.** Schematic diagram depicting the mechanical analog model used for predicting the dynamic CA component V_{dyn}. The model includes two viscoelastic Voigt body elements combined with a spring accounting for the elastic portion of the response.

is a consequence of the blood volume redistribution triggered by gravitational forcing. Without active control systems, ABP would remain low, leading to a reduced flow to the brain. While the autonomic system is activated to restore blood pressure, CA maintains CBF relatively constant. The latter is facilitated by vessel dilatation/constriction. To understand how the body adapts to these changes, it is necessary to develop a dynamic model. The data demonstrate that the recovery time (the elapsed time between the minimum CBFV and the time at which CBFV returns to its baseline value) is longer in the elderly than in the young individual. For the young subject the recovery time is approximately 12 seconds, while it is 15 seconds for the elderly subject (see Figure 4.1). Conversely, the overshoot in the CBFV dynamics is larger in the young than in the elderly subject. Unfortunately, from the data used in this study it is not possible to determine what physical properties cause a larger overshoot in the young subject.

As noted earlier, the relationship between ABP and CBFV closely resembles strain-stress responses observed in viscoelastic-type materials [Flü75; Chr71; Mah14; VJ11], including

overshoot, adaptation, and a phase shift. It is well-known that blood vessels exhibit viscoelastic properties [Fun93]. Moreover, cerebral arteries responsible for regulating CBF contain collagen and the regulatory deformation is likely to be viscoelastic. The model developed in this study is empirical and we do not have data at intermediate stages to determine exactly what type of viscoelastic response is exhibited. In general, tissue shows a continuous relaxation in response to stress [Fun93], yet our previous study [Mah13] revealed that with two relaxation time-constants it is possible to fit the response to ABP changes. Inspired by these studies, we chose to use the model depicted in Figure 4.2, which includes two Voigt bodies connected with a spring. Further, we will show how the model's parameters can be related to features associated with the adaptation, recovery, and overshoot. It should be noted that this study only accounts for the CA response due to changes in pressure. The stimulus (see Figure 4.2) is denoted by f_s, which represents either mean or pulsatile ABP. Numerous studies (e.g. [BH85; HT14; WC13]) have attempted to predict the myogenic contribution to CA as a function of ABP, yet it is still unclear if CA responds to changes in mean or pulsatile pressure. To study the difference between these inputs, we consider two cases. The first case uses pulsatile pressure obtained via interpolating the measured ABP, i.e., $f_s = p_a^d$, and the second case explores the mean pressure stimulus predicted by interpolating the filtered pressure $f_s = \bar{p}_a$. To simplify notation in the remainder of this manuscript, we write $f_s = p$, where $p \in \{p_a^d, \bar{p}_a\}$.

The dynamic component of CA described above, predicts the transient response of CBFV to beat-to-beat fluctuations in ABP. Without any further model components CBFV would adapt to zero rather than to the given baseline flow. Therefore, to account for both dynamic adaptation and baseline flow, we assume that V_{mca}, representing CBFV in the

middle cerebral artery, is given by

$$V_{mca} = V_{bas} + V_{dyn},\tag{4.3}$$

where V_{dyn} models the transient character of the signal and V_{bas} is the baseline value of CBFV. The dynamic portion of CBFV is predicted by determining the strain-stress relationship on each mechanical element in the model (see Figure 4.2). Let ϵ_j and σ_j for $j = 0, 1, 2$ be the strain and stress associated with the spring and the two Voigt bodies. Following the diagram in Figure 4.2, we can write:

$$
\begin{aligned}
\epsilon_0 &= f_s - v_1 & \sigma_0 &= k_{aut}(f_s - v_1) \\
\epsilon_1 &= v_1 - v_2 & \sigma_1 &= k_1(v_1 - v_2) + b_1\left(\frac{dv_1}{dt} - \frac{dv_2}{dt}\right) \\
\epsilon_2 &= v_2 & \sigma_2 &= k_2 v_2 + b_2 \frac{dv_2}{dt}.
\end{aligned}
\tag{4.4}
$$

To incorporate the CA curve into our model, the spring k_2 is assumed to be a function of ABP, i.e., $k_2 = k_2(p)$. Since the two Voigt bodies and a spring are connected in series, the total stress equals to the stress on each element [Chr71], i.e., $\sigma_0 = \sigma_1$ and $\sigma_0 = \sigma_2$, yielding

$$
\begin{aligned}
k_{aut}(f_s - v_1) &= k_1(v_1 - v_2) + b_1\left(\frac{dv_1}{dt} - \frac{dv_2}{dt}\right) \\
k_{aut}(f_s - v_1) &= k_2 v_2 + b_2 \frac{dv_2}{dt}.
\end{aligned}
\tag{4.5}
$$

By making the following substitutions

$$a = \frac{k_{aut}}{b_1}, \quad b = \frac{k_{aut}}{b_2}, \quad c = \frac{k_1}{b_1}, \quad \text{and} \quad d = \frac{k_2}{b_2},\tag{4.6}$$

we obtain a simplified system of equations of the form

$$
\begin{aligned}
\frac{d v_1}{d t} &= -(a+b+c)v_1 + (c-d)v_2 + (a+b)f_s \\
\frac{d v_2}{d t} &= -b v_1 - d v_2 + b f_s,
\end{aligned}
\tag{4.7}
$$

where a, b, and c are nonnegative parameters, while d includes the pressure-dependent resistance, $k_2(p)$, used to discriminate between pressure stimuli both within and outside the CA range. Initial values for a, b, and c were chosen to ensure that the eigenvalues of the system are negative, thereby ensuring adaptation to baseline flow. Finally, the dynamic (transient) autoregulation component of the blood flow velocity within the MCA is given by

$$
V_{dyn} = M(f_s - v_1),
\tag{4.8}
$$

where $M \approx 1$, representing the amplification. It was noted that $d(p)$ was modeled to distinguish between pressures within and outside the CA range.

Figure 4.3 shows a normalized pressure-flow data sets from rats [Har79; DP90] and cats [Mac76; Mac79]; and a CA curve (solid line), which was modeled using a cubic polynomial of the form

$$
f_{aut}(p) = (2.03 \times 10^{-6})p^3 - (6.02 \times 10^{-4})p^2 + (5.94 \times 10^{-2})p - 1.95.
\tag{4.9}
$$

It is known that the CA range is modulated in disease, e.g. hypertension [Ser01; Try13]. By
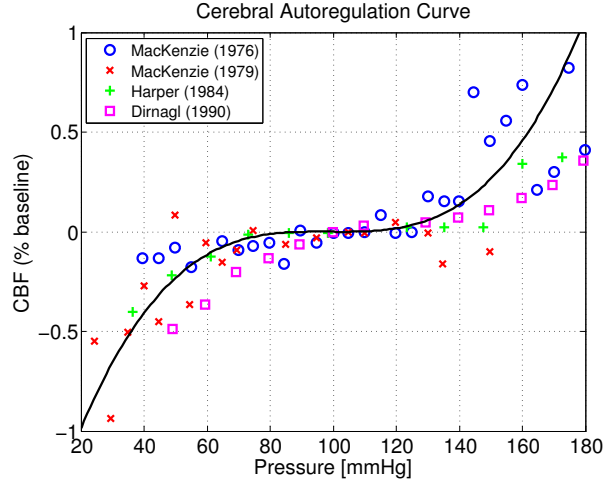
Figure 4.3 CBF-Pressure Curve. Empirical fit of f_{aut} against normalized experimental CBF and ABP data from rats [Har79; DP90] and cats [Mac76; Mac79]. These data suggests that CA range is defined for ABP between approximately 50 and 150 mmHg.

incorporating the steady-state expression for v_1 into Equation (4.8), we obtain

$$d(p) = \frac{b\,c\,f_{aut}}{M\,c\,f_s - (a+c)f_{aut}}, \tag{4.10}$$

ensuring that at the steady-state $V_{dyn} = f_{aut}$. Moreover, it should be noted that within the autoregulatory range $f_{aut} \approx 0$ and as a result $d \approx 0$. The CA curve is determined *a priori*, and therefore no parameters are added to the final model. Using the first steady portion of the subject-specific data set (before standing) and denoted by V_{mca}^d, we compute the baseline value of the CBFV as

$$V_{bas} = \frac{1}{T} \int_0^T V_{mca}^d \, dt, \tag{4.11}$$

where $T = 50$ is the length of the considered interval (in seconds). The values of V_{bas} for the young and elderly subjects have been estimated to be 57.4 and 37.7 cm/s, respectively.

By combining the dynamic V_{dyn} and the baseline V_{bas}, the CBFV in the middle cerebral artery is predicted using Equation (4.3). In summary, the proposed model uses ABP as an input f_s to predict CBFV during postural changes from sitting to standing.

4.2.4 Steady-State and Initial Conditions

The model is formulated as a system of two algebraic and ordinary differential equations in v_1 and v_2. To solve this system, appropriate initial conditions must be determined by, e.g. analyzing steady-state behavior within the model. We assume a constant input stimulus $\bar{f}_s = \bar{p}$, where $\bar{p}$ is the mean pressure over the "steady" portion of the data (e.g., during sitting). Thus, the steady-state of Equation (4.7) is given by

$$v_1^* = \frac{\bar{f}_s(bc + ad)}{bc + (a+c)d}, \qquad v_2^* = \frac{bc\bar{f}_s}{bc + (a+c)d}, \tag{4.12}$$

where d is evaluated at $p = \bar{p}$. From this we get $V_{mca} = V_{bas} + M(\bar{f}_s - v_1^*)$. It should be noted that additional forcing is incorporated in d representing the pressure-dependent spring. However, at rest (before postural change), perturbations in pressure are assumed to be within the CA range. Given that the CA curve was normalized around zero during rest, the input stimulus is $f_{aut} = 0$, which implies that $v_1^* = v_2^* = \bar{f}_s$. One consequence of this assumption is that for simulations examining dynamics outside the CA range f_s will no longer be constant.

4.2.5 Time Constants

Time-constants associated with the model Equation (4.7) were computed to further analyze dynamics around the nominal values of the parameters a, b, and c. Since the eigenvalues λ_1, λ_2 of the Jacobian associated with system (4.7), for a constant stimulus $\bar{f}_s$, are given by

$$\lambda_{1,2} = \frac{1}{2}\left(-a-b-c-d \pm \sqrt{(a+b+c+d)^2 - 4(bc+(a+c)d)}\right), \qquad (4.13)$$

where d is evaluated at $p = \bar{p}$, the time-constants of system of Equation (4.7) are $\tau_{1,2} = 1/\lambda_{1,2}$. Recall that $d(p)$ is not a parameter but a pressure dependent function. We assume that CBFV returns to its baseline value after approximately 20 s, in agreement with the sit-to-stand data analyzed in this study (see Figure 4.1). To facilitate this adaptation, we impose the condition for the steady-state (4.12) to be locally stable, i.e. we require that the eigenvalues (4.13) be negative. This condition is used as a criterion for choosing the initial values (before optimization) for the parameters a, b, and c. For this study it is assumed that $a = 0.25$, $b = 0.1$, and $c = 0.9$. Moreover, assuming that CA operates on more than one time-scale, we checked that optimized parameters generate two distinct time constants, $|\tau_1| \gg |\tau_2|$, which reflect the fast and slow components of the CA dynamics.

4.2.6 Structural Identifiability

As a preliminary step for studying the model's ability to fit measured data, we consider the structural identifiability problem. It addresses the question of whether it is possible to uniquely infer the model parameters given perfect and noise-free data. If possible, structural identifiability should be considered be- fore the practical one. Recall that the practical

identifiability establishes if the model parameters can be determined uniquely given a specific (noisy) dataset. Thus, structural identifiability is a necessary condition for practical identifiability. If a model is unidentifiable, the parameters can take an infinite number of values and still produce the same response [MS14].

We first consider the structural identifiability problem for the CA model given in Equations (4.3, 4.7-4.11), assuming that ABP is within the autoregulatory range, i.e. $f_{aut} = 0$ and consequently $d = 0$, see Equation (4.10). Note that under this assumption, the system (4.3, 4.7-4.11) reduces to two linear differential equations. As discussed in [Mah14], the structural identifiability of the model given by Equation (4.4) can be established by computing the input/output equation. To check the structural identifiability of the model (4.3, 4.7-4.11), we compute the input/output equation, that is, the equation relating p with V_{mca}. First, we differentiate Equation (4.3), and replace $d v_1/d t$ with the expression in Equation (4.7). Next v_1 is extracted from Equation (4.3) and substituted into the current expression in Equation (4.14). Finally, differentiating the resulting expression, replacing $d v_2/d t$ with the equivalent expression in (4.7), and collecting similar terms yields the following input/output equation

$$M \frac{d^2 p}{d t^2} + M c \frac{d p}{d t} = \frac{d^2 V_{mca}}{d t^2} + (a + b + c) \frac{d V_{mca}}{d t} - b c (V_{mca} + V_{bas}). \qquad (4.14)$$

The structural identifiability is determined by whether the corresponding coefficient map

$$\Phi(a, b, c, M) = [M, M c, a + b + c, b c] \qquad (4.15)$$

is one-to-one. It is straightforward to see that equation $\Phi(a, b, c, M) = \Phi(a^*, b^*, c^*, M^*)$ has a unique solution, and thus the model is structurally identifiable in the variables a, b, c,
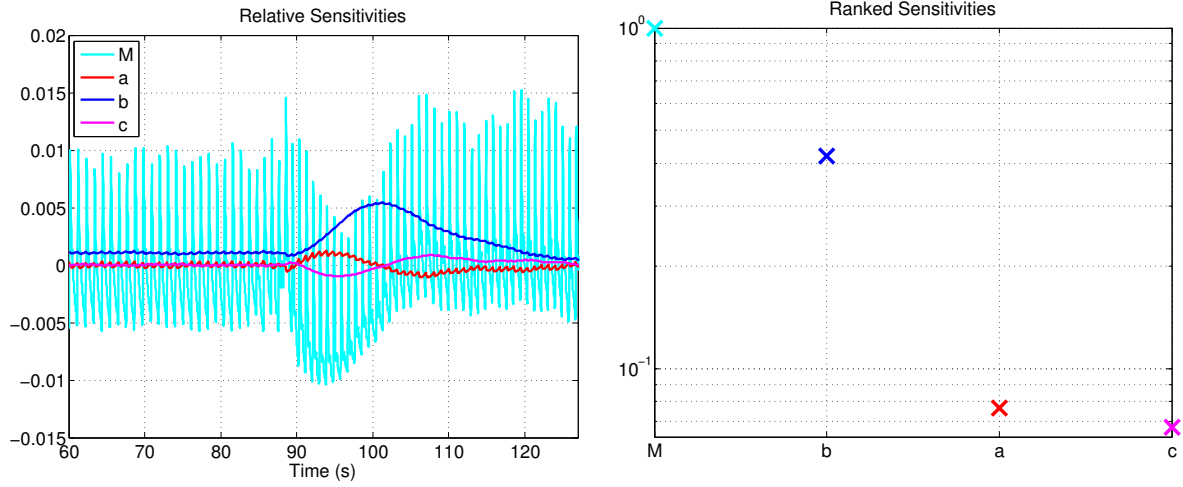
Figure 4.4 Sensitivity analysis. This figure shows the relative (time-varying) [left panel] and ranked [right panel] sensitivities of the model parameters with respect to the model output, CBFV.

and M.

The above analysis assumed that $f_{aut} = 0$, but this is not the case in general. However, if f_{aut} is approximated by a piecewise linear functions, the model can be analyzed in its entirety. For example, if we assume that $f_{aut} = kp$, for some suitable value of k, it can be shown that the model given by Equations (4.3, 4.7-4.11) is structurally identifiable. Unfortunately, it is rather tedious to check the property for the full nonlinear model (4.3, 4.7-4.11), i.e. when f_{aut} is not necessarily assumed to be identically zero but given by Equation (4.9). Thus, to analyze the ability of the general model to fit the data, the sensitivity and practical identifiability problem is considered in the following section.

4.2.7 Sensitivity and Practical Identifiability

Practical identifiability can be determined by considering the sensitivity matrix. To define sensitivities, we assume that the model can be written as

$$\frac{dv}{dt} = f(t, v; \theta)$$
$$h(t; \theta) = g(t, v; \theta),$$

where t denotes time, v represents the state vector $[v_1, v_2]$, $\theta = [a, b, c, M]$ is the parameter vector, $h(t; \theta) = V_{mca}$ is the model output, and g is an algebraic function. The model output V_{mca} defined in Equation (4.3) is computed as a function of the time t, the states v, and the parameter vector θ. Each column of the sensitivity matrix,

$$S = \frac{\partial V_{mca}}{\partial \theta} \tag{4.16}$$

is a time-varying vector that measures how sensitive the model output is to a given parameter at time t (for more details see [OO13]). Given that model parameters do not have the same units, sensitivities cannot easily be compared across the parameter space. To remedy this problem, the sensitivity matrix is often scaled relative to the parameter and the time-varying data. The relative sensitivity matrix is defined by

$$\tilde{S} = \frac{\partial V_{mca}}{\partial \theta} \frac{\theta}{V_{mca}}. \tag{4.17}$$

As noted above, the sensitivities are functions of time for each parameter. For the purpose of parameter identification, it is useful to be able to rank the parameters according to their sensitivity. Insensitive parameters are typically not identifiable. Several measures can be used to obtain ranked sensitivities, but in this study, they are predicted by imposing a two-norm on each column of the sensitivity matrix

$$\bar{S}_i = ||S_i||_2.$$ (4.18)

Plots of the relative (time-varying) and ranked sensitivities (scaled such that the most sensitive parameter has sensitivity equal to one) for the model parameters are shown in Figure 5.3. Note that M is the most sensitive model parameter, while a and c are the least sensitive. For model outputs predicted numerically, parameters for which the ranked sensitivity $S_{\theta i} < \sqrt{\xi}$, where ξ is the tolerance of the ODE solver, are insensitive. For this study, the ODEs were solved numerically using Matlab's ODE solver "ode15s" with absolute and relative error set at 1×10^{-8}. Thus, according to the definition above, all parameters are "sensitive".

A correlation analysis was performed to explore possible pairwise correlations among the sensitive model parameters [Mia11]. The correlation matrix c can be computed from the covariance matrix $C = (S^T S)^{-1}$, as

$$c_{i,j} = \frac{C_{i,j}}{\sqrt{C_{i,i} C_{j,j}}}.$$ (4.19)

The matrix c is symmetric with $|c_{i,j}| \leq 1$ and all $|c_{i,i}| = 1$. Here, we denote the parameter pairs for which $|c_{i,j}| > 0.95$ as correlated. By this definition, all the model parameters are

Table 4.1 Parameter Estimation. Estimated model parameter values for the healthy young (Y) and elderly (E) subjects.

Parameter	Equation	Description	Value (Y)	Value (E)
a	(5.5)	Voigt-body parameter	0.466	2.50
b	(5.5)	Voigt-body parameter	0.0100	0.280
c	(5.5)	Voigt-body parameter	0.290	2.71
M	(5.8)	Mathematical amplifier	1.20	1.00

practically identifiable.

4.2.8   Parameter Estimation

The model was fit to data minimizing the least squares error

$$J = \frac{1}{N} \sum_{i=1}^{N} \left(\frac{\bar{V}_{mca}^{d}(t_i) - V_{mca}(t_i, \theta)}{V_{mca}^{d}(t_i)} \right)^2 , \tag{4.20}$$

where $\bar{V}_{mca}^{d}$ denotes the filtered CBFV data, and V_{mca} is the model output. For each dataset, the parameters were estimated (see Table 4.1) using the Levenberg-Marquardt method [Kel99] with nominal values $a = 0.25$, $b = 0.1$, $c = 0.9$, and $M = 1$.

4.3   Results

4.3.1   Qualitative Results

The qualitative responses of the model, given by Equations (4.3, 4.7-4.11), to pressure step-stimuli within and outside the CA range are presented in Figure 4.5. Input pressures outside of the CA range are denoted by an "o". The upper and the lower panels of the figure
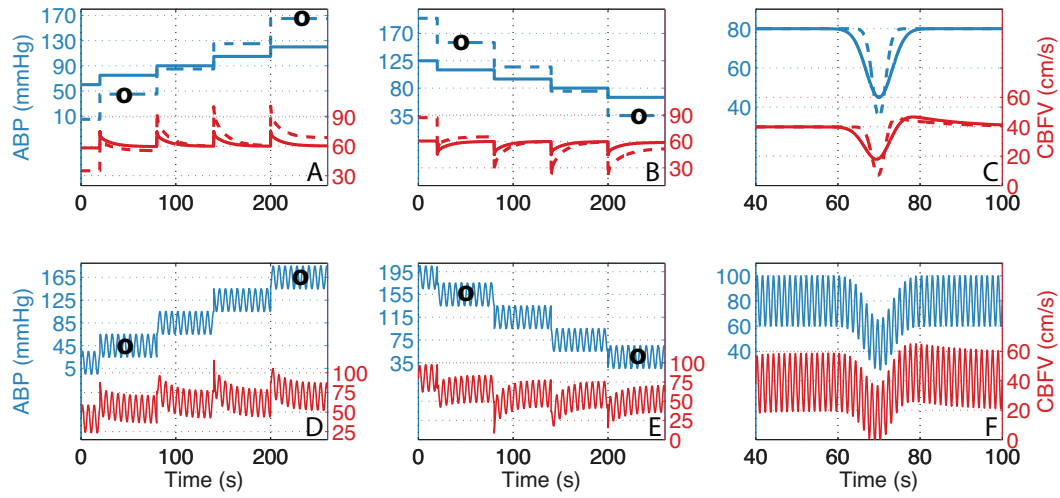
Figure 4.5 Qualitative responses. This figure presents four qualitative responses computed using the ABP/CBFV model. Simulations were done by varying the input pressure (ABP) assuming: a step increases (A), a step decreases (B), ABP drop followed by recovery (C), oscillating step increases (D), oscillating step decreases (E), and an oscillating ABP drop followed by recovery (F). Steps outside of the CA range are denoted by "**o**".

show the filtered and the pulsatile response, respectively. Figures 4.5A and 4.5D show that a step-increase in the input pressure p within the autoregulatory range (solid line) results in an initial overshoot followed by adaptation to the same baseline value. On the other hand, a step-increase in ABP outside the CA range (dotted line) results in V_{mca} settling to a new, higher steady-state value. This is a consequence of incorporating the CA curve into the model. Similarly, the qualitative response of V_{mca} to a pressure step-decrease results in V_{mca} settling at lower CBFV value. Motivated by the sit-to-stand experiment, Figures 4.5C and 4.5F show the model's response to a "dip" in ABP. Results for this stimulus show that the model is able to predict the overshoot and baseline CBFV values recorded before the sit-to-stand protocol. Given that in vivo blood pressure is always pulsatile, we tested that
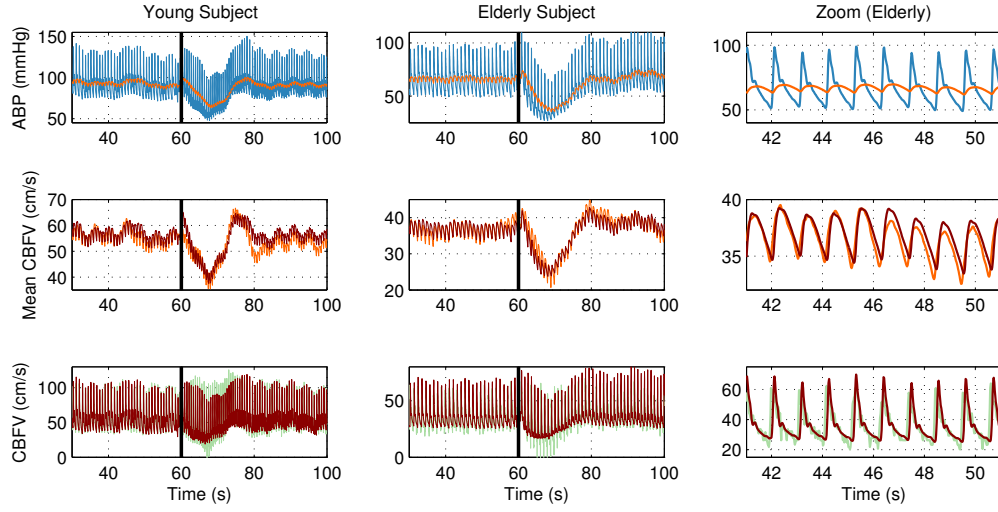
Figure 4.6 Quantitative responses. Estimated mean and pulsatile CBFV model output compared to filtered and pulsatile CBFV data for a young subject and an elderly subject. The vertical black line in each plot denotes the beginning of orthostatic stress.

the model could also reproduce correct behavior when responding to a pulsatile stimulus.

4.3.2 Quantitative Responses

Figure 4.6 shows the model output V_{mca}, given by Equation (4.3), plotted against the pulsatile and filtered ABP/CBFV data from the healthy young and elderly subjects. For both subjects, the fits were generated using the optimal parameter values given in Table 1. The rightmost column shows a zoom of the steady-state segment of the data and the model response. Results obtained using the filtered ABP signal as an input show that the model is able to fit the baseline, dip, overshoot, and adaptation for both the young and elderly subjects. These three features are also captured in the model results computed using the

77

pulsatile ABP data as a stimulus. Though it should be noted that for both the young and the elderly subjects, the model does not fully predict the widening effect portrayed by the data shortly following the transition from sitting to standing. Data for the young subject showed larger overshoot following the ABP stimulus, while the recovery time was larger for the elderly subjects. Both features can be seen in simulation results, in particular for the study using filtered ABP as an input, it should be noted that the stimulus differs between the healthy young and the healthy elderly. The comparison of estimated model parameters shows clear differences. While the parameter M is of the same order of magnitude for both subjects, the Voigt body parameters representing time-scales vary significantly between the two subject types.

4.3.3   Discussion

This study developed a simple nonlinear model using ABP as an input to predict CBFV and analyzed the model's dynamics using both synthetic (pulsatile and nonpulsatile) and experimental data from a heal- thy young and a healthy elderly subject. Results showed that the model is able to capture the CBFV drop, overshoot, and recovery, including both the more pronounced overshoot exhibited by the young subject and the longer time for recovery exhibited by the elderly subject. The model has only four parameters and was motivated by the viscoelastic-like response observed in the data recorded during postural change from sitting to standing. Comparison of estimated model parameters showed that the Voigt body parameters a, b, and c were significantly higher for the elderly subject, while M was similar for both subjects. Given that simulations were performed using one subject in each age group, statistical comparison of values is not feasible. Assuming that

all other model parameters are held at their nominal values, increasing a or b results in a smaller CBFV drop and overshoot, while increasing M produces a more pronounced drop and overshoot. The model response is insensitive to changes in c (see Figure 5.3). Moreover, increasing a results in a longer recovery time. The higher values of a and b in aging could explain observed differences.

One noticeable discrepancy between the fits using pulsatile ABP as an input is that for the young subject, the estimated pulsatile CBFV does not predict the pulse widening observed immediately upon the postural change from sitting to standing. This widening is less pronounced in the elderly subject. This feature was captured in our previous, physiologically-based model [Olu05], though it had more than 60 parameters compared to the 4 parameters in the current approach. It is likely that there may be a feature of CA that this model cannot quantify. For example, if the parameters associated with the change in vessel compliance are not necessarily constant, then they could be determined as a function of strain. More discussion about changes in vessel compliance with age can be found in studies by Carey et al. [Car03] and Yam et al. [Yam05]. Moreover, it should be noted that model simulations were performed using the same parameter set, independent of the nature of the ABP input, i.e. the model was calibrated only to the filtered and not the pulsatile response. We note that estimating parameters using the pulsatile ABP input signal did not provide a better fit.

Although the model output did not fit all aspects of pulsatile CBFV dynamics, the main features of this more complex signal were predicted well. Despite the numerous physiologically-based models that have been developed (see e.g., [UL97; UL98; Urs00; Pay06; Spr12]) to our knowledge this is the first ABP/CBFV model that allows both qualitative and

quantitative prediction of both the average (filtered) and transient (dynamic) responses associated with CA. The main aim of the present study was to model the transient part of ABP/CBFV response. Although the measurements (e.g., the amplitude) of the CBFV depend on the angle of insonation, and that it may vary between individuals, it is likely that it mainly affects the scaling and not the dynamics of ABP/CBFV response.

Aside from model development, extensive model analysis was performed. To our knowledge, no previous CA models have been analyzed whether or not estimated parameters were identifiable. This question is particularly relevant if parameter values are used as physical biomarkers describing the differences both within and between groups of subjects. We showed that the linear model (when $f_{aut} = 0$) is structurally and practically identifiable. For the full nonlinear model (when $f_{aut} \neq 0$) it was not possible to show structural identifiability analytically. If the CA curve is approximated by a piecewise linear function, identifiability can be proven analytically. Regardless, subsequent sensitivity analysis showed that all model parameters were sensitive and practically identifiable allowing estimation of all model parameters. Given that the model has only four parameters, the optimizations were relatively fast. For one dataset it took approximately 10 min using Matlab on a Macbook Pro with a 2.3 GHz Intel Core i5 processor.

While its simplicity makes the model computationally feasible to work with, it may be difficult to infer what specific physiological mechanisms were compromised. Moreover, this type of model is not yet able to predict the cause of disease, similar to many statistical methods [Pan95; Czo96] and efforts aiming at computing various autoregulation indices [Tie95; Pan03a; LA02; Liu03]. One way to improve the current approach could be by incorporating some mechanisms present in physiologically-based models, at the same

time keeping it computationally efficient. Several previous approaches could be used as a point of departure for this effort including the works by Ursino et al. [UL97; Urs00], Arciero et al. [Arc08], or Spronck et al. [Spr12], which quantify in detail the metabolic, myogenic, shear-dependent, and neurogenic responses. The advantage of the latter models is that they can be used to understand how each mechanism impacts the overall dynamics, a feature not provided by our study. The disadvantage is the high number of parameters, which are typically unidentifiable, making the model difficult to validate against experimental data.

4.4   Summary

In conclusion, the CA model developed in this study is able to predict both qualitative and quantitative dynamics associated with ABP/CBFV response during a postural change from sitting to standing. Qualitative features were analyzed by imposing step-changes and a "dip" change in ABP within and outside the CA range. Quantitative responses were analyzed by showing that the model can fit both filtered and pulsatile CBFV dynamics during a postural change from sitting to standing, a feature that to our knowledge has not been tested in previous modeling studies. Parameter estimation was used to show that the model could be adapted to distinguish responses in a healthy young and healthy elderly subject. The model provided very good agreement with the data (for the subjects shown). Finally, we showed that the model exhibits an important nonlinearity related with the CA curve.

CHAPTER

5

DYNAMIC CEREBRAL

AUTOREGULATION IN AGING AND

HYPERTENSION

Similar to Chapter 4, this chapter includes our second manuscript, currently in review. This study was carried out in collaboration with Olufsen, who advised Mader on model development and analysis, and Ottesen and Timmermann who conducted the nonlinear

mixed effects studies.

5.1 Introduction

Cerebral autoregulation (CA) is the combination of local responses that work to maintain adequate cerebral blood flow (CBF) despite changes in pressure. CA is typically studied from two perspectives. Static cerebral autoregulation refers to the net effect that a steady-state change in arterial blood pressure (ABP) has on CBF, generally portrayed using the Lassen curve [Las59]. Dynamic cerebral autoregulation (dCA) describes the transient cerebral blood flow response to alterations in ABP. The latter has been shown to be the more vulnerable component to impairment in certain disease states [Tie95]. Since the elderly are more prone to disease, it is important to study the effects that aging may have on autoregulatory function.

The human cardiovascular system experiences many age-related changes, including decreases in systemic artery compliance [Fle86] and increases in systolic ABP [Kan78]. Additionally, aging leads to widening of cerebral arterial vessels [Kre99] and is responsible for a decrease in both cerebral blood flow velocity (CBFV) and cerebral blood flow volume [Car00; Car03]. Gender differences in the elderly have been studied, concluding that elderly women have better vascular function than elderly men and that women autoregulate better than men [Dee10].

Hypertension is a major risk factor for cerebrovascular diseases [Fuj95]. Increased vascular resistance in hypertension decreases CBF in elderly hypertensives to the level

observed in healthy young subjects [Str73]. This increased resistance is a result of structural changes in the smaller resistance vessel, characterized by narrowed arterioles with thickened walls [CY72]. Moreover, the presence of hypertension reduces the cerebrovascular response to changes in the arterial partial pressure of CO_2 [Mae94].

Current studies cannot detect age-related changes and cannot consistently quantify the effects of aging and hypertension on CA function. Regardless of the method by which CA is assessed, authors have concluded that autoregulation is not compromised in the elderly. Many approaches have been used, including the Mx index [Yam05], the autoregulatory index (ARI) [Car00; Car03], rate of recovery [Sor05], and transfer function analysis [Bee08]. To our knowledge, the only study that has been able to identify age-related effects is that by Vavilala et al. [Vav02], which found that there is a significantly lower CA response in adolescents compared with adults. Investigators also have found that the CA response is preserved in patients with controlled hypertension [Lip00; Fu05]. In addition, one study also found normal CA before and after treatment of hypertension [Zha07]. Novak et al. [Nov04] used the ARI during the Valsalva maneuver and found that there is no difference between healthy and hypertensive middle-aged subjects. They concluded that a smaller phase shift between CBF and ABP signals is an indication that autoregulation is less efficient in hypertensive subjects. Yet, Eames et al. [Eam03] suggested that ARI is not impaired by hypertension in both middle aged and older people. Finally, in a study comparing controlled and uncontrolled hypertensives using transfer function analysis showed that dynamic CA is maintained in both groups [Ser05].

We hypothesize that these studies have failed to capture differences between healthy young, healthy elderly, and hypertensive elderly subjects for three reasons: A) The existing

methods referenced above all assumed a linear relationship between ABP and CBFV [Cla16], a major limitation since CA is widely assumed to be nonlinear [Pan99]; B) All of the previous methods assessed CA using beat-to-beat averaged data; C) Most existing methods lack consistency leading to frequent occurrence of misdetections [Pan03b; Elt14]. To overcome these problems, the Cerebral Autoregulation Research Network (CARNet) argued for the need of a better gold standard [Cla16].

In this study we show that by accounting for pulsatility and nonlinearity, it is possible to devise a measure that can distinguish between three patient groups: healthy young, healthy elderly, and hypertensive elderly. Results are obtained by expanding our previous model [Mad14] and by analyzing the model dynamics within and between the three patient groups. Results were obtained by estimating patient specific model parameters for each subject, which were compared between each of the three groups using a two sample t-test. In addition, nonlinear mixed effects analysis was used to test if all subjects belong to the same population with equal population parameter values, or if the population parameters vary among the three subgroups.

5.2   Materials and Methods

5.2.1   Experimental Methods

De-identified pressure and blood flow data from twenty-eight people were included in this study. The data analyzed were obtained from Dr. Lipsitz at the Hebrew Rehabilitation Center for Aged, Boston, MA. The Institutional Review Board at the Hebrew Rehabilitation Center approved the study and all subjects provided written informed consent according

to the Helsinki II declaration [Lip00]; readers interested in acquiring these data should contact Dr. Lipsitz (email in Acknowledgement section). Two active sit-to-stand procedures were performed on 10 healthy young (age 24±1), 10 healthy elderly (age 72±3), and 10 hypertensive elderly subjects (age 72±2), but data from one young and one elderly subject were not included in our analysis since recordings from either trial were inadequate. This study analyzed ABP and CBFV data from the first sit-to-stand protocol unless the signal was too noisy or included negative or missing measurements. All subjects rested in the sitting position for five minutes and then stood upright for one minute. Transient ABP at the level of the heart and CBFV in the middle cerebral artery (MCA) were measured noninvasively using a photoplethysmographic Finapres monitor (Ohmeda Monitoring Systems, Englewood, CO) and a 2 MHz probe of a portable Doppler system (MultiDop X4, DWL-Transcranial Doppler Systems Inc., Sterling, VA), respectively. ABP was measured using the Finapres in the middle finger of the non-dominant hand, supported by a sling to keep the hand at the level of the right atrium. The latter is needed to eliminate hydrostatic pressure effects. In order to minimize the effects of respiration, subjects were required to breathe at a rate of 15 breaths per minute with the assistance of tape-recorded cues. For the hypertensive subgroup, antihypertensive medications were tapered over 1 to 2 weeks, then withheld for at least 1 week before the experimental protocol was performed. This study used the sit-to-stand protocol because it is well tolerated by elderly subjects and it simulates a physiologic challenge that occurs in daily life capable of threatening cerebral perfusions [Lip00]. A summary of the experimental data is given in Table 5.1.

Table 5.1 Experimental Data. Data are presented as means ± standard deviations. Also provided are the p-values comparing baseline ABP and CBFV in both the sitting and standing phases of experimental protocol for each of the three subgroups. For example, the notation p_{YE} denotes the p-value associated with a t-test comparing the healthy young and elderly subgroups. Here, a p-value of less than 0.05 is considered significant.

	Y	E	H	p_{YE}	p_{EH}	p_{YH}
ABP: Sitting	93 ± 10	85 ± 10	116 ± 11	0.064	< 0.001	< 0.001
ABP: Standing	94 ± 11	85 ± 9	114 ± 10	0.068	< 0.001	0.001
CBFV: Sitting	44 ± 19	36 ± 11	32 ± 11	0.248	0.527	0.106
CBFV: Standing	42 ± 17	34 ± 10	31 ± 4	0.200	0.491	0.082

5.2.2   Data Preprocessing

Instead of using the raw signals, we filter the data to reduce signal noise. Most dCA methods, e.g. [Tie95; Cla16], use beat-to-beat averages of ABP and CBFV for clinical assessment. Here we consider the effects that preprocessing strategies can have on dCA, including beat-to-beat averages and various levels (β) of a previously used [Mad14; Olu06] smoothing technique.

The methods produce the filtered ABP and CBFV signals $\bar{x} \in \{P_\beta, V_\beta\}$ as weighted averages, according to the expression

$$\bar{x} = \beta \int_{-\infty}^{t} x(s) e^{-\beta(t-s)} ds, \tag{5.1}$$

where $x \in \{P, V\}$ is the pulsatile data. Differentiation of (5.1) yields

$$\frac{d\bar{x}}{dt} = \beta(x - \bar{x}). \tag{5.2}$$
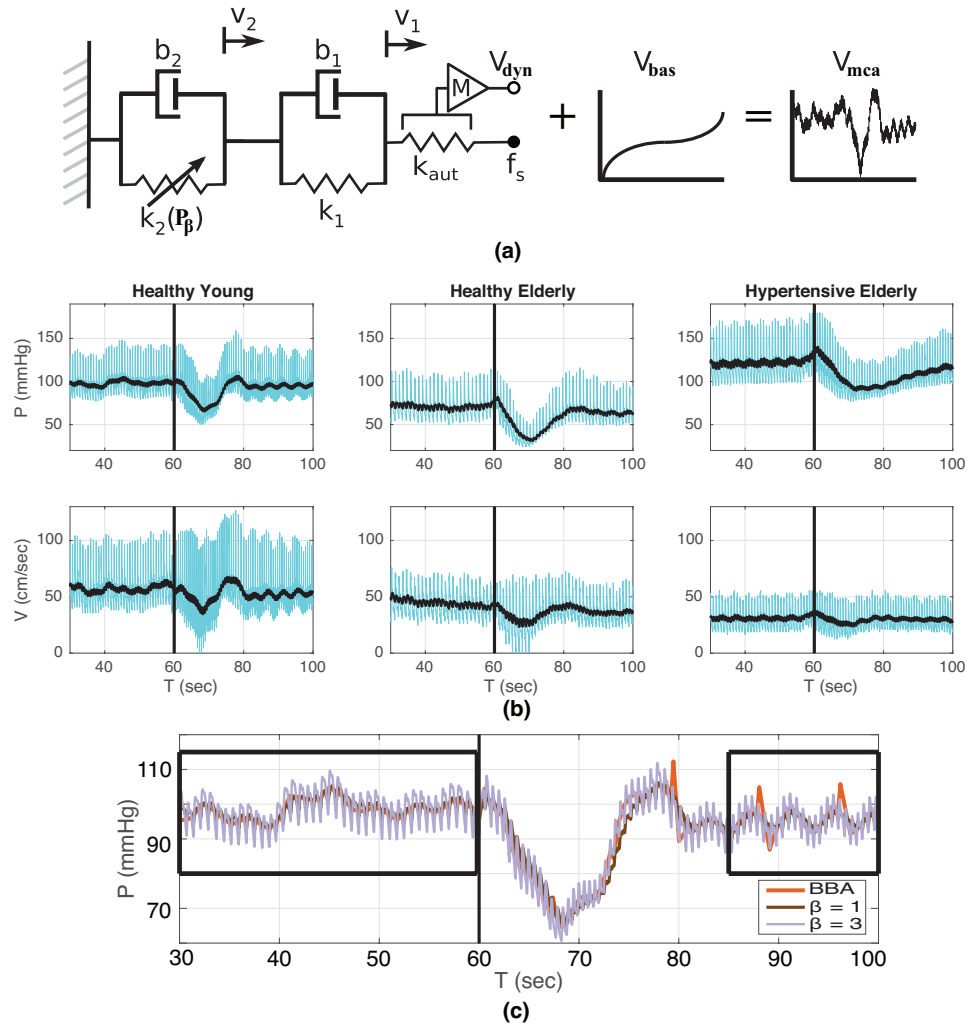
Figure 5.1 Experimental Setup and Data Overview. (a) Mechanical analog used for predicting V_{dyn}. The schematic diagram shows the mechanical analog model used for predicting dynamic autoregulation. The model includes two viscoelastic Voigt body elements combined with a spring accounting for the elastic response. (b) Measured pulsatile (blue) and filtered (black) signals for a representative experimental subject from each of the three subgroups. The filtered ABP and CBFV signals are computed as moving averages from the beat-to-beat pulsatile data as described in Equations (5.1)-(5.2). (c) Zoom view of changing pulsatility in the input ABP for the healthy young dataset. Note, a large value of β allows for more pulsatility in the filtered data.

The parameter β determines the history weight (1/sec). Figure 5.1(b) shows the pulsatile and filtered ABP and CBFV signals for a representative dataset including a healthy young, healthy elderly, and hypertensive elderly subject. In this figure, the black vertical line indicates the onset of the postural change from sitting to standing. Smaller values of β lead to reduced pulsatility and a delayed CBFV response in the preprocessed data; whereas, greater values of β include more pulsatility in the signal, see Figure 5.1(c). Most results in this study are generated using $\beta = 1$.

5.2.3 Mathematical Modeling

The model used to predict CBFV (V_m) consists of two parts: the baseline (V_{bas}) and dynamic (V_{dyn}) components of CBFV, related as

$$V_m = V_{dyn} + V_{bas}. \tag{5.3}$$

The baseline CBFV (V_{bas}) is predicted using a patient-specific sigmoid function relating the mean CBFV in the MCA while sitting (V_β^{pre}) and the terminal mean velocity during standing (V_β^{post}), defined as

$$V_{bas} = V_\beta^{pre} - \left(V_\beta^{pre} - V_\beta^{post}\right)\left(\frac{t^n}{t^n + k^n}\right). \tag{5.4}$$

The pre and post mean MCA velocity are predicted as

$$V_\beta^i = \frac{1}{T} \int_{t_s^i}^{t_e^i} V_\beta(t)dt,$$

where $V^i \in \{V^{pre}, V^{post}\}$, t_s^i and t_e^i denote the start and end time, marked by black boxes on Figure 5.1(c). The steepness of sigmoid is given by n, and k denotes the time at which the sigmoid has half its max value. Note this model assumes that $V_\beta^{pre} < V_\beta^{post}$.

Separating V_{bas} in two parts is an extension of our previous study [Mad14], which assumed that baseline velocity was the same before and after the sit-to-stand procedure. While this was reasonable for the three representative subjects analyzed earlier it does not hold in general.

Similar to our previous study [Mad14], the dynamic component of cerebral autoregulation, i.e. dCA, is modeled using a mechanical system comprised of two viscoelastic Voigt body elements combined in series with a spring, accounting for the elastic portion of the response. Following the diagram in Figure 5.1(a), expressions for the strain across each dashpot are given by

$$
\begin{aligned}
\frac{d v_1}{d t} &= -(a+b+c)v_1 + (c-d)v_2 + (a+b)f_s \\
\frac{d v_2}{d t} &= -b v_1 - d v_2 + b f_s,
\end{aligned}
\tag{5.5}
$$

where a, b, c, and d are nonnegative parameters that include the viscoelastic elements: $a = \frac{k_{aut}}{b_1}$, $b = \frac{k_{aut}}{b_2}$, $c = \frac{k_1}{b_1}$, and $d = \frac{k_2(P_\beta)}{b_2}$. Parameters a and b describe the time course of the autoregulatory recovery from the imposed pressure change. Parameters c and d relate the stresses on each of the Voigt bodies. To account for the nonlinearity of CA [Pan99], d is assumed to be pressure-dependent distinguishing between pressure stimuli within and outside the CA range. On average, when the ABP is below 50 mmHg and above 150 mmHg [Las59], autoregulation is abolished and CBF passively follows the ABP changes. The normalized CA curve shown in Figure 5.2(a) was modeled using a cubic function of the
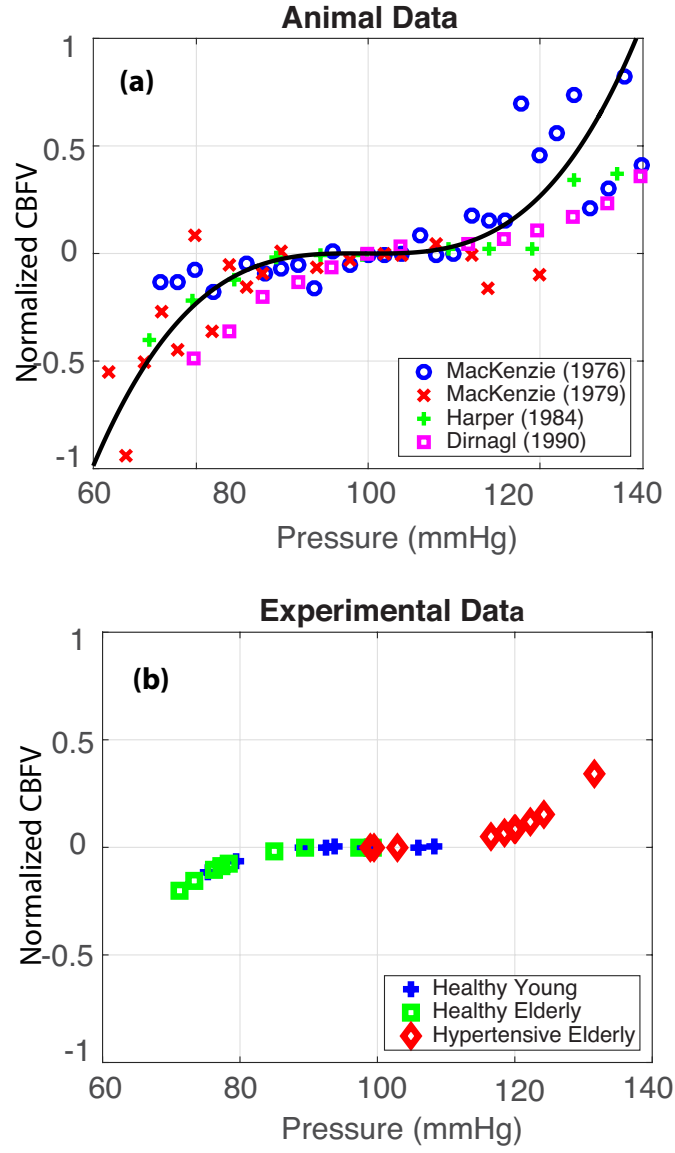
Figure 5.2 Static Autoregulation Curve (sCA). (a) Fit of f_{aut} against normalized experimental CBF and ABP animal data [Mac76; Mac79; Har79; DP90], and (b) the f_{aut}-ABP prediction for data analyzed in this study.

form

$$f_{aut}(P_\beta) = (2.03 \times 10^{-6})P_\beta^3 - (6.02 \times 10^{-4})P_\beta^2 + (5.94 \times 10^{-2})P_\beta - 1.95. \tag{5.6}$$

To ensure that d exhibits threshold and saturation, we let

$$d(P_\beta) = \frac{bc f_{aut}(P_\beta)}{Mc f_s - (a+c)f_{aut}(P_\beta)}. \tag{5.7}$$

The CA curve f_{aut} is determined a priori before the model is fit to patient data. Note that within the autoregulatory range $f_{aut} = 0$ and consequently $d = 0$. Finally, V_{dyn} is given by

$$V_{dyn} = M(f_s - v_1), \tag{5.8}$$

where M is a constant close to 1, representing an amplifier, adjusting the CBFV drop and overshoot observed in response to the sit-to-stand challenge.

In summary, the model uses the filtered ABP, denoted P_β (used to calculate f_s) to predict filtered CBFV dynamics during a postural change from sitting to standing combining the baseline V_{bas} and dynamic V_{dyn} components of the CBFV. For each dataset model parameters $\theta = [a, b, c, M, n, k]$ were estimated to predict patient specific CBFV.

5.2.4 Model Analysis

5.2.4.1 Sensitivity Analysis

Sensitivity analysis and correlation analysis [OO13; Mia11] were conducted to determine practical identifiability of model parameters. We assume that the model can be written as

$$\frac{dv}{dt} = f(t, v; \theta)$$
$$h(t, v; \theta) = g(t, v; \theta),$$

where t denotes time, $v = [v_1, v_2]$ denotes the state vector, $\theta = [a, b, c, M, n, k]$ is the parameter vector, $h(t; \theta)$ is the model output (V_m) given by g (the algebraic expression in Equation (5.8)). Given this formulation, the sensitivity matrix S can be written as

$$S = \frac{\partial h}{\partial \theta} = \frac{\partial V_m}{\partial \theta}, \tag{5.9}$$

for this specific model where the model output is $h = V_m$. In the sensitivity matrix, each column is a time-varying vector measuring how sensitive the model output is to a parameter at a given time t [OO13]. To obtain sensitivities that are all the same unit, it is scaled relative to the parameter and the transient data. The relative sensitivity matrix is given by

$$\tilde{S} = \frac{\partial V_m}{\partial \theta} \frac{\theta}{V_m}. \tag{5.10}$$

Since insensitive parameters are difficult to identify, the parameters are ranked according to their sensitivity. Ranked sensitivities are determined by imposing a two-norm on each column of the sensitivity matrix

$$\bar{S}_i = \left\| \tilde{S}_i \right\|_2. \tag{5.11}$$

5.2.4.2 Subset Selection

Subset selection was performed to explore possible pairwise correlations among the sensitive model parameters [OO13; Mia11]. The correlation matrix c can be computed from the covariance matrix $C = (S^T S)^{-1}$ (assuming it is not singular), as

$$c_{i,j} = \frac{C_{i,j}}{\sqrt{C_{i,i} C_{j,j}}}. \tag{5.12}$$

The matrix c is symmetric and upper triangular with $\left|c_{i,j}\right| \leq 1$ and all $\left|c_{i,i}\right| = 1$. For this study, we denote parameter pairs for which $\left|c_{i,j}\right| > 0.95$ as correlated.

5.2.4.3 Parameter Estimation

For each subject, using filtered ABF as an input, the model was fit to filtered CBFV data using two distinct methods: nonlinear least squares and nonlinear mixed effects (NLME) analysis. The four most sensitive model parameters were estimated assuming nominal values $a = 0.25$, $b = 0.1$, $M = 1$, and $k = 65$.

5.2.4.4 Nonlinear least squares optimization

Nonlinear least squares optimization estimates parameters minimizing the least squares cost $J = R^T R$ between the model output V_m and data V_β, where R is the residual error given by

$$R = \frac{\bar{V}_\beta(t_i) - V_m(t_i, \theta)}{\bar{V}_\beta} \tag{5.13}$$

evaluated at times t_i where the data are measured. Least squares optimization was performed using the Levenberg-Marquardt method [Kel99].

5.2.4.5 Nonlinear Mixed Effects

NLME modeling embeds deterministic models of individuals, which are given by solutions to the differential equations, into a statistical framework whereby inference for repeated measurements from a population, extraction of knowledge, and assumptions on variation in outcomes within and across individuals become formalized [Bon11]. Note, the average of the least squares estimates do not account for variability across individuals.

Statistical inferences are introduced focusing on the model parameters that underlie the individual profiles and on how these vary across the population. In this study, NLME analysis is used to test if the model parameters vary significantly between the three pre-defined subgroups: healthy young, healthy elderly, and hypertensive elderly. Two models are compared; a base model where all subjects are assumed to belong to the same population with equal population parameter values, and a full model where the population parameters values are allowed to vary among the three subgroups.

The statistical test is based on the change in the objective function value between the base model and the full model. Since the two models are nested, the difference is ξ^2-distributed with the difference in number of parameters as degrees of freedom.

A priori, all model parameters to be estimated are assumed to be log-normally distributed. A proportional residual error model is chosen. The stability of the parameter estimates is evaluated using the non-parametric bootstrap approach. For both the base and the full model, 200 new data sets each with twenty eight subjects is generated by repeated random sampling with replacement from the original data set and the model parameters and associated relative standard errors of the parameter estimates will be estimated.

The NLME analysis of the data was conducted using the software program NONMEM (version 7.2, ICON) with the GNU Fortran 95 compiler [Bea11]. The ADVAN13 subroutine was used for integration of systems of nonlinear differential equations and the first order conditional estimation method with interaction (FOCEI) was used for parameter estimation. Data processing and diagnostic plots were performed using S+ (version 8.1, TIBCO Software Inc.).

5.2.4.6 Statistics

Comparison of estimations within and between the three known groups is done by analyzing p-values computed using a two sample t-test with $\alpha = 0.05$ confidence level. Let μ_Y, μ_E, and μ_H represent the means of a parameter estimate from the healthy young, healthy elderly, and hypertensive elderly subgroups. Location testing tests the null hypothesis that the means from two independent samples are equal.

Table 5.2 Parameter Estimates. Least squares estimates of model parameters across the healthy young (Y), healthy elderly (E), and hypertensive elderly (H) subgroups. Nonlinear mixed effects estimates using full model with 12 fixed effect parameters (4 model parameters by 3 subgroups) distinguishing the three subgroups. Nonlinear mixed effects estimates using base model with four fixed effect parameters providing population (Pop) estimates. Model residual errors of the full and base models are 5.1 and 5.4, respectively. Inter-individual variability (IIV) expressed as coefficient of variation (CV%).

Parameter	Least Squares			NLME Full Model				NLME Base Model	
	Y	E	H	Y	E	H	IIV	Pop	IIV
a	0.25	0.29	0.27	0.337	2.25	0.0694	165	0.242	128
b	0.30	0.45	0.61	0.313	0.647	0.773	61	0.429	59
M	0.78	0.68	0.49	0.888	1.28	0.566	28	0.807	37
k	72	79	80	69.9	83.7	79.5	12	70.5	15

5.3 Results

The hypertensive subjects have a significantly higher ABP ($p < 0.001$) in both the sitting and standing stages of the experimental protocol when compared with the young and elderly subgroups (see Table 5.1). No significant baseline CBFV differences amongst the
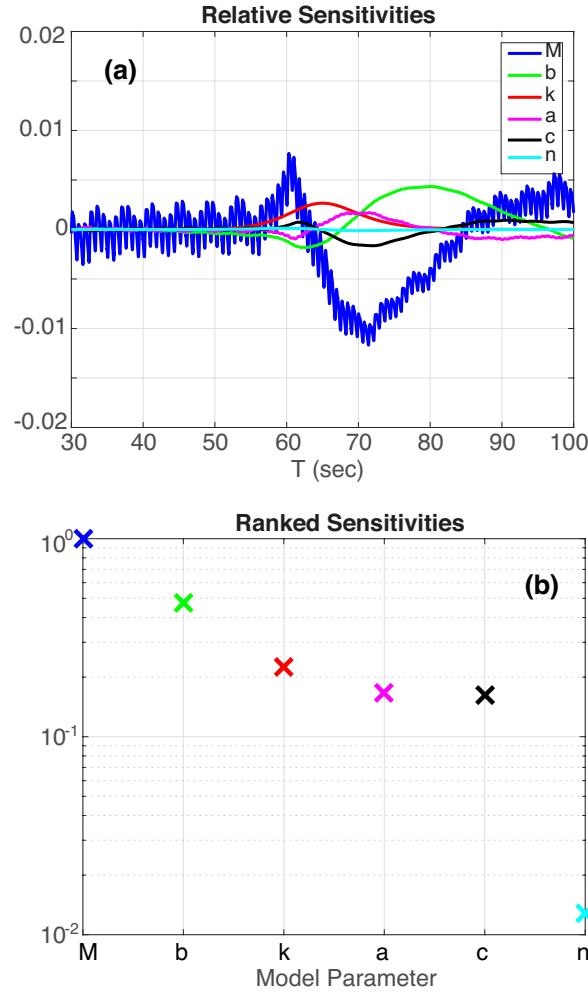
Figure 5.3 Sensitivity analysis. Relative (time-varying (a)) and ranked (b) sensitivities of the model parameters with respect to the model output.

three subgroups were observed.

To compare the steady-state ABP/CBFV relationships of the three subgroups along the static CA curve, see Figure 5.2(b), a t-test was conducted at the $\alpha = 0.05$ significance level. The p-values of $p_{YE} = 0.043$, $p_{EH} = 0.001$, $p_{HY} = 0.017$ were obtained, indicating that the differences between the resting ABP/CBFV amongst all three subgroups are of statistical
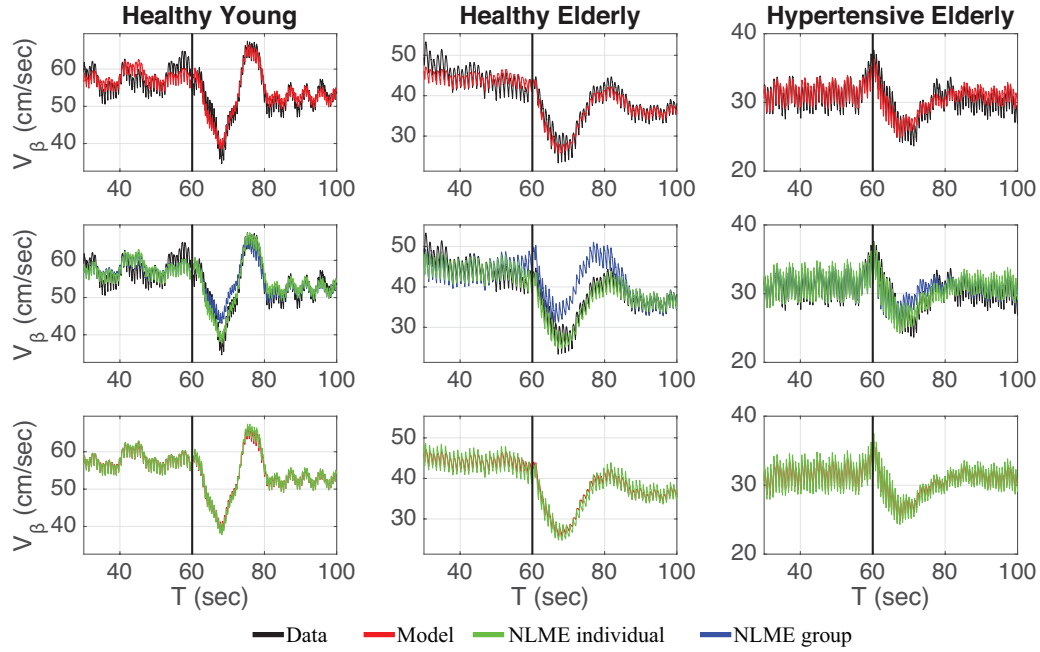
Figure 5.4 Quantitative Results. Model output using least squares optimization against mean CBFV data for representative subjects (top row). Nonlinear mixed effects estimates for individual and group against mean CBFV data for representative subjects (middle row). The model output using least squares optimization against parameter estimates using nonlinear mixed effects for representative subjects (bottom row).

Table 5.3 Pulsatility. p-values comparing subgroups at various β values, where "BTB" denotes beat-to-beat input. The p-values of statistical significance are indicated with $*$.

β	**a**			**b**			**M**			**k**		
	p_{YE}	p_{EH}	p_{HY}	p_{YE}	p_{EH}	p_{HY}	p_{YE}	p_{EH}	p_{HY}	p_{YE}	p_{EH}	p_{HY}
BTB	0.536	0.903	0.279	0.312	0.380	0.059	0.353	0.488	0.041*	0.277	0.716	0.049*
0.5	0.490	0.731	0.615	0.244	0.429	0.020*	0.369	0.069	0.003*	0.295	0.907	0.066
1.0	0.023*	0.239	0.331	0.193	0.217	0.006*	0.408	0.038*	0.005*	0.290	0.871	0.065
1.5	0.017*	0.152	0.391	0.153	0.193	0.001*	0.931	0.016*	0.003*	0.305	0.797	0.061
2.0	0.002*	0.121	0.369	0.098	0.211	0.001*	0.821	0.029*	0.003*	0.349	0.999	0.201
3.0	0.001*	0.211	0.234	0.076	0.211	0.001*	0.687	0.027*	0.003*	0.265	0.612	0.025*

significance.

Plots of the relative and ranked sensitivities for the model parameters are shown in Figure 5.3. Given an integration tolerance of $TOL = 10^{-6}$, parameters with a sensitivity smaller than $10\sqrt{TOL}$ are insensitive [Pop09]. According to this measure n is insensitive, so it was kept fixed at $n = 30$. For most subjects the second least sensitive parameter c was pairwise correlated with a and was therefore also kept fixed ($c = 2.5$).

The estimated parameter values within each of the three subgroups using nonlinear least squares optimization are provided in Table 5.2. The model output computed using optimized parameters at the $\beta = 1$ level for representative healthy young, healthy elderly, and hypertensive elderly subjects are shown in the top row in Figure 5.4. The p-values comparing the estimated parameter values across the three subgroups are listed in Table 5.3 (see $\beta = 1$ line). When comparing the healthy young and the hypertensive elderly subjects, parameters b and M vary significantly. Parameter M is also of statistical significance distinguishing between the healthy and hypertensive elderly subjects.

Furthermore, Table 5.2 lists the estimated population values for the four parameters along with the inter-individual variability and residual error obtained using NLME analysis. In the full model, each of the four population parameters are allowed to vary across the three subgroups, leading to a model with 12 parameters. The middle row in Figure 5.4 shows individual and population predictions against the mean CBFV data for the representative subjects. Allowing the sub-groups to have separate population parameters for each of the four model parameters resulted in a statistically significant improvement of the model. The last row in Figure 5.4 compares the least squares and NLME individual predictions.

Finally, Table 5.3 shows the p-values comparing the subgroups for different values of β

(shown on Figure 5.1(c)). Consistent significant differences between the three subgroups are detected when more pulsatility is introduced in the ABP input (for $\beta \geq 1$). This is done by increasing the value of β when determining P_β.

5.4   Discussion

Stable and optimal cerebral blood flow is imperative for normal brain function. Several factors effect brain function, including age, hypertension, diabetes, and a range of other disease states. All of these alter the brain structure and overall cerebral function, rapidly increasing the risk of cognitive and physical impairment.

   CA is typically assessed [Tie95; Zha98] from model based analysis of CBFV and arterial BP. As discussed earlier, existing tests are not able to detect changes due to healthy aging. This study presents a new model that is able to detect differences between three age groups including healthy young and elderly, as well as hypertensive elderly.

   Similar to observation by Yam et al. [Yam05], the group of young subjects (see Table 5.1) did not display a significantly increased CBFV compared to the elderly and hypertensive subgroups, as suggested by previous studies [Car00; Vav02; Ros03; Sor05]. This may be due to a relatively small sample size, uncertainties in data collection, or it could be attributed to the specific test analyzed. Yet as expected, the ABP was significantly higher in hypertensive subjects than in the healthy subjects, but could not be distinguished between the healthy young and elderly. However, by mapping mean resting BP (averaged over the sitting period) measured during sitting onto the static CA curve, we were able to distinguish all three patient groups (see Figure 5.2). The differentiation between the three groups were also observed from analysis of dynamic model components as shown in Table 5.3 (see $\beta = 1$).

Finally, we showed that it is essential to include some pulsatility to distinguish the three subgroups. In particular note that group differences cannot be detected for $\beta < 1$ as shown in Table 5.3. This is particularly evident for parameter a, which cannot be distinguished between the healthy young and elderly for $\beta < 1$. In summary, model analysis presented here compared dynamic data from 28 subjects using a model extended from previous studies [Mad14; Tie95]. Moving forward, the next step will be to interpret changes to determine what model parameters best reflect CA pathophysiology.

In addition to extracting differences among groups, the model is able to accurately estimate the filtered CBFV for all 28 subjects, see Figure 5.4. This figure shows that accurate model fits can be obtained both using least squares optimization and NLME analysis. Using NLME analysis we observe a high intra-group variability for model parameter a, which indicates variability in the dynamic response.

The estimated parameters provide insight into what quantities are changed with aging and hypertension. The significantly smaller value for parameter M indicates a less significant viscoelastic response after standing, dampening the CBFV drop and overshoot following posture change to standing, a characteristic observed in the elderly hypertensive subgroup when compared to all healthy subjects (both young and elderly). This finding suggests that the dynamic CA response is different in the presence of hypertension and can be characterized by the parameter M. In addition, the parameter a is higher in the healthy elderly compared to the healthy young, while the parameter b is significantly larger in the hypertensive elderly compared to the healthy young subjects. Parameter a is associated with the stress sensed by the autoregulatory spring. A higher value of a indicates a decreased CA response, resulting in a smaller CBFV drop and overshoot. The parameter b increased

101

in aging and hypertension, and is associated with the autoregulatory recovery time (see Figure 5.1(b)). The increase in this parameter suggests that it takes longer for the elderly and hypertensive subjects to autoregulate.

Our findings conflict with earlier studies, which did not determine any CA change with hypertension [Lip00; Eam03; Ser05; Fu05]. Many studies suggest that even though aging leads to vasculature changes, altered CBF, endothelial dysfunction, and reduced innervation density, the dynamic CA response is not compromised in the elderly. Although we cannot say verbatim that CA is impaired in the elderly, analysis of dynamic model parameters suggests that significant differences can be found between the groups. Even though most of the parameter estimates within each group are similar (see Table 5.2), a large inter-individual variability is detected for parameter a when using NLME analysis. To gain more insight on this difference, we considered the effects of pulsatility.

The inclusion or exclusion of pulsatility in the preprocessed ABP data alters the results significantly. Pulsatility can be controlled by varying β in Equations (5.1)-(5.2) (see Figure 5.1(c)). The results in our previous [Mad14] and current study (see Table 5.2) were determined using $\beta = 1$. From Table 5.3, notice the small differences for low values of β. These decreased values of β as well as the input data consisting of one data point per heartbeat are similar to the common clinical methods used for CA assessment that only explore beat-to-beat averages of experimental data. When minimal pulsatility is included ($\beta < 1$), the only differences detected (see Table 5.3) are between the healthy young and hypertensive elderly subgroups. The comparison of these two groups is not intuitive since they differ in age and health. By increasing β, and therefore introducing more pulsatility, the model consistently identifies significant differences in the dCA responses between

the subgroups. The effect of aging can be quantified by comparing the healthy young and elderly subgroups, and a difference in the dynamics is consistently detected through parameter a. The effects of hypertension on CA can be quantified by distinguishing between all healthy subjects and the hypertensive elderly subjects, and a difference exists in parameter M. These conclusions strengthen our findings using $\beta = 1$, and we argue that by ignoring pulsatility in the input data, important information about the dynamics is discarded.

5.5   Summary

In conclusion, this study contributes to the ongoing discussion of the effects of aging and hypertension on cerebral blood flow regulation. Since hypertension has been shown to shift the limits of autoregulation toward higher levels of ABP to protect the brain against hypertension [Pau90], one possible model enhancement could be to shift the static CA curve (f_{aut}). The model is able to accurately estimate CBFV from ABP input in every subject. More importantly, when incorporating some pulsatility in the input, the model is able to differentiate between healthy young, healthy elderly, and hypertensive elderly subjects. While the current formulation of the model is incapable of identifying impaired CA, the ability of the model to distinguish between the three groups suggests that the dCA responses are different and that a lot of information pertaining to dCA is lost when using only beat-to-beat averages for ABP and CBFV. Results of this study contribute to understanding what quantities may be impacted by aging and hypertension, but given high variability in parameter estimates, we have a significant amount of misdetection, likely due to the high inter-individual variability.

CHAPTER

6

MATHEMATICAL PHYSIOLOGY OF THE AUTOREGULATION CURVE

6.1 Introduction

While the current formulation of the model [Mad14; Mad16] is able to accurately describe the dynamic response of cerebral autoregulation and predict the cerebral blood flow velocity, the incorporated static autoregulation curve is not formed using physiological princi-

ples. By integrating the Arciero et al. static models for blood flow regulation [Arc08; Arc13] into our model, valuable physiological insights can be obtained and the potential for a physiologically-based index of cerebral autoregulation arises. The static cerebral autoregulation is formulated using the polynomial function f_{aut} (Equation (5.6); also see Figure 6.7) to represent the steady-state relationship between blood pressure and normalized cerebral blood flow. However, this plateau curve, commonly referred to as the Lassen curve [Las59], is believed to shift in the presence of various disease states. For chronic hypertensive subjects, the curve is believed to be shifted to the right, likely because of medial hypertrophy and vascular remodeling of the cerebral arteries and arterioles [Cip07]. As shown in Figure 6.2, the curve shifts to lower pressures (left) in the presence of chronic hypotension [Ser01]. The Lassen curve also is believed to shift up and left during pregnancy [Cip07], and complete loss of autoregulation, meaning CBF changes linearly with pressure, is thought to occur during eclampsia (see Figure 6.1). In acute head injury, the autoregulatory curve is shifted to the right [Kin16]. The following sections will focus on the physiological considerations behind the static cerebral autoregulation curve. The penultimate goal will be using the Arciero model as a tool for generating various static curves within our model framework.

6.2   Arciero Model

Arciero et al. [Arc08] developed a theoretical model of metabolic blood flow regulation for skeletal muscle in the skin. The model for metabolic blood flow regulation based on oxygen saturation-dependent release of adenosine triphosphate (ATP) by red blood cells. These red blood cells carry oxygen in the blood and act as oxygen sensors. Thus, they have the ability to communicate metabolic demand. A segment model representing the seven
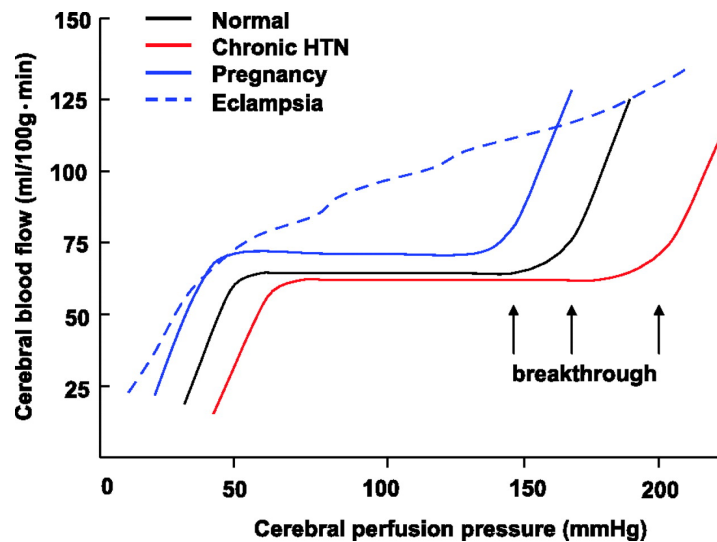
Figure 6.1 Lassen Curves Under Various Conditions. The solid black line represents normal CBF as a function of CPP. The solid red lines represents chronic hypertension (chronic HTN) in which the autoregulatory curve is shifted to the higher pressures. The solid blue line represents a potential shift in the autoregulatory curve during normal pregnancy. The arrows point to pressures at which breakthroughs occur, demonstrating a large, steep increased in CBF. The dashed blue line demonstrates loss of autoregulation in which CBF changes linearly with pressure and is thought to occur during eclampsia. Reproduced from [Cip07].
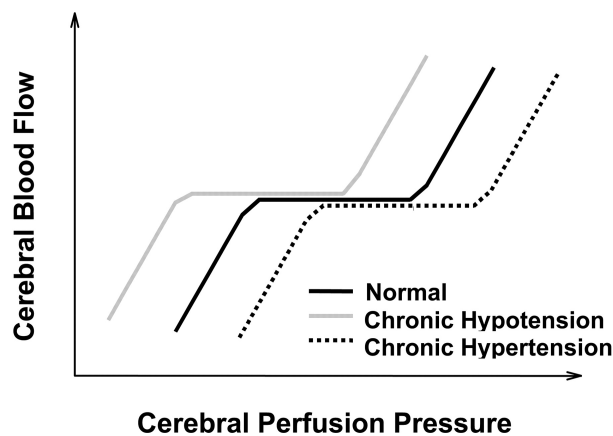
Figure 6.2 Lassen Curve Shifts. Theoretical shifts in cerebral autoregulation curve during chronic exposure to hypotension (gray line) or hypertension (dotted line). Reproduced from [Ser01].

branching vessel regions connected in series was used, where geometric and hemodynamic parameters were uniquely defined for each segment (see Figure 6.3). Three equations were developed to explain the effects of oxygen saturation, ATP concentration, and a conducted response signal. Since red blood cells deliver oxygen to surrounding tissue and respond to oxygen level by releasing ATP at a rate dependent on oxygen saturation level, the authors concluded that ATP release from RBCs initiates a conducted response that travels upstream and changes arteriolar diameter.
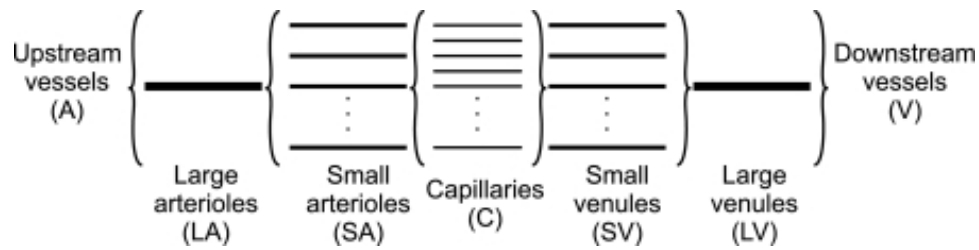
Figure 6.3 Vessel Network. Separations of representative segments used in theoretical model. Reproduced with permission from [Arc08].

6.2.1   Oxygen Saturation

The model assumes that oxygen is delivered to the surrounding tissue by the upstream vessels (A), large arterioles (LA), small arterioles (SA), and capillaries (C). Thus, no oxygen exchange is assumed in the venous segments (SV, LV, and V). Since the decline in oxygen flux must be equal to the rate of oxygen consumption (conservation of mass), an ODE for

oxygen saturation ($S(x)$) can be derived

$$\frac{d}{dx}[Q c_0 H_D S(x)] = -\pi M_0 \left(r_t^2 - r_v^2\right), \tag{6.1}$$

where M_0 is the oxygen demand, c_0 denotes the oxygen capacity of red blood cells, and H_D is the discharge hematocrit. The volumetric flow rate Q in an individual vessel i is given by

$$Q_i = \frac{\tau_i D_i^3 \pi}{32 \mu_i}, \tag{6.2}$$

where τ_i represents the shear stress in the wall of vessel i, D_i is the diameter of vessel i, and μ_i denotes the viscosity in vessel i. Equation (6.1) can be solved for oxygen saturation, yielding

$$S(x) = S(x_0) + \frac{\pi M_0 \left(r_t^2 - r_v^2\right)}{Q c_0 H_D}(x_0 - x). \tag{6.3}$$

Using the solution to the ODE for oxygen saturation and the provided parameter values, we were successfully able to predict the oxygen saturation reported by Arciero et al., see Figure 6.4.

6.2.2 ATP Release

Red blood cells (RBCs) respond to oxygen levels by releasing ATP at a rate dependent on the oxygen saturation level. To represent the release rate of ATP from RBCs, Arciero et al. [Arc08] define the linear function

$$R[S(x)] = R_0[1 - R_1 S(x)],$$

where R_0 is the maximal rate of ATP release and R_1 represents the effect of oxygen saturation on ATP release. The rate of change in plasma ATP concentration is defined by the difference between the rates of ATP release and ATP degradation. This rate of change is described by
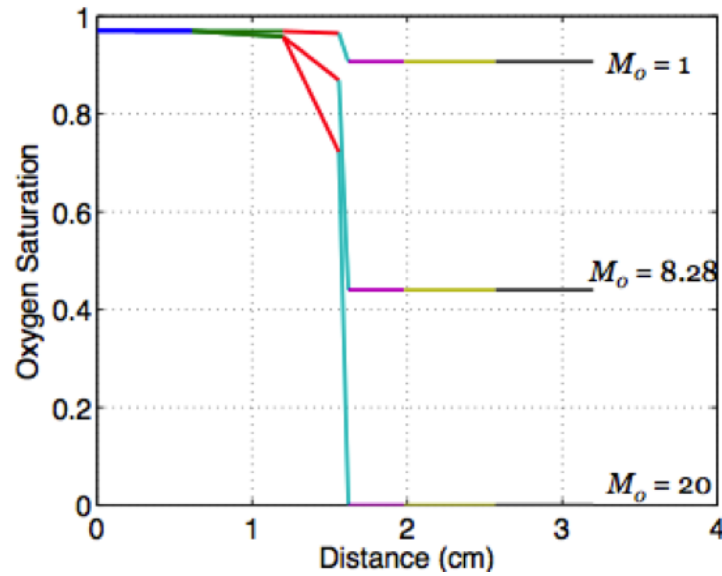
Figure 6.4 Oxygen Saturation. Model predictions for oxygen saturation along flow segments for three levels of exercise: $M_0 = 1$ (rest), $M_0 = 8.28$ (control; moderate exercise), and $M_0 = 20$ (heavy exercise). The changes in color indicate a change in vessel segment.

an ODE that can be solved for ATP concentration, $C(x)$.

$$\frac{d}{dx}[(1-H_D)QC(x)] = \frac{\pi}{4}D^2 H_T R_0 (1-R_1 S(x)) - k_d \pi D C(x)$$

$$\vdots$$

$$\underline{\text{Solution: }} C(x) = \alpha + \beta x + e^{\gamma(x_0-x)}\left(C_0 - \alpha - \beta x_0\right) \tag{6.4}$$

where

$$\alpha = \frac{H_T R_0}{4k_d}\left[D_i(1-R_1 S(x_0)) - \frac{(1-H_D)R_1 \pi M_0\left(r_t^2 - r_v^2\right)}{\pi C_0 H_D k_d}\right]$$

$$\beta = \frac{D_i H_T R_0 R_1 \pi M_0\left(r_t^2 - r_v^2\right)}{4Q_i C_0 H_D k_d}$$

$$\gamma = \frac{k_d \pi D_i}{(1-H_D)Q_i}$$

Using this solution to the ODE and the given parameters (see Table 6.1), we were successfully able to predict the ATP concentration reported by Arciero et al., see Figure 6.5.

6.2.3 Conducted Response Signal

The ATP release from RBCs initiates a conducted response that travels upstream and triggers arteriolar vasodilation. The conducted response signal, SCR, was computed differently than what was originally reported in the paper. Here, we integrate the ATP concentration at each x position to the end of the large venules (x_{end}) using by the equation

$$S_{CR}(x) = \int_x^{x_{end}} e^{\frac{-(y-x)}{L_0}} C(y)dy. \tag{6.5}$$

110
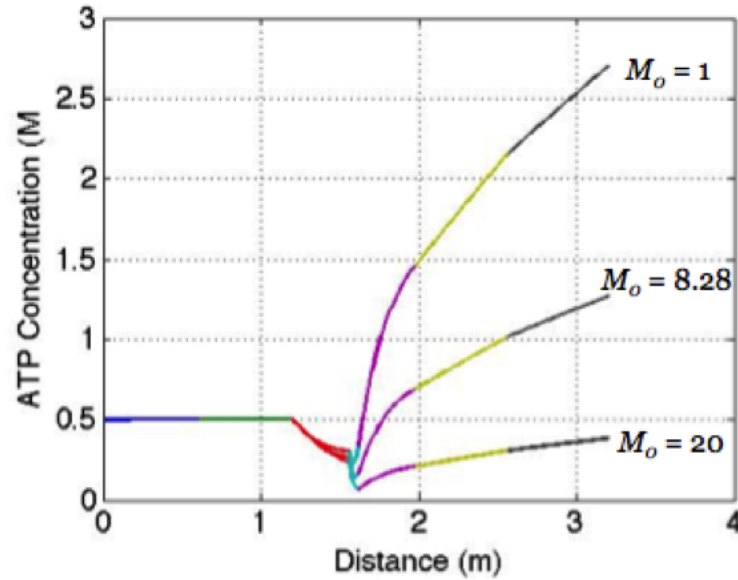
Figure 6.5 ATP Release. Model predictions for ATP concentration along flow pathway for three levels of exercise: $M_0 = 1$ (rest), $M_0 = 8.28$ (control; moderate exercise), and $M_0 = 20$ (heavy exercise). The changes in color indicate a change in vessel segment.

At each point in the network, a signal is generated at the vessel wall in proportion to the local concentration of ATP in the plasma. Metabolic control of the large arteriole and small arteriole diameters occurs via SCR, assuming exponential decay of the signal in the upstream direction. Using the values obtain for the ATP concentration at each point along the vascular network along with Equation (6.5), we were successfully able to predict the conducted response signal reported by Arciero et al., see Figure 6.6.

6.2.4   Activation & Diameter

When the pressure is altered within a vessel, it shows a rapid passive change in diameter followed by an active smooth muscle contraction or dilation to a new equilibrium diameter.

This behavior is represented by the ODE system below.

$$\frac{dD_i}{dt} = \frac{1}{\tau_d}\frac{D_c}{T_c}(T_i - T_{total})$$

$$\frac{dA_i}{dt} = \frac{1}{\tau_a}(A_{total} - A_i),$$

where A_{total} is smooth muscle activation, τ_d, represents the time constant for diameter change, τ_a is the time constant for activation changes, and D_c and T_c are the control state values of diameter and tension. This system is composed of two coupled ODES and various algebraic equations, making it difficult to solve analytically. The total circumferential wall
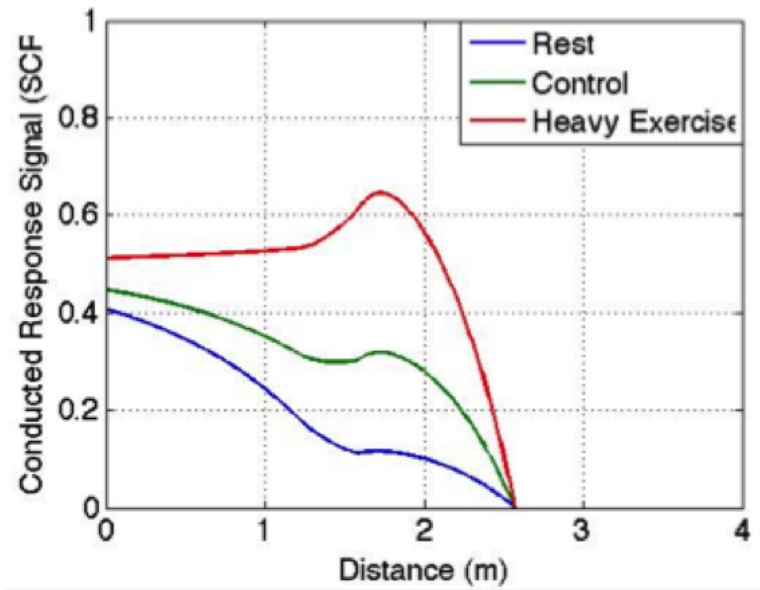
Figure 6.6 Conducted Response. Model predictions for the conducted response signal along flow pathway for three levels of exercise: $M_0 = 1$ (rest), $M_0 = 8.28$ (control; moderate exercise), and $M_0 = 20$ (heavy exercise).

tension T_{total} is given by

$$T_{total} = T_{pass} + AT_{act}^{max}.$$ (6.6)

Here, T_{pass} represents the passive wall tension generated by the structural components of the vessel wall, given by

$$T_{pass} = C_{pass} \cdot \exp\left[C'_{pass} \left(\frac{D}{D_0} - 1 \right) \right],$$ (6.7)

where C_{pass} and C'_{pass} are parameters representing passive tension strength and sensitivity. D_0 is the passive reference vessel diameter. The maximum degree of active wall tension that can be generated in response to maximal constriction of the vascular smooth muscle cells is represented by

$$T_{act}^{max} = C_{act} \cdot \exp\left[-\left(\frac{\frac{D}{D_0} - C'_{act}}{C''_{act}} \right)^2 \right],$$ (6.8)

where C_{act}, C'_{act}, and C''_{act} are parameters describing the maximally active vascular smooth muscle peak tension, length dependence, and tension range, respectively. Note that the total tension is generated in the resistance vessels, e.g. the large and small arterioles [Arc13]. The vascular smooth muscle tone is described using the equation

$$A = \frac{1}{1 + \exp(-S_{tone})}.$$ (6.9)

The level of activation, which is a sigmoidal value between 0 and 1, depends on the stimulus function S_{tone}. Various terms can be included in S_{tone} to account for one (or all) of the CA mechanisms, contributing to the level of smooth muscle response. To include the myogenic,

shear-dependent, and metabolic regulatory mechanisms, the stimulus function can be constructed as

$$S_{tone} = C_{myo} T - C_{shear} \tau - C_{meta} S_{CR} + C_{tone}^{''}. \tag{6.10}$$

The coefficients C_{myo}, C_{shear}, C_{meta}, and $C_{tone}^{''}$ are parameters. Please consult Table 6.1 for a detailed description of all model parameters. For simplicity, let's only include the myogenic response to begin with. Thus, we will define the stimulus function as

$$S_{tone} = C_{myo} T - C_{tone}^{''}, \tag{6.11}$$

where C_{myo} is a parameter representing vascular smooth muscle activation tension sensitivity and $C_{tone}^{''}$ is a constant. Using the definitions of tension and activation, the ODE system describes diameter changes in the vessel wall due to smooth muscle behavior. The key link between tension and diameter comes from the Law of Laplace. Circumferential wall tension (T) is related to pressure and diameter by the Law of Laplace ($T = \frac{PD}{2}$), assuming that vessel wall thickness is much less than vessel diameter.

6.2.5 Autoregulation Curve

The Lassen curve describing the static CA response can be found as a collection stable equilibria. Equilibrium of differential systems can be found by setting the ODEs equal to zero. In this example, we want to find equilibrium solutions by setting $\frac{dD}{dt} = 0$ and $\frac{dA}{dt} = 0$. Notice that the steady-state values are independent of the values chosen for the time constants τ_d and τ_a. The D-nullcline is the set of points where $\frac{dD}{dt} = 0$, and the A-nullcline is the set of points where $\frac{dA}{dt} = 0$. The points of intersection between these two nullclines

Parameter	Description
M_0	oxygen demand
$S(0)$	initial oxygen concentration
c_0	oxygen capacity of red blood cells
H_D	discharge hematocrit
C_{pass}	passive tension strength
C'_{pass}	passive tension sensitivity
C_{act}	maximally active VSM peak tension
C'_{act}	maximally active VSM length dependence
C''_{act}	maximally active VSM tension range
D_0	passive reference vessel diameter
D_i	diameter of vessel i
k_d	rate of ATP degradation
R_0	maximal rate of ATP release
R_1	effect of saturation on ATP release
H_T	tube hematocrit
L_0	length constant
τ_d	time constant for diameter (1 sec)
τ_a	time constant for activation (60 sec)
C_0	initial ATP concentration in vessel
x_0	initial position in vessel (0 cm)
x_{end}	downstream S_{CR} position (2.57 cm)
τ_{wall}	vessel wall shear stress
C_{myo}	VSM activation tension sensitivity
C_{shear}	VSM activation shear stress sensitivity
C_{meta}	VSM activation conducted response sensitivity
C''_{tone}	VSM constant

Table 6.1 Arciero Model Parameters. Description and associated values for parameters used in the Arciero et al. [Arc08] theoretical model.

are exactly the equilibrium points. First, let's look at the nullcline for diameter.

$$\frac{dD}{dt} = \frac{2}{P_{REF}} \left(\frac{T - T_{total}}{\tau_d} \right) = 0 \text{ when } T = T_{total}.$$
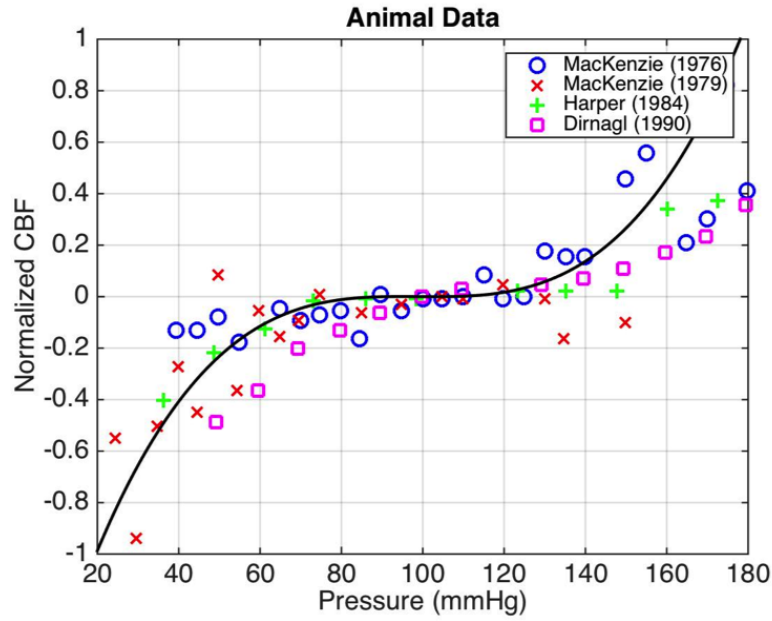
Figure 6.7 Static Autoregulation. Current function in the model [Mad14] to incorporate the static CA curve, plotted against the same animal data from Figure 6.10

The nullclines for the diameter ODE occur when $D = 0$ and $D = 198$, when using a reference pressure of 100 mmHg. Now let's explore the nullcline for activation, including only the myogenic regulatory response in the formulation for S_{tone}.

$$\frac{dA}{dt} = \left(\frac{A_{total} - A}{\tau_a}\right) = 0 \text{ when } A = A_{total}.$$

$$
\begin{aligned}
A &= A_{total} \\
&= \frac{1}{1+\exp(-S_{tone})} \\
&= \frac{1}{1+\exp\left(-C_{myo}T + C'_{tone}\right)} \\
&= \frac{1}{1+\exp\left(-C_{myo}\frac{PD}{2} + C'_{tone}\right)}.
\end{aligned}
$$

The nullclines for diameter and activation intersect at two points (see Figure 6.8). This phase portrait was generated using *pplane*. Thus, there are two equilibria for the system. One equilibria occurs at ($D = 0$, $A = 0$). This is a saddle point (unstable). However, since both quantities are zero, this equilibrium point is of little interest physiologically. The other equilibrium point occurs at ($D = 198$, $A = 1$). This point is a nodal sink (stable), meaning that the eigenvalues are real, distinct, and negative. It is important to note that this equilibrium point was found for a reference diameter value of $D_0 = 156\mu$m, which is the passive reference vessel diameter in the large arterioles [Arc08].

By solving the system to steady-state for various vessel reference diameters, we can obtain the curve representing the static response of CA (see Figure 6.9). As you can see, this doesn't match the theoretical Lassen curve. However, from looking at Figure 6.10, you will notice that by including the myogenic response alone, it is not possible to obtain the plateau-like CA curve. In fact, in order to obtain the accurate plateau curve, all three responses (myogenic, shear, and metabolic) must be active.

6.3 Conclusion

Future work will extend our model to account for all mechanisms. This could be done combining existing animal data (e.g. Virtual Physiological Rat Project) with dynamic data used in the current study to add physiological meaning to the current autoregulatory curve in the model [Mad14; Mad16], shown in black in Figure 6.7. Shifts of the static f_{aut} curve are shown in Figure 6.11. Model output and associated error using the arithmetic shifts of our static CA curve to estimate CBFV on a hypertensive elderly subject are given in Figure 6.12(a) and Figure 6.12(b), respectively. By using the f_{aut} function shifted to the right, a slightly better fit is obtained (green). Hypertension is said to shift the static CA curve to the right. One possible way to incorporate metabolic control into the system is through a conducted response signal, similar to what is found in [Arc08]. The central idea behind conducted responses is that adenosine triphosphate (ATP) release from red blood cells initiates a response that can travel upstream to trigger arteriolar vasodilation. These remote responses occur via cell-to-cell communication along the vessel wall. This idea is based on experimental results, showing that when ATP is applied intraluminally to collecting venules the result is an increase in vessel diameter of upstream arterioles [Col98]. Metabolic control has been used for autoregulation in other parts of the body, including the retina [Arc13]. In particular, the activation coefficients representing the myogenic (C_{myo}), shear-dependent (C_{shear}), and metabolic (C_{meta}) responses can be estimated using experimental data. Additionally, a mechanism describing the effects of carbon dioxide can be included since tissue levels of P_{CO2} and pH have been shown to be significant factors in retinal and brain autoregulation [Kon77; Pou08].

x´ = (2/100)*(50*x−(1043*exp(8.3*(x/156−1))))
y´ = (1/60)*(1/(1+exp(10.11−0.01*50*x))−y)
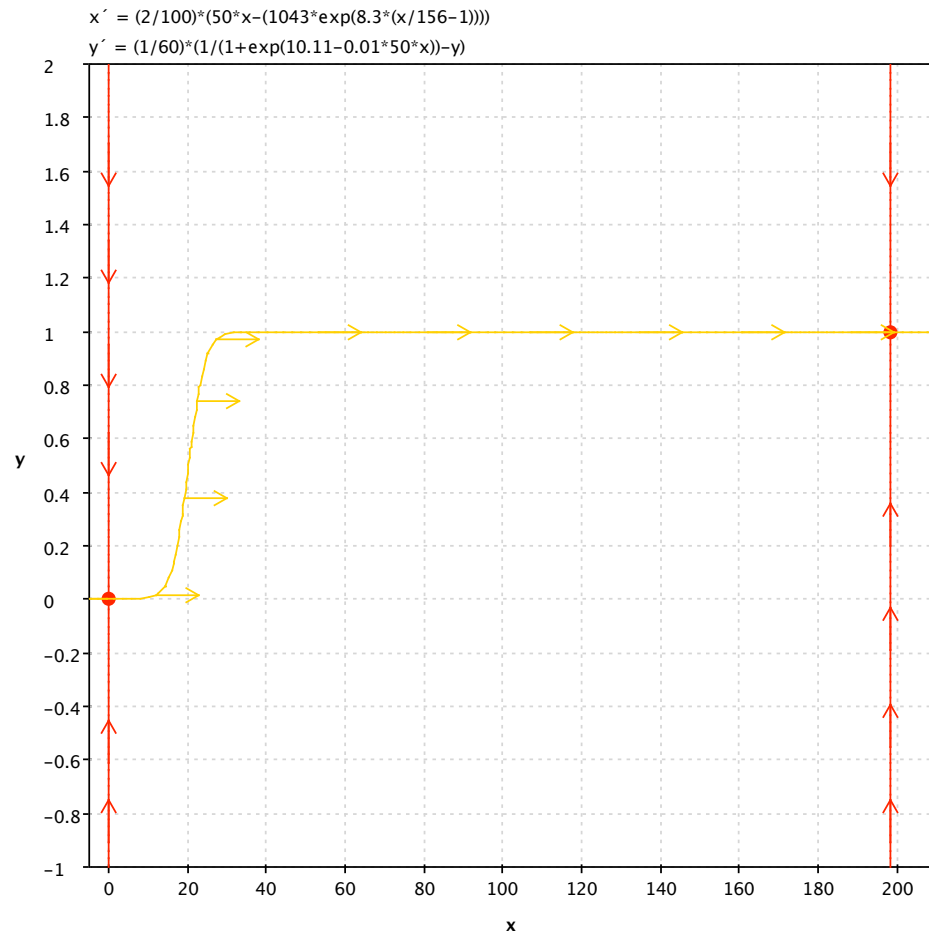
Figure 6.8 Phase Plane. Phase plane snapshot of the ODE system for diameter (horizontal axis) and activation (vertical axis). The nullclines are plotted, and the intersection of these nullclines denoted the equilibria of the system. There are two equilibrium points for this system.

119
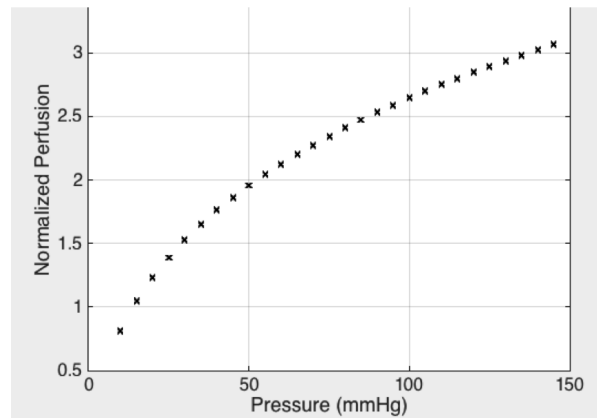
Figure 6.9 Passive Response. Relationship between blood pressure and blood flow (perfusion) using the model accounting for smooth muscle (myogenic) response
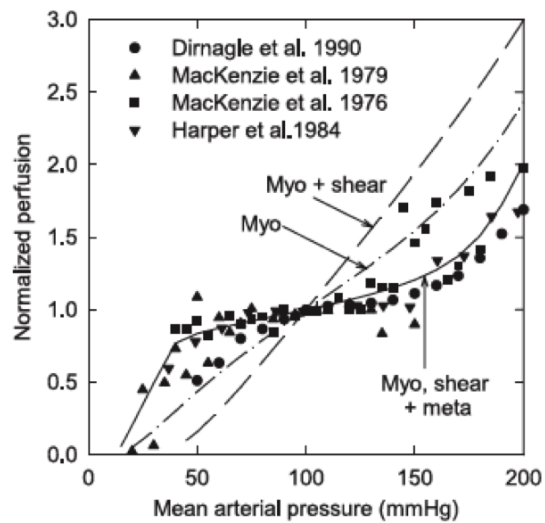
Figure 6.10 Autoregulation Curve. Relationship between blood pressure and perfusion depicting experimental animal data and the effects that combining the autoregulatory responses can have. Using the myogenic response alone is not sufficient enough to observe the CA curve. Reproduced with permission from [Car08].
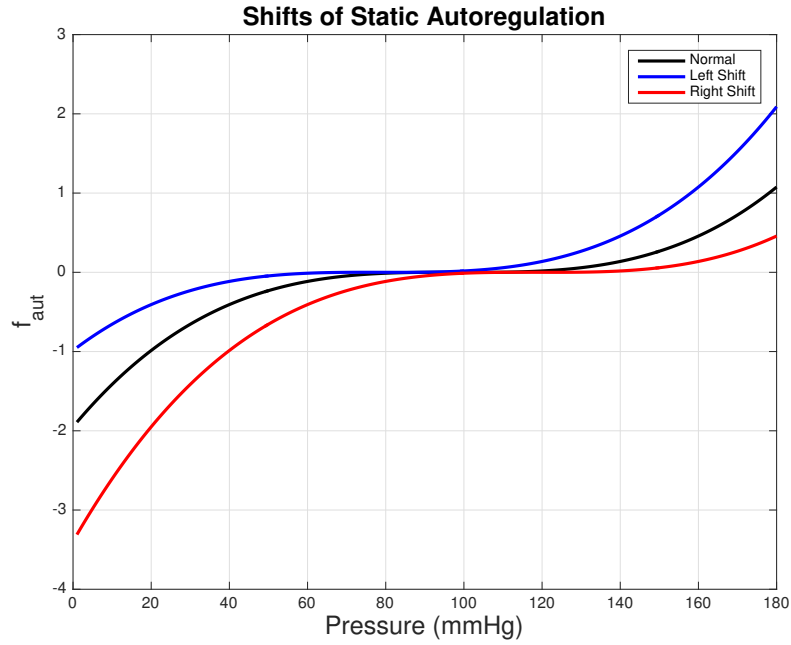
Figure 6.11 Shifts of f_{aut}. Arithmetic translations of f_{aut} to portray shifts of the static autoregulation curve used in our model. Having physiological quantities determining f_{aut} would allow the model and its parameters to be clinically useful.

| (a) | (b) |
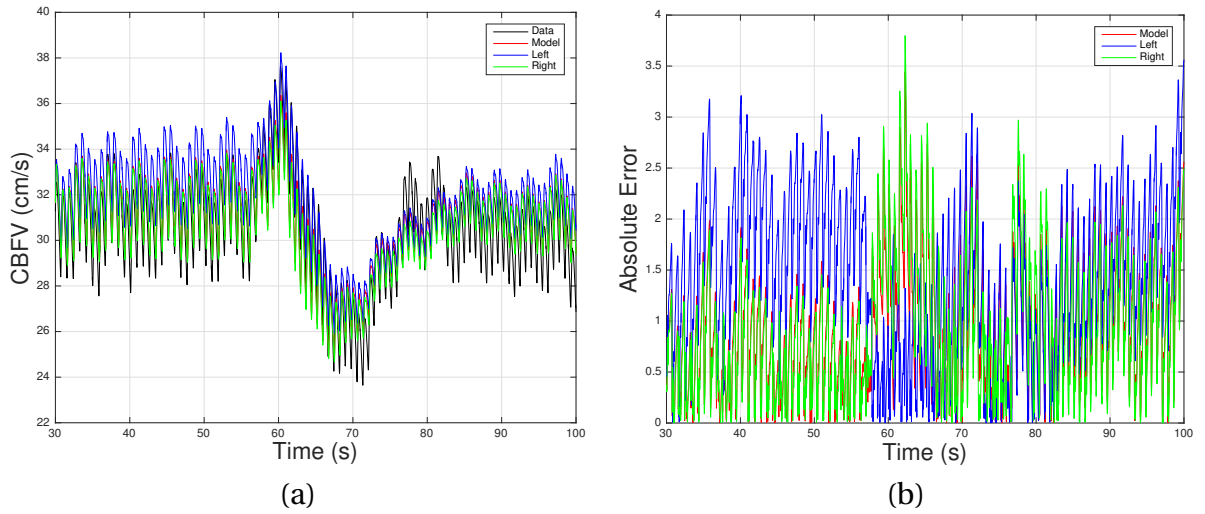
Figure 6.12 Model Output Using Shifts. Model output (a) and absolute error (b) using the arithmetic shifts of our static CA curve to estimate CBFV on a hypertensive elderly subject. Note that by using the f_{aut} function shifted to the right, a slightly better fit is obtained (green). Hypertension is said to shift the static CA curve to the right.

CHAPTER

7

DISCUSSION

7.1   Summary

This study developed a nonlinear dynamic model predicting cerebral autoregulation in three groups of subjects, including healthy young, healthy elderly, and hypertensive elderly. The model uses filtered blood pressure to predict cerebral blood flow velocity. Sensitivity and identifiability analysis were used to identify a set of parameters capable of being estimated given the model and available data. This parameter subset was estimated for each subject

and optimized values were compared within and between the three groups. Results showed that, when accounting for some pulsatility, it is possible to distinguish the three groups.

To our knowledge, this is the first model of cerebral autoregulation using sensitivity and identifiability analysis to determine the subset of parameters estimated, and the first that is able to detect differences between all three patient groups. These results are novel and have the potential to make an important contribution to the field of cerebral hemodynamics.

The ARI model defines an autoregulatory index based on estimated parameter values. A similar approach could be used for the model studied here. Even though parameters cannot be related to physiologically measured quantities, they still represent physical biomarkers describing the differences both within and between groups of subjects.

The use of parameters and/or parameter combinations as biomarkers require that they are identifiable. For this study we showed that the linear model (when $f_{aut} = 0$) is structurally and practically identifiable. For the full nonlinear model (when $f_{aut} \neq 0$) it is not possible to prove show structural identifiability analytically. If the CA curve is approximated by a piecewise linear function, identifiability can be proven analytically. Regardless, subsequent local sensitivity and identifiability analysis showed that parameters a, b, M, and k can be estimated reliably given the model and the data.

7.2   Effects of Aging and Hypertension

Current methods for assessment of cerebral autoregulation, like the autoregulatory index [Tie95] and transfer function analysis [Zha98], have not found differences in autoregulation in aging and hypertension. There are two differences between these models and the one proposed here: A) we include some pulsatility in the filtered input pressure data, and

B) our model combines the nonlinear static Lassen curve with the dynamic model.

More specifically we showed that differences due to aging can be quantified through model parameter a. A larger value of the Voigt body parameter a indicates a longer adaptation recovery time following decrease in pressure. Dynamic CBFV response differences are observed in the presence of disease through model parameter M, indicating a decreased overal viscoelastic response and a slower rate of recovery. These two parameters represent possible biomarkers of the assessment and evaluation of CA.

Our results showed that without accounting for pulsatility, the three groups could not be distinguished. In addition, the proposed model provided good estimates of cerebral blood flow velocity for all human subjects. Blood pressure was used as an input for all simulations. Most of the healthy control subjects had pressure values within the cerebral autoregulatory range, while the normotensive elderly and hypertensive elderly patients often had either low or high pressure outside the static range. More studies should be carried out investigating the effect of shifting the static cerebral autoregulation curve as discussed in Chapter 6. To test the nonlinearity versus pulsatility, the filter used in our studies could be used within the linear ARI and TFA models.

The data analyzed in this study were all extracted from patients with intact cerebral autoregulation. More studies are needed to test if our model is able to identify impaired CA. One limitation of our model is that it requires an input signal accounting for variation in pressure. Many patients with impaired cerebral autoregulation are in intensive care units, where postural changes are difficult to impose. Thus, more studies are needed to test if natural variation in blood pressure signals are adequate to analyze dynamics.

While its simplicity makes the model computationally feasible to work with, it may be

difficult to infer what specific physiological mechanisms were compromised. Moreover, this type of model is not yet able to predict the cause of disease. One way to improve the current approach could be by incorporating some mechanisms present in physiologically-based models, e.g. [Arc08], at the same time keeping it computationally efficient. The advantage of the detailed physiologically-based models [UL97; UL98; Urs00; Pay06; Spr12] is that they can be used to understand how each mechanism impacts the overall dynamics, a feature not yet provided by our study. The disadvantage is the high number of parameters, which are typically unidentifiable, making the model difficult to validate against experimental data.

On the other hand, data driven models are simple and can easily be built in to clinical devices. The TFA and ARI models are purely empirical; whereas, the model developed in this study was constructed using mechanical principles governing the viscoelastic response of arterioles. Blood vessels exhibit viscoelastic properties, and the cerebral arteries responsible for regulating the flow of blood likely experience viscoelastic deformation [Fun93]. In our study the static autoregulation curve was defined empirically, yet in Chapter 6 we discussed how this sub-model could be expanding separating each of the four mechanisms (described in Chapter 2) associated with cerebral autoregulation.

7.3   Conclusion

There have been various model-based approaches to assessing cerebral autoregulation, including autoregulation index (ARI) [Tie95], autoregressive-moving average (ARMA) [Pan03a], autoregressive exogenous (ARX) [LA02; Liu03], and transfer function analysis (TFA) [Gil90; Pan96; Zha98]. Of these, the ARI is commonly used in the clinical applications to evaluate

CA performance. As previously discussed, Tiecks et al. [Tie95] propose a set of equations for cerebral blood flow velocity in response to a sudden drop in blood pressure from which an ARI can be calculated. The mean velocity was approximated using a second-order linear differential equation system. Our model for assessing CA is very similar [Mad14]. Both approaches incorporate an approximation of mean velocity.

While our model can be used with pulsatile signals, the penultimate goal of our model is to predict the dynamics of the mean cerebral blood flow velocity during some ortho-static stress, not necessarily the pulsatile response. Both models are characterized by few parameters. In the Tiecks model, the method is characterized by three parameters: T (time constant), D (damping factor), and K (autoregulatory dynamic gain). By taking all three parameters into account, an ARI is generated, ranging from 0 (no autoregulation) to 9 (best autoregulation). Our model also has few parameters, consisting of four total estimated parameters. While we have yet to link the parameters to physiological relevance (see Chapter 6), they can be considered as indices in their own right, with each describing differences in dynamic responses across the population. In our model, M might be the closest parameter we have to a standalone index. Varying M results in the severity of drop, overshoot, and recovery, which can mimic the responses found in this plot.

Both systems have two ODE states. In the Tiecks model, x_1 and x_2 represent the states, which are equal to zero during the control state. Similarly, in our model, the states are represented by v_1 and v_2. However, during the control state (steady state), our model is equal to the static CA curve, which describes the relationship between normalized cerebral blood flow velocity and arterial blood pressure. In the Tiecks model, the steady state is the function $dP(t)$, which is simply the normalized change in mean arterial blood pressure

126

obtained from filtering the pulsatile ABP signal. The main difference between the two methods, in terms of structure, is that our approach is nonlinear; whereas, the Tiecks model is a linear differential equation set. Our inclusion of nonlinearity was motivated by the Lassen curve [Las59] and is justified by the physiological considerations or diameter dilation and constriction across various pressures.

We consider our model to be based on a similar structure of the ARI model. Our extension of the method can be used to gain more insight into the dynamics of the flow velocity, with the possibility of being a tool for predicting CBFV response given an ABP stimulus and knowing the disease state and/or age of the patient. One problem with the ARI method and similar data-driven approaches is the variability of assessment predictions for a given individual. The index provided for a subject can vary depending on which part of the pressure signal being analyzed. A recent study by Mahdi et al. [Mah16] found improved reproducibility of autoregulation indices when individuals are standing. We hope to address this issue by providing a clinical approach to assessing CA on a patient-specific basis with minimal variability.

To improve repeatability of the findings in this study, the model should be validated on an independent dataset. Thus, we would be able to test whether the model can correctly identify subjects in a new dataset. In particular, the model could be used on data for those individuals known to have intact or compromised autoregulation. Model results using these data can then be compared to existing methods, which so far have shown an insensitivity to detect changes between the prescribed subgroups.

Since autoregulation is a nonlinear phenomenon [Las59], we believe that our model [Mad14; Mad16] is advantageous over linear approaches. By incorporating some mathematical

implementation for the metabolic, myogenic, and shear-dependent autoregulatory mechanisms, model parameters would have more physiological meaning. More insight into how to interpret the parameters and what the parameters mean in terms of autoregulation could be obtained.

A new physiologically-based index for CA could be determined using the parameters or a combination of the parameters. By incorporating nonlinearity, pulsatility, and physiology within a mathematical framework, our model and its output might not endure the same inconsistencies and irreproducibility of the ARI model.

BIBLIOGRAPHY

[Aas82]   Aaslid, R et al. "Noninvasive transcranial Doppler ultrasound recording of flow velocity in basal cerebral arteries". *J Neurosurg* **57** (1982), pp. 769–774.

[Aas89]   Aaslid, R et al. "Cerebral autoregulation dynamics in humans". *Stroke* **282** (1989), pp. 45–52.

[Ain08]   Ainslie, P. et al. "Dynamic cerebral autoregulation and baroreflex sensitivity during modest and severe step changes in arterial PCO2". *Brain Research* **1230** (2008), pp. 115–124.

[Aoi09]   Aoi, M. *Nonlinear, Noninvasive Assessment of Patient-Specific Cerebral Autoregulation in Stroke Subjects*. Ph.D. thesis. Raleigh: North Carolina State University, 2009.

[Arc13]   Arciero, J et al. "Theoretical analysis of vascular regulatory mechanisms contributing to retinal blood flow autoregulation". *Invest Ophthalmol Vis Sci* **54** (2013), pp. 5584–5593.

[Arc08]   Arciero, J. et al. "Theoretical model of metabolic blood flow regulation: roles of ATP release by red blood cells and conducted responses". *Am J Physiol Heart Circ Physiol* (2008), H1562–H1571.

[Att10]   Attwell, D et al. "Glial and neuronal control of brain blood flow". *Nature* **468** (2010), pp. 232–243.

[Aud01]   Audoly, S et al. "Global identifiability of nonlinear models of biological systems". *IEEE Trans Biomed Eng* **48** (2001), pp. 55–65.

[Ban05]   Banaji, M et al. "A physiological model of cerebral blood flow control". *Math Biosci* **194** (2005), pp. 125–173.

[Bea11]   Beal, S et al. *NONMEM user guides (1989-2011*. Ellicott City: Technical Report, Icon Development Solutions, 2011.

[Bee08]   Beek, A. van et al. "Cerebral autoregulation: an overview of current concepts and methodology with special focus on the elderly". *J Cereb Blood Flow Metab* **28** (2008), pp. 1071–1085.

[Bee10]   Beek, A. van et al. "Dynamic cerebral autoregulation in the old using a repeated sit-stand maneuver". *Ultrasound Med Biol* **36** (2010), pp. 192–201.

[BP10]   Bendat, J. & Piersol, A. *Random data: analysis and measurement procedures*. 4th. Hoboken, NJ: John Wiley & Sons, Inc, 2010.

[BH85]   Bevan, J. & Hwa, J. "Myogenic tone and cerebral vascular autoregulation: the role of a stretch-dependent mechanism". *Ann Biomed Eng* **13** (1985), pp. 281–286.

[Bla08]   Black, M. et al. "Importance of measuring the time course of flow-mediated dilatation in humans". *Hypertension* **51** (2008), pp. 203–210.

[Bon11]   Bonate, P. *Pharmacokinetic-pharmacodynamic modeling and simulation*. New York: Springer, 2011.

[Cam99]   Campbell, N. et al. *Biology*. 5th. Benjamin/Cummings, 1999.

[Car00]   Carey, B. et al. "Dynamic cerebral auto regulation is unaffected by aging". *Stroke* **31** (2000), pp. 2895–2900.

[Car03]   Carey, B. et al. "Effect of aging on dynamic cerebral autoregulation during head-up tilt". *Stroke* **34** (2003), pp. 1871–1875.

[Car08]   Carlson, B. et al. "Theoretical model of blood flow autoregulation: roles of myogenic, shear-dependent, and metabolic responses". *Am J Physiol Heart Circ Physiol* (2008), H1572–H1579.

[Chr71]   Christensen, R. M. *Theory of viscoelasticity, an introduction*. New York, London: Academic Press, 1971.

[Cip07]   Cipolla, M. "Cerebrovascular function in pregnancy and eclampsia". *Hypertension* **50** (2007), pp. 14–24.

[Cla16]   Classen, J. et al. "Transfer function analysis of dynamic cerebral autoregulation: a white paper from the International Cerebral Autoregulation Research Network". *J Cereb Blood Flow Metab* **36** (2016), pp. 665–680.

[Col98]   Collins, D. et al. "Conducted vascular responses: communication across the capillary bed". *Microvasc Res* **56** (1998), pp. 43–53.

[CY72]   Cook, T. & Yates, P. "A histometric study of cerebral and renal arteries in normotensive and chronic hypertensives". *J Pathol* **108** (1972), pp. 129–135.

[Czo96]   Czosnyka, M et al. "Monitoring of cerebral autoregulation in head-injured pa-
           tients". *Stroke* **27** (1996), pp. 1829–1834.

[Czo97]   Czosnyka, M et al. "Contribution of mathematical modelling to the interpre-
           tation of bedside tests of cerebrovascular autoregulation". *J Neurol Neurosurg
           Psychiatry* **63** (1997), pp. 721–731.

[Dau08]   Daun, S et al. "An ensemble of models of the acute inflammatory response to
           bacterial lipopolysaccharide in rats: results from parameter space reduction". *J
           Theor Biol* **253** (2008), pp. 843–853.

[Dav09]   David, T et al. "Coupled autoregulation models in the cerebro-vasculature". *J
           End Math* **64** (2009), pp. 403–415.

[DG95]   Davidian, M & Giltinian, D. *Nonlinear models for repeated measurement data*.
           Chapman & Hall, 1995.

[Dee10]   Deegan, B. et al. "The relationship between cardiac output and dynamic cerebral
           autoregulation in humans". *J Appl Physiol* **109** (2010), pp. 1424–1431.

[DP90]   Dirnagl, U & Pulsinelli, W. "Autoregulation of cerebral blood flow in experimental
           focal brain ischemia". *J Cereb Blood Flow Metab* **10** (1990), pp. 327–336.

[Eam02]   Eames, P. et al. "Dynamic cerebral autoregulation and beat to beat blood pres-
           sure control are impaired in acute ischemic stroke". *J Neurology, Neurosurgery,
           and Psychiatry* **72** (2002), pp. 467–472.

[Eam03]   Eames, P. et al. "Cerebral autoregulation indices are unimpaired by hypertension
           in middle aged and older people". *Am J Hypert* **16** (2003), pp. 746–753.

[EK02]   Edvinsson, L & Krause, D. *Cerebral blood flow and metabolism*. 2nd. Philadel-
           phia: Lippincott, Williams and Wilkins, 2002.

[Ell08]   Ellwein, L. et al. "Sensitivity analysis and model assessment: mathematical
           models for arterial blood flow and blood pressure". *J Cardiovasc Eng* **8** (2008),
           pp. 94–108.

[Elt14]   Elting, J. et al. "Reproducibility and variability of dynamic cerebral autoregula-
           tion during passive cyclic leg raising". *Med Eng Phys* **36** (2014), pp. 585–591.

[Fle86]   Fleg, J. "Alterations in cardiovascular structure and function with advancing age". *Am J Cardiol* **57** (1986), pp. 33–44.

[Flü75]   Flügge, W. *Viscoelasticity*. New York: Springer Verlag, 1975.

[Fu05]   Fu, C. et al. "Effects of different classes of antihypertensive drugs on cerebral hemodynamics in elderly hypertensive patients". *Am J Hypertens* **18** (2005), pp. 1621–1625.

[Fuj95]   Fujishima, M et al. "Cerebral blood flow and brain function in hypertension". *Hypertens Res* **18** (1995), pp. 111–117.

[Fun93]   Fung, Y. *Biomechanics: Mechanical Properties of Living Tissues*. New York: Springer Verlag, 1993.

[Gil90]   Giller, C. "The frequency-dependent behavior of cerebral autoregulation". *Neurosurgery* **27** (1990), pp. 362–368.

[Gil03]   Giller, C. "The emperor has no clothes: velocity, flow, and the use of TCD". *J Neuroimag* **13** (2003), pp. 97–98.

[Goa04]   Goadsby, P. *Chapter 36: Cerebral circulation - autonomic influences*. Primer on the Autonomic Nervous System. Elsevier Inc, 2004, pp. 144–146.

[Gos71]   Gosling, R. et al. "The quantitative analysis of occlusive peripheral arterial disease by a non-intrusive ultrasonic technique". *Angiology* **22** (1971), pp. 52–55.

[Haj90]   Hajdu, M. et al. "Effects of aging on mechanics and composition of cerebral arterioles in rats". *Circ Res* **66** (1990), pp. 1747–1754.

[Hal11]   Hall, J. *Guyton and Hall textbook of medical physiology*. 12th. Philadelphia, PA: Saunders, Elsevier, 2011.

[Hal16]   Hall, J. *Guyton and Hall textbook of medical physiology*. 13th. Philadelphia, PA: Elsevier, 2016.

[HT14]   Hamner, J. & Tan, C. "Relative contributions of sympathetic, cholinergic, and myogenic mechanisms to cerebral auto regulation". *Stroke* **45** (2014), pp. 1771–1777.

[Har79]   Harper, S. et al. "Arterial and microvascular contributions to cerebral cortical autoregulation in rats". *Am J Physiol Heart Circ Physiol* **246** (1979), H17–H24.

[HP14]   Hawthorne, C & Piper, I. "Monitoring of intracranial pressure in patients with traumatic brain injury". *Front Neurol* **5** (2014), pp. 1–16.

[HR91]   Holstein-Rathlou, N. et al. "Tubuloglomerular feedback dynamics and renal blood flow autoregulation in rats". *Am J Physiol* **260** (1991), F53–F68.

[Hu08]   Hu, K et al. "Altered phase interactions between spontaneous blood pressure and flow fluctuations in type 2 diabetes mellitus: nonlinear assessment of cerebral autoregulation". *Phys A* **387** (2008), pp. 2279–2292.

[Jac85]   Jacquez, J. *Compartmental analysis in biology and medicine*. 2nd. Ann Arbor, MI: Univ of Michigan Press, 1985.

[Kan78]   Kannel, W. "Evaluation of cardiovascular risk in the elderly: the Framingham Study". *Bull N Y Acad Med* **54** (1978), pp. 573–591.

[Kas12]   Kashif, F. et al. "Model-based noninvasive estimation of intracranial pressure from cerebral blood flow velocity and arterial pressure". *Sci Transl Med* **4** (2012), 129ra44.

[Kel99]   Kelley, C. *Iterative Methods for Optimization*. Philadelphia, PA: SIAM, 1999.

[Kin16]   Kinoshita, K. "Traumatic brain injury: pathophysiology for neurocritical care". *J Intensive Care* **4** (2016), pp. 1–10.

[Kon77]   Kontos, H. et al. "Analysis of vasoactivity of local pH, PCO2 and bicarbonate on pial vessels". *Stroke* **1** (1977), pp. 358–360.

[KH98]   Krabbe-Hartkamp, M. et al. "Circle of Willis: morphologic variation on three-dimensional time-of-flight MR angiograms". *Radiology* **201** (1998), pp. 103–111.

[Kre99]   Krejza, J et al. "Transcranial color Doppler sonography of basal cerebral arteries in 182 healthy subjects: age and sex variability and normal reference values for blood flow parameters". *AJR Am J Roentgenol* **172** (1999), pp. 213–218.

[Lan07]   Lanzarone, E et al. "Model of arterial tree and peripheral control for the study of physiological and assisted circulation". *Med Eng Phys* **29** (2007), pp. 542–555.

[Las59]   Lassen, N. "Cerebral blood flow and oxygen consumption in man". *Physiol Rev* **39** (1959), pp. 183–238.

[Lip00]   Lipsitz, L. et al. "Dynamic regulation of middle cerebral artery blood flow velocity in aging and hypertension". *Stroke* **31** (2000), pp. 1897–1903.

[LA02]   Liu, Y & Allen, R. "Analysis of dynamic cerebral autoregulation using an ARX model based on arterial blood pressure and middle cerebral artery velocity simulation". *Med Biol Eng Comput* **40** (2002), pp. 600–605.

[Liu03]   Liu, Y et al. "Dynamic cerebral autoregulation assessment using an ARX model: comparative study using step response and phase shift analysis". *Med Eng Phys* **25** (2003), pp. 647–653.

[Lu14]   Lu, J et al. "Online transcranial Doppler ultrasonographic control of an onscreen keyboard". *Front Hum Neurosci* **8** (2014), pp. 1–11.

[Mac76]   MacKenzie, E. et al. "Effects of acutely induced hypertension in cats on pial arteriolar caliber, local cerebral blood flow, and the blood-brain barrier". *Circ Res* **39** (1976), pp. 33–41.

[Mac79]   MacKenzie, E. et al. "Effects of hemorrhagic hypotension on the cerebral circulation. I. Cerebral bood flow and pial arteriolar caliber". *Stroke* **10** (1979), pp. 711–718.

[Mad14]   Mader, G. et al. "Modeling cerebral blood flow velocity during orthostatic stress". *Ann Biomed Eng* (2014).

[Mad16]   Mader, G. et al. "Using modeling to identify changes in dynamic cerebral autoregulation in aging and hypertension (under review)". *J Cereb Blood Flow Metab* (2016).

[Mae94]   Maeda, H et al. "Reactivity of cerebral blood flow to carbon dioxide in hypertensive patients: evaluation by the transcranial Doppler method". *J Hypertens* **12** (1994), pp. 191–197.

[Mah13]   Mahdi, A et al. "Modeling the afferent dynamics of the baroreflex control system". *PLoS Comput Biol* **9** (2013), e10033384.

[Mah14]   Mahdi, A et al. "Identifiability of viscoelastic mechanical systems". *PLoS ONE* **9** (2014), e86411.

[Mah16]   Mahdi, A et al. "Increased blood pressure variability upon standing up improves reproducibility of cerebral autoregulation indices". *Preprint* (2016).

[Mar12]   Martina, J. et al. "Noninvasive continuous arterial blood pressure monitoring with Nexfin". *Anesthesiology* **116** (2012), pp. 1092–1103.

[MS14]   Meshkat, N & Sullivant, S. "Identifiable reparametrizations of linear compartment models". *J Symbolic Comput* **63** (2014), pp. 46–67.

[Mia11]   Miao, H et al. "On identifiability of nonlinear ODE models and applications in viral dynamics". *SIAM Rev* **53** (2011), pp. 3–39.

[NM65]   Nelder, J. & Mead, R. "A simplex method for function minimization". *The Computer Journal* **7** (1965), pp. 308–313.

[Nis07]   Nishimura, N et al. "Penetrating arterioles are a bottleneck in the perfusion of neocortex". *Proc Natl Acad Sci U S A* **104** (2007), pp. 365–370.

[Nov04]   Novak, V et al. "Multimodal pressure-flow method to assess dynamics of cerebral autoregulation in stroke and hypertension". *Biomed Eng Online* **3** (2004), p. 39.

[OO13]   Olufsen, M. & Ottesen, J. "A practical approach to parameter estimation applied to model predicting heart rate regulation". *J Math Biol* **67** (2013), pp. 39–68.

[Olu00]   Olufsen, M. et al. "Dynamics of cerebral blood flow regulation explained using a lumped parameter model". *Am J Physiol Regul Integr Comp Physiol* **282** (2000), R611–R622.

[Olu02]   Olufsen, M. et al. "Dynamics of cerebral blood flow regulation explained using a lumped parameter model". *Am J Physiol Regul Integr Comp Physiol* **282** (2002), R611–R622.

[Olu05]   Olufsen, M. et al. "Blood pressure and blood flow variation during postural change from sitting to standing: model development and validation". *J Appl Physiol* **6**.99 (2005), pp. 1523–1537.

[Olu06]   Olufsen, M. et al. "Modeling baroreflex regulation of heart rate during orthostatic stress". *Am J Physiol Regul Integr Comp Physiol* **291**.5 (2006), R1355–R1368.

[Pan98]   Panerai, R. "Assessment of cerebral pressure-autoregulation in humans - a review of measurement methods". *Physiol Meas* **19** (1998), pp. 305–338.

[Pan09]   Panerai, R. "Transcranial Doppler for evaluation of cerebral autoregulation". *Clin Auton Res* **19** (2009), pp. 197–211.

[Pan95]   Panerai, R. et al. "Cerebral autoregulation dynamics in premature newborns". *Stroke* **26** (1995), pp. 74–80.

[Pan96]   Panerai, R. et al. "Analysis of cerebral blood flow autoregulation in neonates". *IEEE Trans Biomed Eng* **43** (1996), pp. 779–788.

[Pan99]   Panerai, R. et al. "Linear and nonlinear analysis of human dynamic cerebral autoregulation". *Am J Physiol Heart Circ* **277** (1999), H1089–H1099.

[Pan00]   Panerai, R. et al. "Multivariate dynamic analysis of cerebral blood flow regulation in humans". *IEEE Trans Biomed Eng* **47**.3 (2000), pp. 419–423.

[Pan01]   Panerai, R. et al. "Cerebral blood flow velocity response to induced and spontaneous sudden changes in arterial blood pressure". *Am J Physiol Heart Circ Physiol* **280** (2001), H2162–H2174.

[Pan03a]   Panerai, R. et al. "Variability of time-domain indices of dynamic cerebral autoregulation". *Physiol Meas* **24** (2003), pp. 367–381.

[Pan03b]   Panerai, R. et al. "Variability of time-domain indices of dynamic cerebral autoregulation." *Physiol Meas* **24** (2003), pp. 367–381.

[Pau90]   Paulson, O. et al. "Cerebral autoregulation". *Cerebrovasc Brain Metab Rev* **2** (1990), pp. 161–192.

[Pay06]   Payne, S. "A model of the interaction between autoregulation and neural activation in the brain". *Math Biosci* **204** (2006), pp. 260–281.

[Pay16]   Payne, S. *Cerebral autoregulation: control of blood flow in the brain*. Switzerland: Springer, 2016.

[Pet11]   Peterson, E. et al. "Regulation of cerebral blood flow". *Int J Vasc Med* **2011** (2011), pp. 1–8.

[Pet14]   Peterson, N. et al. "Comparison of non-invasive and invasive arterial blood pressure measurement for assessment of dynamic cerebral autoregulation". *Neurocrit Care* **20** (2014), pp. 60–68.

[Pop09]   Pope, S. et al. "Estimation and identification of parameters in a lumped cere-brovascular model". *Math Biosci Eng* **6**.1 (2009), pp. 93–115.

[Pou08]   Pournaras, C. et al. "Regulation of retinal blood flow in health and disease". *Prog Retin Eye Res* **27** (2008), pp. 284–330.

[Ran02]   Rannala, B. "IdentiŎability of Parameters in MCMC Bayesian Inference of Phy-logeny". *Syst Biol* **51** (2002), pp. 754–760.

[Rau09]   Raue, A et al. "Structural and practical identifiability analysis of partially ob-served dynamical models by exploiting the profile likelihood". *Bioinformatics* **25** (2009), pp. 1923–1929.

[Rei08]   Reinhard, M et al. "Cerebral dysautoregulation and the risk of ischemic events in occlusive carotid artery disease". *J Neurology* **255** (2008), pp. 1182–1189.

[Ros95]   Rosenblum, W. "Autoregulatory plateau: does it exist?" *J Cereb Blood Flow Metab* **15** (1995), pp. 174–177.

[Ros03]   Rosengarten, B et al. "Neurovascular coupling remains unaffected during nor-mal aging". *J Neuroimaging* **13** (2003), pp. 43–47.

[Sau89]   Saul, J. et al. "Transfer function analysis of autonomic regulation. II. Respiratory sinus arrhythmia". *Am J Physiol* **256** (1989), H153–H161.

[Sau91]   Saul, J. et al. "Transfer function analysis of the circulation: unique insights into cardiovascular regulation". *Am J Physiol* **261** (1991), H1231–H1245.

[Ser01]   Serrador, J. et al. "Effect of acute exposure to hypergravity (GX vs. GZ) on dynamic cerebral autoregulation". *J Appl Physiol* **91** (2001), pp. 1986–1994.

[Ser05]   Serrador, J. et al. "Cerebral pressure-flow relations in hypertensive elderly hu-mans: transfer gain in different frequency domains". *J Appl Physiol* **98** (2005), pp. 151–159.

[Sor05]   Sorond, F. et al. "Regional cerebral autoregulation during orthostatic stress: age-related differences". *J Gerontol A Biol Sci Med Sci* **60** (2005), pp. 1484–1487.

[Sor09]   Sorond, F. et al. "The sit-to-stand technique for the measurement of dynamic cerebral autoregulation". *Ultrasound Med Biol* **35** (2009), pp. 21–29.

[Spr12]   Spronck, B et al. "A lumped parameter model of cerebral blood flow control combining cerebral autoregulation and neurovascular coupling". *Am J Physiol Heart Circ Physiol* **303** (2012), H1143–53.

[Str73]   Strandgaard, S et al. "Autoregulation of brain circulation in severe arterial hypertension". *Br Med J* **1** (1973), pp. 507–510.

[Tho09]   Thompson, D. et al. "Parameter estimation in a simplified MWD model for HDPE produced by a Ziegler-Natta catalyst". *Macromol React Eng* **3** (2009), pp. 160–177.

[Tie95]   Tiecks, F. et al. "Comparison of static and dynamic cerebral autoregulation measurements". *Stroke* **26** (1995), pp. 1014–1019.

[Try13]   Tryambake, D et al. "Intensive blood pressure lowering increases cerebral blood flow in older subjects with hypertension". *Hypertension* **61** (2013), pp. 1309–1361.

[Urb08]   Urbano, F et al. "Impaired cerebral autoregulation in obstructive sleep apnea". *J Appl Physiol* **105** (2008), pp. 1852–1857.

[Urs88a] Ursino, M. "A mathematical study of human intracranial hydrodynamics. Part 1 - The cerebrospinal fluid pulse pressure". *Ann Biomed Eng* **16** (1988), pp. 379–401.

[Urs88b] Ursino, M. "A mathematical study of human intracranial hydrodynamics. Part 2 - Simulation of clinical tests". *Ann Biomed Eng* **16** (1988), pp. 403–416.

[UL97]   Ursino, M & Lodi, C. "A simple mathematical model of the interaction between intracranial pressure and cerebral hemodynamics". *Am J Physiol Heart Circ Physiol* (1997), pp. 1256–1269.

[UL98]   Ursino, M & Lodi, C. "Interaction among autoregulation, CO_2 reactivity, and intracranial pressure: a mathematical model". *Am J Physiol Heart Circ Physiol* **274** (1998), H1715–H1728.

[Urs95]   Ursino, M et al. "Intracranial pressure dynamics in patients with acute brain damage: a critical analysis with the aid of a mathematical model". *IEEE Trans Biomed Eng* **42** (1995), pp. 529–540.

[Urs00]   Ursino, M et al. "Cerebral hemodynamics during arterial and CO_2 pressure changes: in vivo prediction by a mathematical model". *Am J Physiol Heart Circ Physiol* **279** (2000), H2439–H2455.

[VJ08]   Valdez-Jasso, D et al. "Viscoelastic mapping of the arterial ovine system using a Kelvin model". *IEEE Trans Biomed Eng* **56** (2008), pp. 210–219.

[VJ11]   Valdez-Jasso, D et al. "Linear and nonlinear viscoelastic modeling of aorta and carotid pressure-area dynamics under *in vivo* and *ex vivo* conditions". *Ann Biomed Eng* **39** (2011), pp. 1438–1456.

[Vav02]   Vavilala, M. et al. "Dynamic cerebral autoregulation in healthy adolescents". *Acta Anaesthesiol Scand* **46** (2002), pp. 393–397.

[Vok07]   Vokatch, N et al. "Is cerebral autoregulation impaired in Parkinson?s disease? A transcranial Doppler study". *J Neurol Sci* **254** (2007), pp. 49–53.

[WC13]   Walsh, M. & Cole, W. "Review article: The role of actin filament dynamics in the myogenic response of cerebral resistance arteries". *J Cereb Blood Flow Metab* **33** (2013), pp. 1–12.

[Win85]   Winn, H. et al. "The role of adenosine in autoregulation of cerebral blood flow". *Ann Biomed Eng* **13** (1985), pp. 321–328.

[WZ06]   Wu, H & Zhang, J. *Nonparametric regression methods for longitudinal data analysis: mixed-effects modeling approaches*. Vol. 515. John Wiley & Sons, 2006.

[Yam05]   Yam, A. et al. "Cerebral autoregulation and ageing". *J Clin Neurosci* **12** (2005), pp. 643–646.

[ZM97]   Zauner, A & Muizelaar, J. *Chapter 5: Brain metabolism and cerebral blood flow*. Head Injury. London: Chapman & Hall, 1997.

[Zha98]   Zhang, R et al. "Transfer function analysis of dynamic cerebral autoregulation in humans". *Am J Physiol* **274** (1998a), H233–H241.

[Zha07]   Zhang, R et al. "Cerebral hemodynamics after short- and long-term reduction in blood pressure in mild and moderate hypertension". *Hypertension* **49** (2007), pp. 1149–1155.

[Zon03]   Zong, W et al. "An open-source algorithm to detect onset of arterial blood pressure pulses". *Computers in Cardiology* (2003), pp. 259–262.